

# MULTIPLE SCALE ANALYSIS OF DAMAGE EVOLUTION IN REAL HETEROGENEOUS MATERIALS

Final Report to

Engineering and Environmental Sciences Division

Solid Mechanics Program

Dr. M.A. Zikry and Dr. K.R. Iyer, Program Managers

Department Of The Army  
ARMY RESEARCH OFFICE  
P.O. Box 12211  
Research Triangle Park  
NC 27709-2211

for

Grant # DAAH04-95-1-076  
to The Ohio State University

by

Somnath Ghosh, Principal Investigator  
Associate Professor of Applied Mechanics  
Department of Aerospace Engineering, Applied Mechanics and Aviation  
323 Boyd Laboratory, 155 W. Woodruff Ave.  
The Ohio State University, Columbus, OH 43210

1999

## DISTRIBUTION STATEMENT A

Approved for Public Release  
Distribution Unlimited

1

DTIC QUALITY INSPECTED 4

19991101 058

## REPORT DOCUMENTATION PAGE

Form Approved  
OMB NO. 0704-0188

Public reporting burden for this collection of information is estimated to average 1 hour per response, including the time for reviewing instructions, searching existing data sources, gathering and maintaining the data needed, and completing and reviewing the collection of information. Send comment regarding this burden estimate or any other aspect of this collection of information, including suggestions for reducing this burden, to Washington Headquarters Services, Directorate for Information Operations and Reports, 1215 Jefferson Davis Highway, Suite 1204, Arlington, VA 22202-4302, and to the Office of Management and Budget, Paperwork Reduction Project (0704-0188), Washington, DC 20503.

1. AGENCY USE ONLY (Leave blank)

2. REPORT DATE

3. REPORT TYPE AND DATES COVERED

PROGRESS REPORT

FINAL

4. TITLE AND SUBTITLE

MULTIPLE SCALE ANALYSIS OF DAMAGE AND TEXTURE EVOLUTION  
IN REAL HETEROGENEOUS MATERIALS.

5. FUNDING NUMBERS

DAAH04-95-1-0176

6. AUTHOR(S)

SOMNATH GHOSH

7. PERFORMING ORGANIZATION NAME(S) AND ADDRESS(ES)

APPLIED MECHANICS SECTION  
327 BOYD LABORATORY  
155 W. WOODRUFF AVENUE  
THE OHIO STATE UNIVERSITY, COLUMBUS, OH 432108. PERFORMING ORGANIZATION  
REPORT NUMBER

1

9. SPONSORING / MONITORING AGENCY NAME(S) AND ADDRESS(ES)

U.S. Army Research Office  
P.O. Box 12211  
Research Triangle Park, NC 27709-221110. SPONSORING / MONITORING  
AGENCY REPORT NUMBER

ARO 33514.10-EG

11. SUPPLEMENTARY NOTES

The views, opinions and/or findings contained in this report are those of the author(s) and should not be construed as an official Department of the Army position, policy or decision, unless so designated by other documentation.

12a. DISTRIBUTION / AVAILABILITY STATEMENT

Approved for public release; distribution unlimited.

12 b. DISTRIBUTION CODE

13. ABSTRACT (Maximum 200 words)

A combined experimental-computational approach has been pursued to study the evolution of microscopic damage to cause failure in heterogeneous composite and porous materials. The experiments include interrupted testing methods where the load is halted prior to fracture. Microstructures in the severely necked region are examined in 3D using a serial sectioning method. Characterization functions are generated and sensitivity analysis is conducted to explore the influence of morphological parameters on damage. A novel microstructural Voronoi cell finite element model (VCFEM) is developed to simulate the evolution of damage in microstructures. The model is capable of efficient and accurate prediction of microstructure evolution and particle cracking. An adaptive multi-level methodology is developed to create a hierarchy of computational sub-domains with varying resolution for multiple scale problems. It concurrently predicts evolution of variables at the structural scales by conventional FEM and at the microstructural scales by VCFEM.

14. SUBJECT TERMS

15. NUMBER OF PAGES

16. PRICE CODE

17. SECURITY CLASSIFICATION  
OF REPORT

UNCLASSIFIED

18. SECURITY CLASSIFICATION  
OF THIS PAGE

UNCLASSIFIED

19. SECURITY CLASSIFICATION  
OF ABSTRACT

UNCLASSIFIED

20. LIMITATION OF ABSTRACT

UL

# Contents

<b>1</b>	<b>Introduction</b>	<b>1</b>
<b>2</b>	<b>List of Publications</b>	<b>4</b>
2.1	Dissertations/Theses Acknowledging this Grant . . . . .	4
2.2	Refereed Publications Acknowledging this Grant . . . . .	4
<b>3</b>	<b>Voronoi Cell FEM for Damage in Heterogeneous Microstructures</b>	<b>6</b>
3.1	Introduction . . . . .	6
3.2	Voronoi Cell FEM with Particle Fracture . . . . .	8
3.2.1	Voronoi cell element formulation for damage . . . . .	8
3.2.2	Element assumptions . . . . .	9
3.2.3	Constitutive relations and particle cracking criterion . . . . .	10
3.3	Validation Examples for Voronoi Cell FEM . . . . .	11
3.3.1	Square diagonal packing with existing crack . . . . .	12
3.4	Damage in Non-uniform Microstructures . . . . .	12
3.4.1	Computer simulated microstructures . . . . .	15
3.4.2	Particle splitting simulation with actual micrographs . . . . .	19
3.5	Conclusions . . . . .	27
<b>4</b>	<b>Multi-level Computational Model For Multiscale Damage Analysis In Composite And Porous Materials</b>	<b>32</b>
4.1	Introduction . . . . .	32
4.2	Two Way Coupling for Multiple Scale Modeling . . . . .	35
4.3	A Multi Level Model for Coupling Different Scales . . . . .	36
4.4	Homogenization with Voronoi Cell FEM . . . . .	39
4.4.1	Asymptotic homogenization with microstructural periodicity . . . . .	39
4.4.2	The Voronoi cell FEM for microstructural analysis . . . . .	41
4.4.3	Coupling asymptotic homogenization with VCFEM . . . . .	42
4.5	Computational Subdomain Level-0 in the Hierarchical Model . . . . .	43
4.5.1	An elastic-plastic constitutive model . . . . .	43
4.5.2	Elasto-plasticity with anisotropic yield function . . . . .	44
4.5.3	Numerical implementation of the constitutive model . . . . .	48
4.5.4	Numerical examples with the continuum constitutive model . . . . .	49
4.6	Computational Subdomain Level-1 in the Hierarchical Model . . . . .	53
4.7	Computational Subdomain Level-2 in the Hierarchical Model . . . . .	56

4.7.1	Damage criterion for particle cracking in level-2 . . . . .	57
4.8	Coupling the Levels in the Hierarchical FEM . . . . .	57
4.9	Adaptation Criteria for Various Levels . . . . .	60
4.10	Numerical Examples with the Adaptive Multilevel Model . . . . .	61
4.10.1	Effects of inhomogeneity size (Scale effect) . . . . .	62
4.10.2	Homogenization vs. multi-level simulation . . . . .	66
4.10.3	Effect of heterogeneity distribution and shape . . . . .	68
4.10.4	A heterogeneous plate with a macroscopic holes . . . . .	72
4.11	Conclusions . . . . .	72
<b>5</b>	<b>Experimental-Computational Investigation Of Damage Evolution In Discontin-</b>	
	<b>uously Reinforced Aluminum Matrix Composite</b>	<b>82</b>
5.1	Introduction . . . . .	82
5.2	Experiments for Damage Assessment . . . . .	83
5.2.1	Interrupted tests . . . . .	83
5.2.2	Damage examination and microscopic analysis . . . . .	84
5.2.3	Major observations . . . . .	86
5.3	Equivalent Microstructure & Mesh Generation . . . . .	86
5.4	Microstructure and Damage Characterization . . . . .	89
5.5	Damage Simulation by Voronoi Cell FEM . . . . .	92
5.5.1	Calibration of Weibull parameters $\sigma_0$ and $m$ . . . . .	94
5.6	Characteristic Size of Microstructures . . . . .	100
5.7	Conclusions . . . . .	102
<b>6</b>	<b>List of Participating Scientific Personnel</b>	<b>106</b>



# Chapter 1

## Introduction

The project entitled "*Multiple Scale Analysis of Damage and Texture Evolution in Real Heterogeneous Materials*" began in January 1995. A no-cost extension was granted to continue this project till December 31, 1998. During the four year period of this grant, substantial progress has been made in advancing the state of the art in multiple scale modeling of damage in heterogeneous materials. Research has been conducted in a few distinct areas that are delineated below. A list of publications, acknowledging this grant is provided in chapter 2.

### **I. Voronoi Cell Finite Element Model for Damage in Heterogeneous Microstructures**

(Details in: Chapter 3)

This work deals with the evolution of damage in microstructures of reinforced ductile-matrix composites, by particle cracking and splitting. A small deformation Voronoi Cell finite element model is developed, in which each element may consist of a matrix phase, an inclusion phase and a crack phase. Brittle inclusions may be of arbitrary shapes and sizes, and may be dispersed non-uniformly in the matrix. Damage initiation of inclusions is assumed to follow a maximum principal stress theory. Complete particle cracking or splitting is assumed at the onset of damage. The model is validated by a few comparison studies. Various geometric patterns are studied to test the effectiveness of the model, as well as to understand the effect of morphology on damage evolution. Actual microstructures from optical micrographs of Al-Si-Mg composite systems are analyzed and compared with experimentally observed results. Quantitative characterization and statistical analysis is conducted to correlate morphological parameters with mechanical response.

### **II. Multi-level Computational Model For Multiscale Damage Analysis In Composite And Porous Materials**

(Details in: Chapter 4)

An adaptive multi-level methodology is developed in this work to create a hierarchy of computational sub-domains with varying resolution for multiple scale problems. It is intended to concurrently predict evolution of variables at the structural and microstructural scales, as well as to track the incidence and propagation of microstructural damage in composite and porous

materials. The microstructural analysis is conducted with the Voronoi cell finite element model (VCFEM), while a conventional displacement based FEM code executes the macroscopic analysis. The model introduces three levels in the computational domain which include macro, macro-micro and microscopic analysis. It differentiates between non-critical and critical regions and ranges from macroscopic computations using continuum constitutive relations to zooming in at 'hotspots' for pure microscopic simulations. Coupling between the scales in regions of periodic microstructure is accomplished through asymptotic homogenization. An adaptive process significantly increases the efficiency while retaining appropriate level of accuracy for each region. Numerical examples are conducted for composite and porous materials with a variety of microscopic architectures to demonstrate the potential of the model.

### **III. Experimental-Computational Investigation Of Damage Evolution In Discontinuously Reinforced Aluminum Matrix Composite**

(Details in: Chapter 5)

This work deals with a combined experimental-computational approach to study the evolution of microscopic damage to cause failure in commercial SiC particle reinforced DRA's. Determination of aspects of microstructural geometry that are most critical for damage nucleation and evolution forms a motivation for this work. An interrupted testing technique is invoked where the load is halted in the material instability zone, following necking but prior to fracture. Sample microstructures in the severely necked region are microscopically examined in 3D using a serial sectioning method. The micrographs are then stacked sequentially on a computer to reconstruct 3D microstructures. Computer simulated equivalent microstructures with elliptical or ellipsoidal particles and cracks are constructed for enhanced efficiency, which are followed by tessellation into meshes of 2-D and 3-D Voronoi cells. Various characterization functions of geometric parameters are generated and sensitivity analysis is conducted to explore the influence of morphological parameters on damage. Micromechanical modeling of 2D micrographs are conducted with Voronoi Cell Finite Element Method (VCFEM). Inferences on the initiation and propagation of damage are made from the 2D simulations. Finally, the effect of size and characteristic lengths of representative material element (RME) on the extent of damage in the model systems is investigated.

### **IV. Development of the Voronoi Cell Finite Element Model for Large Deformation Crystal Plasticity**

A large deformation Voronoi cell finite element formulation is developed for modeling large elastic-plastic deformation in polycrystalline materials. The formulation is based on an assumed stress hybrid finite element method which makes independent assumption on stress rate, spin within the domain of elements, and displacement or velocity assumptions only on the element boundary. The finite element equations are solved with a two level Quasi-Newton iterative solver. The outer loop in this iterative algorithm is for displacements, and the inner loop is for stress rates and spin, with given boundary displacements. Orders of interpolating polynomials for stress rate and spin functions can be varied within each element, independent of the neighbouring element. Assuming that slip is the sole cause of plastic deformation an elastic-plastic constitutive model for crystalline

plasticity is implemented into the finite element algorithm. A two-dimensional crystal model with three slip systems is used as an example model of the single crystal that is analysed. The entire crystal is modeled with one single element in this model. Both explicit and implicit integration procedures of the evolution equations are implemented. Results for elasticity are validated by comparison with theoretical solutions and results of displacement based finite element codes. For crystal plasticity, problems encountered modeling highly rate dependent materials are noted and suggestions to future research to improve them are made. A M.S. thesis has resulted from this work.

## Chapter 2

# List of Publications

### 2.1 Dissertations/Theses Acknowledging this Grant

1. K. Lee, "Adaptive Hierarchical Modeling of Response and Damage in Heterogeneous Materials", Ph.D. Dissertation, The Ohio State University, Autumn 1998.
2. M. Li, "Characterization and Modeling of Damage in Metal Matrix Composite Microstructures", Ph.D. Dissertation, The Ohio State University, Autumn 1998.
3. S. Moorthy, "The Voronoi Cell Finite Element Method for Response and Damage Analysis of Arbitrary Heterogeneous Media", Ph.D. Dissertation, The Ohio State University, Winter 1997.
4. M. Narasa, "Large Deformation Voronoi Cell Finite Element Analysis with Crystalline Plasticity", M.S. Thesis, The Ohio State University, Winter 1997.

### 2.2 Refereed Publications Acknowledging this Grant

#### I. Voronoi Cell FEM for Damage in Heterogeneous Microstructures

1. M. Li, S. Ghosh and O. Richmond, "An experimental-computational approach to the investigation of damage evolution in discontinuously reinforced aluminum matrix composite", *Acta Materialia*, (in press).
2. S. Moorthy and S. Ghosh, "A Voronoi Cell Finite Element Model for Particle Cracking in Composite Materials," *Computer Methods in Applied Mechanics and Engineering*, Vol. 151, pp 377-400, 1998.
3. S. Moorthy and S. Ghosh, "Particle Cracking In random MMC's by VCFEM," *Intl. Jour. Plasticity*, Vol. 14, No. 8, p 805-827, 1998.
4. S. Ghosh and S. Moorthy, "Particle Fracture Simulation in Nonuniform Microstructures of Metal-Matrix Composites," *Acta Materialia*, Vol. 46, No. 3, pp 965-982, 1998.

5. S. Moorthy and S. Ghosh, "Damage Modeling in Heterogeneous Materials by the Voronoi Cell Finite Element Method," *Proceedings of 14th US Army Symposium on Solid Mechanics*, K.R. Iyer and S-C. Chou eds., Battelle Press, pp 3651-370, 1997.

## II. Multiple Scale Modeling of Heterogeneous Materials Using Asymptotic Homogenization and the Voronoi Cell FEM

6. K. Lee and S. Ghosh, "A multilevel computational model for multiscale damage analysis in composite and porous materials", *International Journal of Solids and Structures*, (in review).
7. K. Lee, S. Moorthy and S. Ghosh, "Multiple scale computational model for damage in composite materials," *Computer Methods in Applied Mechanics and Engineering*, Vol. 172 No. 1-4, pp. 175-201, 1999.
8. S. Ghosh, M. Li, S. Moorthy and K-H. Lee, "Microstructural characterization, meso-scale modeling and multiple scale analysis of discretely reinforced materials," *Materials Science and Engineering A*, Vol. 249, No. 1-2, pp 62-70, 1998.
9. S. Ghosh, "Multiple Scale Computational Model for Composite Materials with Microstructural Damage," *Multiple Scale Analyses and Coupled Physical Systems*, J. Salencon ed., Presses de lecole nationale des, pp 263-274, 1997.

## III. Methods for Material Characterization & Analysis

10. M. Li, S. Ghosh, O. Richmond, H. Weiland and T.N. Rouns, "Three dimensional characterization and modeling of particle reinforced MMCs, Part I: Quantitative description of microstructural morphology", *Materials Science and Engineering A*, Vol. A265, pp 153-173, 1999.
11. M. Li, S. Ghosh, O. Richmond, H. Weiland and T.N. Rouns, "Three dimensional characterization and modeling of particle reinforced MMCs, Part II: Damage characterization", *Materials Science and Engineering A*, (in press).
12. S. Ghosh, Z. Nowak and K. Lee, "Tessellation Based Computational Methods in Characterization and Analysis of Heterogeneous Microstructures," *Composites Science and Technology*, Vol. 57, pp 1187-1210, 1997.
13. S. Ghosh, Z. Nowak and K. Lee, "Quantitative Characterization and Modeling Of Composite Microstructures by Voronoi Cells," *Acta Materialia*, Vol. 45, No. 6, pp 2215-2234, 1997.

## Chapter 3

# Voronoi Cell FEM for Damage in Heterogeneous Microstructures

### 3.1 Introduction

The presence of fibers or particulates in composite microstructures often have adverse effects on their failure properties like fracture toughness, ductility and creep resistance. Important micromechanical phenomena that are responsible for deterring the overall properties include, fracture and splitting of reinforcements, matrix failure and inclusion-matrix debonding. Many engineering materials exhibit strong non-uniformities in inter-particle/fiber spacings, inclusion shapes, volume fractions and arrangements, at the microstructural level. In addition, there are heterogeneities at larger length scales which include local regions of clustering and directionality, often related to the fabrication process. Failure characteristics of heterogeneous materials are affected by microstructural mechanisms that control initiation and evolution of localized damage and cracks. These mechanisms are highly sensitive to local parameters, such as reinforcement distribution, morphology, size, interfacial strength etc. Experimental studies with MMCs [1] have established that particles in regions of clustering or preferential alignment, have a greater propensity towards fracture, than those in regions of dilute concentration. SEM micrographs of damaged MMCs show that larger particles tend to fracture at lower macroscopic load levels due to the existence of large flaws. Christman et.al. [8] have shown that local plastic flow is very sensitive to shape of reinforcements. Lack of reliability of these composite materials have inhibited their applications to high performance load carrying engineering components. It is therefore important to understand damage mechanisms and fracture process for enhancing the level of utilization of these material systems.

Within the framework of damage mechanics, micromechanical damage models have been employed to predict overall constitutive response by using continuum mechanics principles at the microscopic level [3, 4]. While some of these models [3] provide reasonable predictions of overall properties for a dilute distribution of damage entities, others [4] attempt to analyze the interaction effects between damage entities introduced by morphological characteristics of the microstructure. Recently, novel approaches to integrate micromechanical and computational approaches at the microscale with phenomenological approaches in the macroscale have also been proposed [5]. While many of these methods can model damage in brittle homogeneous materials, far fewer analytical

models are available for ductile two phase materials. Small scale yielding solutions using asymptotic analysis for a single bi-material interface due to Shih & Asaro [6] and Hutchinson et.al. [7] are notable exceptions.

Evolving damage in heterogeneous media with a mixture of ductile and brittle constituents have been numerically modeled using *Unit Cell* methods. These methods assume that the material is constituted of periodic repetition of unit cells, identified as representative volume elements (RVE) of the microstructure. Displacement based finite element analysis is used to analyze the RVE in order to predict the onset and growth of evolving damage. Notable among these are the finite element simulations by Needleman [11, 9], Tvergaard [12], Bao [13], Hom [14], Sugimura et.al. [13] and Finot et.al. [15]. In [12, 13, 14, 13], simple microstructures with pre-existing damaged heterogeneities are considered. In [15] a finite element mesh which allows for crack growth by element separation is used to simulate microscale particle and matrix cracking. While these models provide valuable insights into the microstructural damage processes, the simple morphologies idealize actual microstructures for many engineering materials. Consideration of simple RVE's bear little relationship to the actual stereographic features, and have limited them to the assumption that all particles or particle/matrix interfaces are *damaged simultaneously*. To circumvent these deficiencies, Suresh and coworkers [16, 8], McHugh et. al. [17] among others, have made novel progresses in computational modeling of discontinuously reinforced materials with random spatial dispersion. However, a very high resolution of finite element mesh is required even for undamaged heterogeneous media, and enormous computational efforts are required to capture failure by these models.

The microstructure based *Voronoi Cell Finite Element Model (VCFEM)* developed by Ghosh et.al. [34, 35], has shown a significant promise in this regard. It can overcome the large computational requirements of conventional finite element methods, by combining concepts of hybrid finite elements with characteristics of micromechanics. The VCFEM mesh naturally evolves from the microstructure by Dirichlet tessellation to generate a network of multi-sided *Voronoi polygons*. Each Voronoi cell represents a basic structural element containing one second phase inclusion at most (see [19] for details), and the analysis needs no further discretization leading to drastically reduced efforts in generating the microstructural mesh. Additionally, computational efficiency is greatly enhanced due to Voronoi cell elements being considerably larger than conventional unit cell finite elements, with reduced degrees of freedom.

The evolution of damage by particle cracking or splitting, in particle reinforced ductile matrix microstructures, is analyzed in this work by a Voronoi cell finite element model. No matrix cracking is allowed in this work. Each Voronoi cell element may consist of a matrix phase, an inclusion phase and a crack phase. The inclusions are brittle, of arbitrary shapes and sizes, and may be dispersed non-uniformly in the matrix. Damage initiation is assumed to follow a maximum principal stress theory or Rankine criterion. Complete particle cracking or splitting is assumed at the onset of damage. Different geometric patterns are studied to test the effectiveness of the model, as well as to understand the effect of morphology on damage evolution. Actual microstructures from optical micrographs of Al-Si-Mg composite systems are analyzed and compared with experimentally observed results. Quantitative characterization and statistical analysis is conducted to correlate morphological parameters with mechanical response.



## 3.2 Voronoi Cell FEM with Particle Fracture

The Voronoi cell finite element model has been developed for undamaged composite and porous materials in [34, 35] using the assumed stress hybrid formulation. The formulation is extended to accommodate damage evolution in the form of particle cracking or splitting. It is assumed that in particle cracking, the crack is completely contained within the inclusion, while for particle splitting its tip extends nominally into the matrix. The crack in a fractured particle is realized as an elliptical void with a high aspect ratio ( $\sim 10-100$ ), implying a blunt crack. Each Voronoi cell element is amenable to change in topology from two constituent phases (matrix and inclusions) in undamaged cells, to three phases (matrix, inclusion and crack) in damaged cells. Complete particle cracking or splitting is assumed to occur at the very onset of damage, and thus the problem of crack propagation within each inclusion is avoided. This assumption is justifiable from the consideration that for the multitude of inclusions analyzed, crack propagation in each inclusion would make the problem inordinately large. Additionally, experimental observations indicate rapid transition from crack initiation to complete cracking/splitting.

### 3.2.1 Voronoi cell element formulation for damage

Consider a typical representative material element (RME) consisting of  $N$  undamaged and/or damaged particles, that are contained in each of the  $N$  Voronoi cell elements as shown in figure 3.5(a). The assumed stress hybrid formulation in the Voronoi cell finite element method (VCFEM) requires independent assumptions of an equilibrated stress field ( $\sigma$ ) in the interior of each element  $\Omega_e$ , and compatible displacement fields  $\mathbf{u}$  on the element boundary  $\partial\Omega_e$ ,  $\mathbf{u}'$  on the matrix-inclusion interface  $\partial\Omega_c$  and  $\mathbf{u}''$  on the crack boundary  $\partial\Omega_{cr}$ . In an incremental formulation for elastoplasticity, the incremental two field ( $\sigma - \mathbf{u}$ ) hybrid variational formulation introduces an element energy functional,

$$\begin{aligned} \Pi_e^C(\Delta\sigma, \Delta\mathbf{u}) = & - \int_{\Omega_e} \Delta B(\sigma, \Delta\sigma) d\Omega - \int_{\Omega_e} \epsilon : \Delta\sigma d\Omega + \\ & \int_{\partial\Omega_e} (\sigma + \Delta\sigma) \cdot \mathbf{n}^e \cdot (\mathbf{u} + \Delta\mathbf{u}) \partial\Omega - \int_{\Gamma_{tm}} (\bar{\mathbf{t}} + \Delta\bar{\mathbf{t}}) \cdot (\mathbf{u} + \Delta\mathbf{u}) d\Gamma \\ & - \int_{\partial\Omega_c} (\sigma^m + \Delta\sigma^m - \sigma^c - \Delta\sigma^c) \cdot \mathbf{n}^c \cdot (\mathbf{u}' + \Delta\mathbf{u}') \partial\Omega \\ & - \int_{\partial\Omega_{cr}} (\sigma^c + \Delta\sigma^c) \cdot \mathbf{n}^{cr} \cdot (\mathbf{u}'' + \Delta\mathbf{u}'') \partial\Omega \end{aligned} \quad (3.1)$$

where  $\Delta B$  is the increment of complimentary energy density. Variables  $(\sigma, \mathbf{u})$  correspond to values at the beginning of an increment, while variables  $(\Delta\sigma, \Delta\mathbf{u})$  are the corresponding increments in a load increment or step. Outward normals on  $\partial\Omega_e$ ,  $\partial\Omega_c$  and  $\partial\Omega_{cr}$  are denoted by  $\mathbf{n}^e$ ,  $\mathbf{n}^c$  and  $\mathbf{n}^{cr}$  respectively. Superscripts  $m$ ,  $c$  and  $cr$  are associated with the matrix, inclusion and crack phases respectively in each Voronoi cell element. The total energy for the entire RME of  $N$  Voronoi cells is obtained as  $\Pi^C = \sum_{e=1}^N \Pi_e^C$ . Setting the first variation of  $\Pi_e^C$  in equation (3.1) with respect to stress increments  $\Delta\sigma$  to zero yields the element compatibility as the Euler equation, while setting the first variations of  $\Pi^C$  with respect to the independent boundary displacements  $\Delta\mathbf{u}$ ,  $\Delta\mathbf{u}'$  and  $\Delta\mathbf{u}''$  to zero, yield the inter-element traction reciprocity or element boundar traction, interface traction reciprocity and zero traction on crack boundary respectively. Equilibrated stress increments  $\Delta\sigma$ ,



compatible displacement fields  $\Delta \mathbf{u}$ ,  $\Delta \mathbf{u}'$  and  $\Delta \mathbf{u}''$ , the stress-strain relationships ( $\frac{\partial \Delta B}{\partial \Delta \boldsymbol{\sigma}} = \Delta \boldsymbol{\epsilon}$ ), along with the Euler equations completely define the incremental problem for a heterogeneous RME.

### 3.2.2 Element assumptions

Independent assumptions on stress increments  $\Delta \boldsymbol{\sigma}$  are made in the matrix and inclusion phases in each element, thus allowing stress discontinuities across the interface. In two-dimensional analysis, the Airy's stress function  $\Phi(x, y)$  is usually convenient in deriving equilibrated stress fields. Components of  $\Delta \boldsymbol{\sigma}$  are expressed in terms of  $\Phi$  as:

$$\Delta \sigma_{xx} = \frac{\partial^2 \Phi}{\partial y^2}, \quad \Delta \sigma_{yy} = \frac{\partial^2 \Phi}{\partial x^2}, \quad \Delta \sigma_{xy} = -\frac{\partial^2 \Phi}{\partial x \partial y} \quad (3.2)$$

Incorporation of key features of micromechanics in the choice of stress functions significantly enhances computational efficiency. Moorthy and Ghosh [34, 19] have introduced a decomposition of the matrix and inclusion stress functions into (a) purely polynomial functions  $\Phi_{poly}^m$ ,  $\Phi_{poly}^c$  and (b) reciprocal functions  $\Phi_{rec}^m$ ,  $\Phi_{rec}^{mc}$  and  $\Phi_{rec}^{cc}$ , for elements with matrix, inclusion and crack phases. Mathematically, the stress functions for the matrix and inclusion phases are constructed as:

$$\begin{aligned} \Phi^m &= \Phi_{poly}^m + \Phi_{rec}^m + \Phi_{rec}^{mc} \\ \Phi^c &= \Phi_{poly}^c + \Phi_{rec}^{cc} \end{aligned} \quad (3.3)$$

In the above equation, the purely polynomial part of the stress functions  $\Phi_{poly}^{m/c}$  account for the far field tractions on the element boundary  $\partial \Omega_e$  and on the interface  $\partial \Omega_c$ , and are expressed as:

$$\Phi_{poly}^{m/c} = \sum_{p,q} \xi^p \eta^q \Delta \beta_{pq}^{m/c} \quad (3.4)$$

where  $(\xi, \eta)$  are the scaled local coordinates with origin at the element centroid  $(x_c, y_c)$ , and may be written as  $\xi = (x - x_c)/L$ ,  $\eta = (y - y_c)/L$ .  $L$  is a scaling parameter  $(= \sqrt{\max(x - x_c) \max(y - y_c)}) \forall (x, y) \in \partial \Omega$ . The use of the local coordinates  $(\xi, \eta)$  prevents numerical inaccuracies in  $\Phi^{m/c}$  due to high exponents of  $(x, y)$ , and thus avoid ill-conditioning of the element stiffness matrices. The reciprocal terms  $\Phi_{rec}^m$ ,  $\Phi_{rec}^{mc}$  and  $\Phi_{rec}^{cc}$  facilitate stress concentration near the interface and crack boundary, accounting for the shape of the inclusion and crack. They also help satisfy traction reciprocity (zero traction for the crack) at the interfaces  $\partial \Omega_c$  and  $\partial \Omega_{cr}$ , as well as decay at large distances from these interfaces. The matrix reciprocal function  $\Phi_{rec}^m$  is constructed from a transformed radial coordinate  $f$ , that is generated by either a Schwarz-Christoffel conformal transformation (for elliptical heterogeneities) [20], or by a Fourier series transformation of the interface  $\partial \Omega_c$  (for arbitrary shapes) [34]. The radial distance  $f$  satisfies the conditions  $f \rightarrow \infty$  as  $(x, y) \rightarrow \infty$ , and  $f = 1$  on the interface  $\partial \Omega_c$ . In the expression for  $\Phi_{rec}^m$ , shape effects are dominant near  $\partial \Omega_c$  and vanish in the far-field.

$$\Phi_{rec}^m = \sum_{p,q} \xi^p \eta^q \sum_i \frac{1}{f^{p+q+i-1}} \Delta \beta_{pqi}^m \quad (3.5)$$

At the interface ( $f = 1$ ), coefficients  $\Delta \beta_{pqi}^m$  in equation (3.5) impart flexibility to the polynomial coefficients  $\Delta \beta_{pq}^m$  for matching traction conditions. Finally, the terms  $\Phi_{rec}^{mc}$  and  $\Phi_{rec}^{cc}$  are contributions

to the matrix and inclusion stress functions due to the crack.

$$\begin{aligned}\Phi_{rec}^{mc} &= \sum_{p,q} \xi^p \eta^q \sum_i \left( \frac{\Delta \beta_{pqi}^{mc}}{f_{cr}^{p+q+i-1}} \right) \\ \Phi_{rec}^{cc} &= \sum_{p,q} \xi^p \eta^q \sum_i \left( \frac{\Delta \beta_{pqi}^{cc}}{f_{cr}^{p+q+i-1}} \right)\end{aligned}\quad (3.6)$$

The inclusion crack is assumed to be of elliptical shape with a high aspect ratio. Consequently, the crack boundary  $\partial\Omega_{cr}$  is parametrically represented through a conformal mapping of the ellipse as  $f_{cr}(x, y) = 1$ .  $f_{cr}$  represents a parameterized radial coordinate with the property  $f_{cr} \rightarrow \infty$  as  $(x, y) \rightarrow \infty$ . The reciprocal terms  $\frac{1}{f_{cr}^{p+q+i-1}}$  in  $\Phi_{rec}^{cc}$  facilitate zero traction condition on the crack boundary  $\partial\Omega_{cr}$ . The same terms in  $\Phi_{rec}^{mc}$  provide asymptotic stress gradients near the crack tip in the matrix. Stress increments may be derived by substituting  $\Phi$  functions in the equation (3.2) in the form  $\{\Delta\sigma^m\} = [P^m]\{\Delta\beta^m\}$  for the matrix and  $\{\Delta\sigma^c\} = [P^c]\{\Delta\beta^c\}$  for the inclusion. All of the stress coefficients  $\{\Delta\beta^m\}$  and  $\{\Delta\beta^c\}$  are a-priori unknown and are solved by setting the first variation of the element energy functional (3.1) with respect to the stresses to zero. Compatible displacement increments are generated on each of the boundaries/interfaces  $\partial\Omega_e$ ,  $\partial\Omega_c$  and  $\partial\Omega_{cr}$  by interpolation in terms of generalized nodal displacements as ,

$$\{\Delta u\} = [L^e]\{\Delta q\} \quad , \quad \{\Delta u'\} = [L^c]\{\Delta q'\} \quad , \quad \{\Delta u''\} = [L^{cr}]\{\Delta q''\} \quad (3.7)$$

where  $\{\Delta q\}$ ,  $\{\Delta q'\}$  and  $\{\Delta q''\}$  are the nodal displacement increment vectors, and  $[L^e]$ ,  $[L^c]$  and  $[L^{cr}]$  are the corresponding interpolation matrices. In general, linear forms of  $[L]$  are computationally efficient. However for the crack boundary, discontinuous normals at the nodes may degrade the solution and hence a quadratic interpolation is implemented. Details of the solution process are provided in [34, 19, 21].

### 3.2.3 Constitutive relations and particle cracking criterion

The reinforcing phase of particles are assumed to be brittle and are modeled as linear elastic materials. The matrix material on the hand is assumed to be ductile, and is modeled by small deformation elasto-plasticity relations using associated  $J_2$  flow theory with isotropic hardening. For the brittle particulate materials, microstructural damage initiation is assumed to be governed by a maximum principal stress based criterion, also known as the Rankine criterion. In this criterion, a crack is initiated when the maximum principal stress in tension exceeds a critical fracture stress  $\sigma_{cr}$  at a point. In the computational procedure, complete particle cracking or splitting is assumed to occur in the form of an elliptical void, as soon as the principal tensile stress reaches  $\sigma_{cr}$ . In the case of particle cracking, the crack tip coincides with the interface and is completely contained in the particle, while it extends nominally into the matrix for particle splitting. A parameter  $d_{crack} = \frac{\text{Crack Length}}{\text{Inclusion Dimension}}$  distinguishes between complete cracking and splitting of inclusions. A fully cracked inclusion corresponds to a value  $d_{crack} = 1$ , for which the crack terminates at the inclusion-matrix interface, whereas splitting is represented by  $d_{crack} = 1.004$  for which the crack tip has moved slightly into the matrix. In the incremental computational procedure, more than one point may exceed the critical  $\sigma_{cr}$  value during increment. The location of a single crack is

determined by a weighted averaging method as:

$$x_{damage} = \frac{\sum x \frac{\sigma_I^c(x,y)}{\sigma_{cr}}}{\sum \frac{\sigma_I^c(x,y)}{\sigma_{cr}}} , \quad y_{damage} = \frac{\sum y \frac{\sigma_I^c(x,y)}{\sigma_{cr}}}{\sum \frac{\sigma_I^c(x,y)}{\sigma_{cr}}} \quad \forall \quad [\sigma_I^c(x,y) \geq \sigma_{cr}] \quad (3.8)$$

where  $\sigma_I^c(x,y)$  corresponds to all values of maximum tensile principal stress larger than  $\sigma_{cr}$  in the particle. The crack is oriented at right angles to the principal stress directions at  $(x_{damage}, y_{damage})$  and extends to the interface on both sides.

### Critical Fracture Stress

Various experimental studies on metal matrix composites [6, 22, 24], suggest that the critical stress  $\sigma_{cr}$  for particle fracturing is not only material dependent, but is also influenced by the particle size due to the existence of microcracks. Micrographs of damaged composites indicate that larger particles tend to fracture at lower load levels than smaller particles. To account for the size effect in particle cracking, and hence flaw size and distribution, two alternative approaches are considered. These criteria have been discussed in Curtin [25], Kiser et.al. [24]. The first is a fracture mechanics based criterion, in which particles are assumed to contain flaws and the critical stress to fracture is determined from mode-I fast fracture of these flaws. In this criterion, an initial particle flaw size  $c$  is assumed to be a fraction of a characteristic length  $D$ , and is expressed as.  $c = eD$ . The characteristic length is considered to be the diameter of an equivalent circle or  $D = \sqrt{\frac{4A}{\pi}}$ , where  $A$  is the particle area. The factor  $e$  is determined from experimental observations, and a value  $\sim 5 - 15\%$  is found to be suitable in this study. For mode-I fracture, the critical load to fracture  $\sigma_{cr}$  is thus related to the fracture toughness  $K_{IC}$  through the relation:

$$\sigma_{cr} = \frac{K_{IC}}{\sqrt{\pi c}} = \frac{K_{IC}}{\sqrt{\pi e D}} \quad (3.9)$$

Larger particles with large initial flaws will fracture at smaller critical stresses by this relation. The second criterion uses statistical functions to correlate particle size, stress levels and failure. It is based on a Weibull distribution, in which the probability of particle fracture  $P_f(A, \sigma)$  is related to the particle volume (area in 2-D)  $A$  and the maximum principal stress  $\sigma_I$  as:

$$P_f(A, \sigma) = 1 - e^{-A(\frac{\sigma}{\sigma_{cr}})^m} \quad (3.10)$$

where  $\sigma_{cr}$  and  $m$  are two material parameters in the Weibull distribution. The probability of damage in this model, increases with larger particles at larger stress levels. The Weibull parameters  $\sigma_{cr}$  and  $m$  may be calculated by correlating geometric features and simulated stresses with experimental observations, as discussed in the section on numerical examples.

### 3.3 Validation Examples for Voronoi Cell FEM

The accuracy and efficiency of the Voronoi cell finite element model in stress analysis of heterogeneous materials with particle cracking has been extensively verified by comparison with results of analyses conducted with conventional finite element packages as well as with published results in the literature. Several comparison studies have been made with this model, some of which are

described in [21, 19]. Only one such example studies with simple, uniform distribution is described here. To establish an aspect ratio for the elliptical cracks, a numerical experiment was conducted with various aspect ratios viz. ( $\frac{a}{b} = 3, 5, 10, 25, 20 \text{ and } 100$ ). From this study, a ratio  $\frac{a}{b} = 10$  was found to be most desirable from an efficiency and accuracy point of view. While both plane stress and plane strain problems have been solved, the numerical examples presented in this work are only for the plane strain assumption.

### 3.3.1 Square diagonal packing with existing crack

This comparison problem, studied by Finot et.al. [15] with finite deformation kinematics, involves stress analysis of a square-diagonally packed composite microstructure with pre-cracked inclusions. The representative material element (RME) consists of two square SiC inclusions (volume fraction  $V_f = 20\%$ ) in an Al-3.5%Cu matrix as shown in figure (3.3.1). The elastic properties of SiC particles are assumed to be: Young's Modulus  $E = 450$  GPa and Poisson's Ratio  $\nu = 0.2$ . The elastic-plastic properties for the Al-3.5% Cu alloy matrix are taken as: Young's Modulus  $E = 72$  GPa, Poisson's Ratio  $\nu = 0.32$ ; Post yield behavior (*Power law hardening*)  $\sigma_m = \sigma_0(\epsilon_m^p/\epsilon_0 + 1)^N$ , with  $\sigma_0 = 175$  MPa, and  $N = 0.2$ . Different degrees of pre-existing damage, e.g. 0% damage with two intact inclusions, 50% damage with cracked inclusion, and 100% damage with both inclusions cracked, are assumed in accordance with those used in [15]. For 0% damage, the matrix stress function  $\Phi^m$  in equation (3.3) consists of 61 terms, with 25 polynomial terms  $\Phi_{poly}^m$  ( $p + q = 2..6$  in equation 3.4) and 36 reciprocal terms  $\Phi_{rec}^m$  ( $i = 1..3, p + q = 2..6$  in equation 3.5). The corresponding inclusion stress function  $\Phi^c$  in equation (3.3) consists of 25 polynomial terms  $\Phi_{poly}^m$  ( $p + q = 2..6$  in equation 3.5). The function  $f$  in equation (3.5) for  $\Phi_{rec}^m$  is created by a Fourier series transformation of the square interface, as described in [34]. For damaged microstructures, 36 additional terms in the form of  $\Phi_{rec}^{mc}$  and  $\Phi_{rec}^{cc}$  are appended to the stress functions  $\Phi^m$  and  $\Phi^c$  ( $i = 1..3, p + q = 2..4$  in equation 3.6).

The VCFEM simulation of the RME is executed for upto a vertical applied strain of 2% as shown in figure (3.3.1). In figure (3.3.1) the macroscopic stress-strain responses, calculated by taking volumetric averages of microscopic variables, are compared with results in [15], and excellent agreement is recorded. The stress capacity of the RME reduces considerably with transition from particle cracking to particle splitting. As the crack propagates into the matrix due to splitting, the damaged inclusions cease to carry significant load. The major load now shifts to the matrix material and the remaining undamaged inclusions. Contour plots of the effective plastic strains for the cracked and split microstructures at  $\bar{\epsilon}_{yy} = 2\%$  are presented in figures (3.3.1). The matrix regions vertically adjacent to the split inclusions have considerably less plastic strains than those adjacent to cracked inclusions, due to much lower stresses caused by splitting. Also in the case of splitting, a considerably larger plastic strain accumulates near the crack tip. The plastic strain flows in the form of ligaments from one crack tip to the next, causing bands of strain localization. Similar observations have also been made in [15] for axisymmetric inclusions.

## 3.4 Damage in Non-uniform Microstructures

Examples in the previous section consider pre-existing damage, and thus do not involve crack initiation and change of element topology. The present section deals with continuously evolving

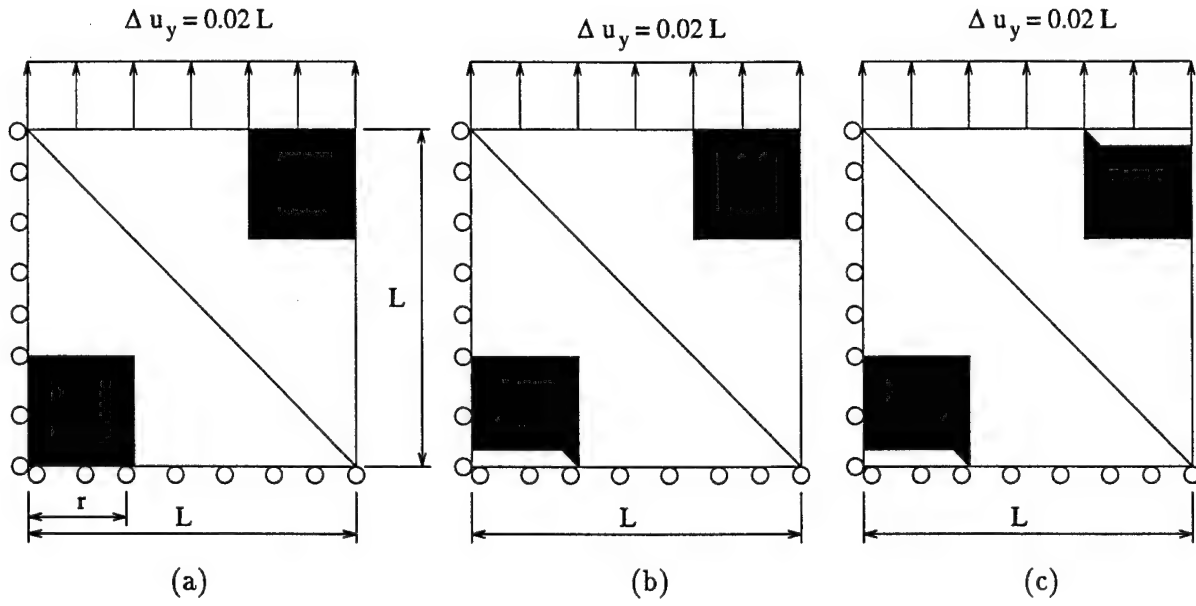


Figure 3.1: Representation and VCFEM mesh for RME with  $V_f = 20\%$  cracked square inclusions (a) 0% damage (b) 50% damage (c) 100% damage.

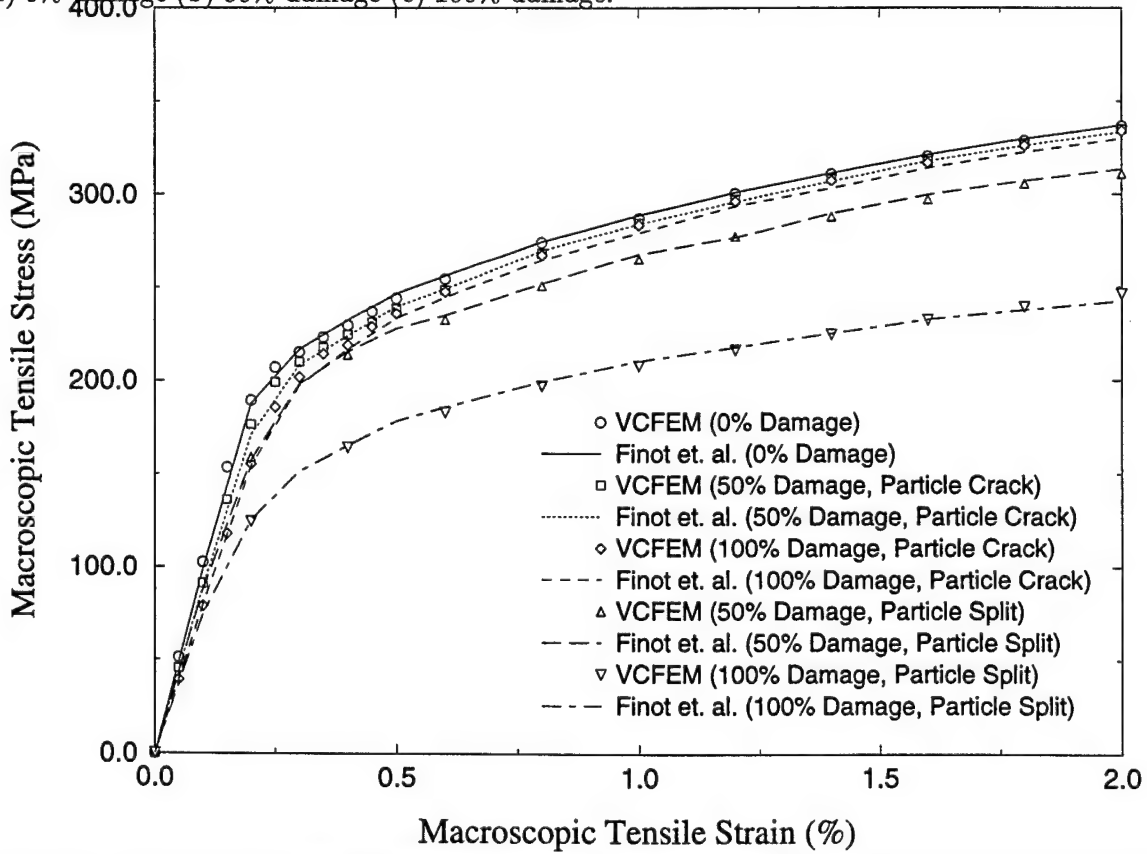
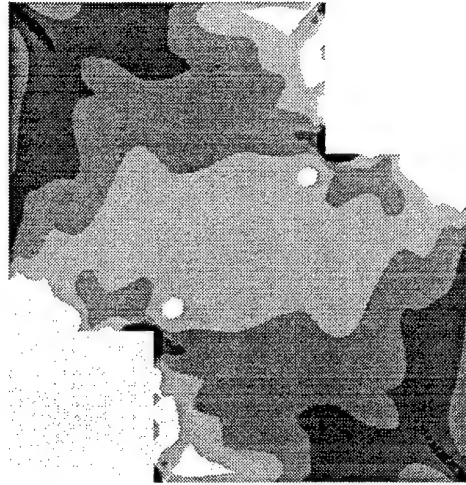


Figure 3.2: Macroscopic stress-strain response for RMEs with  $V_f = 20\%$  cracked square inclusions.



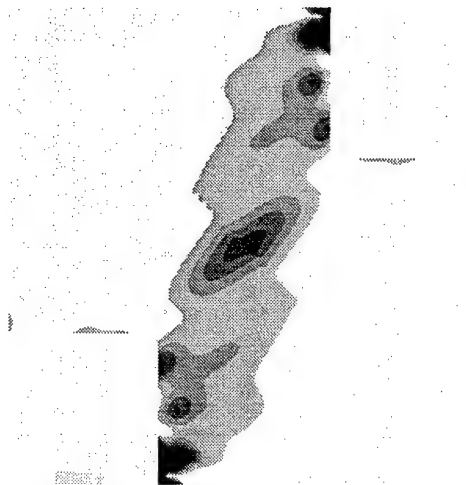
(a)



(b)



(c)



(d)

Figure 3.3: Equivalent plastic strain (%) distribution at  $\bar{\epsilon}_{yy} = 2\%$  for (a) 50% cracked inclusion, (b) 100% cracked inclusion, (c) 50% split inclusion and (d) 100% split inclusions.

microstructural topology through the onset and evolution of particle cracking in more complex, computer simulated and real microstructures. For undamaged Voronoi elements, the matrix stress function  $\Phi^m$  in equation (3.3) consists of 34 terms with 25 polynomial terms  $\Phi_{poly}^m$  ( $p + q = 2..6$  in equation 3.4) and 9 reciprocal terms  $\Phi_{rec}^m$  ( $i = 1..3, p = 0..2, q = 2 - p$  in equation 3.5). The inclusion stress function  $\Phi^c$  consists of 25 polynomial terms  $\Phi_{poly}^m$  ( $p + q = 2..6$  in equation 3.5). Fewer reciprocal terms are used than in the previous example due to the smooth interface for circular inclusions. For cracked elements though, the additional reciprocal terms are the same as those in the previous example, i.e. ( $i = 1..3, p + q = 2..4$  in equation 3.6).

### 3.4.1 Computer simulated microstructures

The effect of particle clustering on damage evolution is studied with two computer generated microstructural distributions as follows.

- (a) *A hard core distribution*: which is generated as a variant of a pure random Poisson pattern through the imposition of two constraints, namely (a) no two inclusions are allowed to overlap, and (b) all inclusions are completely contained within the region window.
- (b) *A single cluster hard core distribution*.
- (c) *Triple cluster hard core model*, where clusters are characterized by reduced average inclusion separation distance in an otherwise hard-core region.

Each RME consists of 50 equi-sized circular Si particles dispersed in an Al-Si-Mg alloy matrix, and constituting a 20% volume fraction. Pertinent dimensions are : RME size =  $200\mu \times 200\mu$ , particle diameter =  $14.2\mu$ , cluster diameter in (b) =  $33.38\mu$  and cluster diameter in (c) =  $25.78\mu$ . Details of the generation process are described in [27].

### Characterization

Statistical functions of geometric descriptors, which can discriminate between patterns, as discussed in [27, 28], are considered. Figures 3.4.1(a and b) show the cumulative distribution function  $F(A)$  and the probability density function  $f(A)$  of the local area fraction, measured as the ratio of the particle size to the area of the associated Voronoi cell. The range of  $A$  for hard core pattern is significantly shorter than for clustered patterns and thus the difference in  $F(A)$  increases with increasing area fraction. The high spike in  $f(A)$  for the hard core pattern is a consequence of the steep gradients due to pronounced uniformity in local area fraction, and the intensity of these spikes diminishes with clustering. The cumulative distribution function  $F(d)$  and density distribution functions  $f(d)$  for center to center nearest neighbor distances are plotted in figures 3.4.1(c and d). The longer plateaus in  $F(d)$  and the corresponding zeros in  $f(d)$  for clustered patterns are for the distances for which a near neighbor does not exist. Spikes in  $f(d)$  are much more pronounced for the hard-core distribution due to large number of neighbors at nearly similar distances. The lowest  $d$  values are much smaller for the clustered patterns. Second order intensity function  $K(r)$ , defined as the number of additional points expected to lie within a distance  $r$  of an arbitrarily located point divided by overall the point density, is an informative descriptor and has been discussed in [22, 27, 28]). Additionally, the pair distribution function  $g(r) = \frac{1}{2\pi r} \frac{dK(r)}{dr}$ , corresponds to the probability  $g(r)dr$  of an finding an additional point within a circle of radius  $dr$  and centered at  $r$ . The two functions are plotted for the patterns in figure (3.4.1e and f) and compared with a pure Poisson process for which  $K(r) = \pi r^2$  and  $g(r) = 1$ . With increased in clustering,  $K(r)$  deviates from that for the Poisson process. The peaks in  $g(r)$  are more pronounced for the hardcore



distribution indicating a greater likelihood of encountering additional particles at lower radii for this volume fraction.

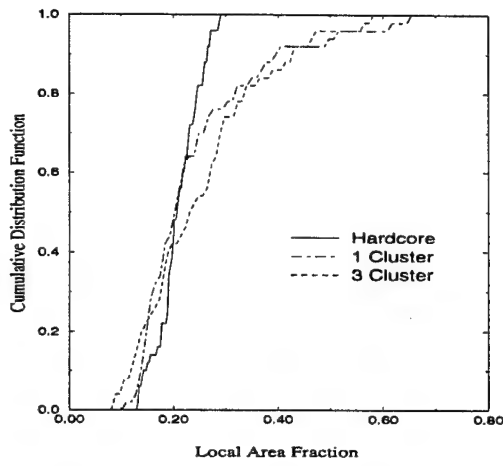
### Damage Simulation

Both complete particle cracking and particle splitting are analyzed in this example, with initially undamaged particles. Constituent material properties are as follows:

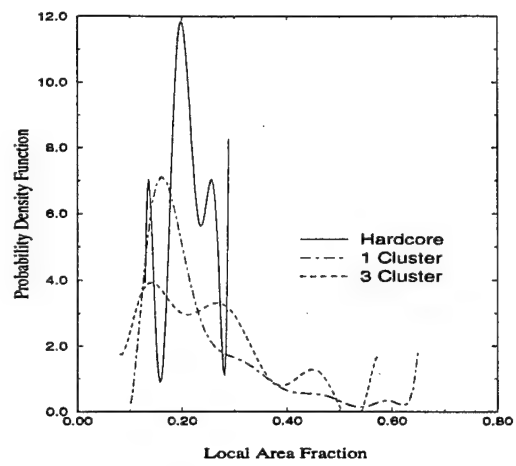
For the Al-Si-Mg matrix: Young's modulus  $E = 69$  GPa, Poisson's ratio  $\nu = 0.33$ , and the post yield elastic-plastic behavior is obtained from data on B-treatment matrix material in figure (5-1) (page 137) of Hunt [22]. For the Si inclusions: Young's modulus  $E = 161$  GPa, Poisson's ratio  $\nu = 0.2$ . All particles are of identical shape and size, and therefore a constant critical stress to failure  $\sigma_{cr} = 300$  MPa is assumed. The RME's are subjected to a macroscopic horizontal tensile strain that increases from 0 to a maximum of  $\bar{\epsilon}_{xx} = 2\%$ . Evolving damaged configurations by particle splitting are shown in figures (3.5a-f). For the hard core pattern, the first set of particles crack at  $\bar{\epsilon}_{xx} = 0.6\%$ . Particle cracking occurs at random locations with increased loading upto a strain of  $\bar{\epsilon}_{xx} = 1.6\%$ , after which no additional cracking is noticed. Large plastic strains occur in regions near the crack tips. However due to the lack of close proximity of cracked particles, plastic strain regions were not observed to propagate in any preferred direction. In contrast, for the triple cluster microstructure in figure 3.5d-f, the first set of particles crack and split within the cluster near the top-right corner at  $\bar{\epsilon}_{xx} = 0.4\%$ . With increased loading, high stress concentration at the crack tips lead to progressive cracking of other particles inside this cluster before particles in other clusters begin to crack. However if only particle cracking is allowed, particles in both the top right and bottom center clusters begin to crack almost concurrently. Particles in the third cluster remain relatively undamaged during the entire process. At the final strain  $\bar{\epsilon}_{xx} = 2.0\%$ , most particles in the two clusters are split while damage in the third cluster has just begun. During the initial stages of deformation and splitting, localized plastic straining occurs in the top right cluster which propagates from one crack tip to the next within the cluster by linking. Plastic straining in other clusters are less pronounced during this period. With subsequent particles splitting, plastic straining intensifies in bottom-center cluster and eventually links up with strained regions in the top cluster. High strain regions are much more diffused in the case of particle cracking and occur at higher macroscopic stresses compared to the particle splitting case.

Macroscopic stress-strain responses of the hard core and triple clustered RMEs are illustrated in figure (3.4.1). Abrupt drops due to particle cracking are smoothed in this figure. The stress level for the hard core pattern with particle splitting continues to drop throughout the loading. For the clustered microstructure, drops are higher in the initial stages due to rapid failure in the clusters, followed by increase in the stress levels due to matrix hardening. In general the RME with cracked particles projects a considerably stiffer behavior when compared to that with split particles. The effect of spatial distributions on damage evolution is studied through *marked correlation functions*  $M(r)$  introduced in Pyrz [22] and used in [27, 28]. Two marks associated with each particle are considered for their relevance to damage evolution. They are: (a) a parameter  $R_{ps}$  which is defined as the ratio of the maximum principal stress to the critical failure stress  $\sigma_{cr}$  for an undamaged particle, and as the ratio of the current overall strain to the strain at which the particle had cracked, for a cracked particle ( $\frac{\sigma}{\sigma_{cr}} = 1$ ).  $R_{ps}$  signifies the propensity to advance the damage state in the microstructure; and (b) the average effective plastic strain  $\bar{\epsilon}^p$  in each Voronoi cell, which

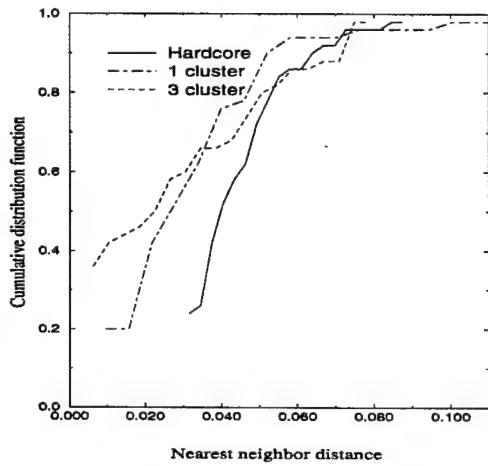




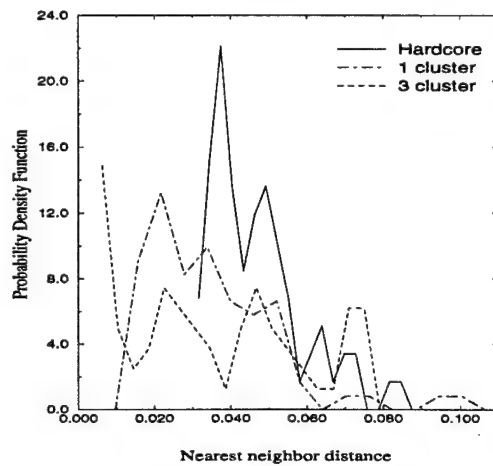
(a)



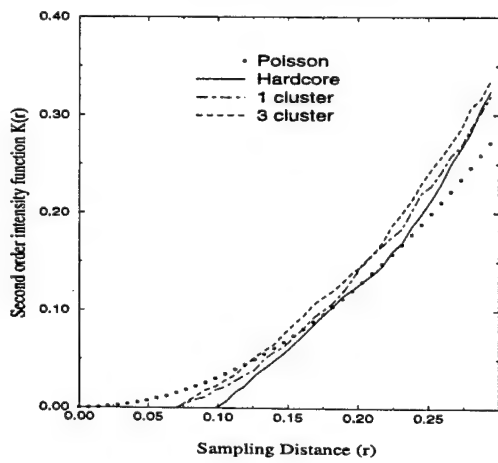
(b)



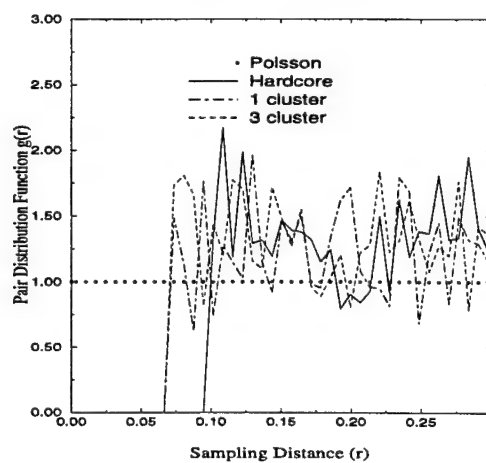
(c)



(d)



(e)



(f)

Figure 3.4: (a) Cumulative distribution and (b) Probability density functions of local area fractions; (c) Cumulative distribution and (d) Probability density functions of nearest neighbor distance; (e) Second order intensity and (f) Pair distribution functions for computer simulated microstructure.

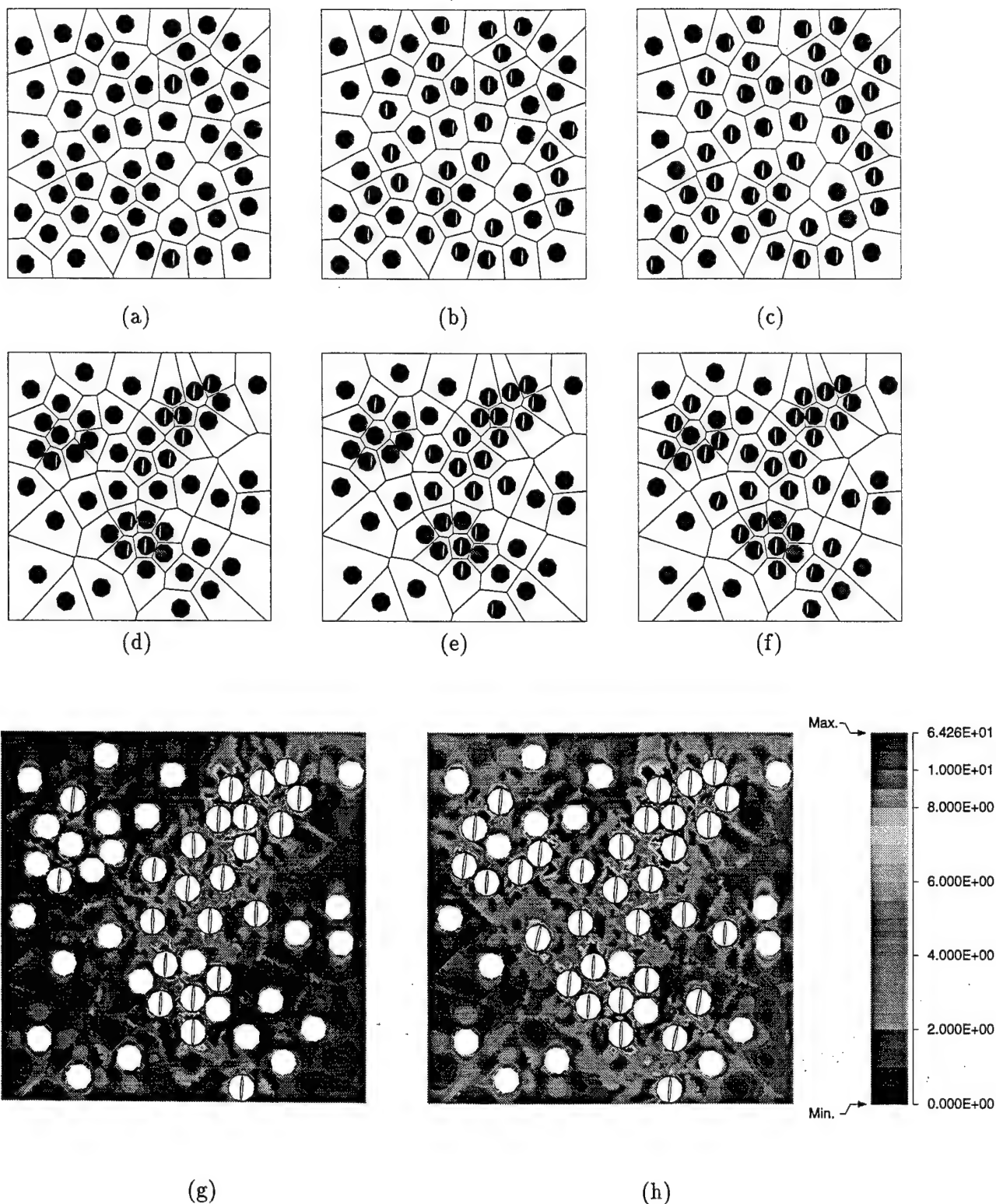


Figure 3.5: Damage configurations of hard core microstructure at (a)  $\bar{\epsilon}_{xx} = 0.8\%$ , (b)  $\bar{\epsilon}_{xx} = 1.4\%$  and (c)  $\bar{\epsilon}_{xx} = 2.0\%$ . Damage configurations of triple cluster microstructure at (d)  $\bar{\epsilon}_{xx} = 0.8\%$ , (e)  $\bar{\epsilon}_{xx} = 1.4\%$  and (f)  $\bar{\epsilon}_{xx} = 2.0\%$ ; Corresponding effective plastic strains(%) for triple cluster microstructure at (g)  $\bar{\epsilon}_{xx} = 1.4\%$  and (h)  $\bar{\epsilon}_{xx} = 2.1\%$ , for particle splitting with  $\sigma_{cr} = 300\text{MPa}$ .

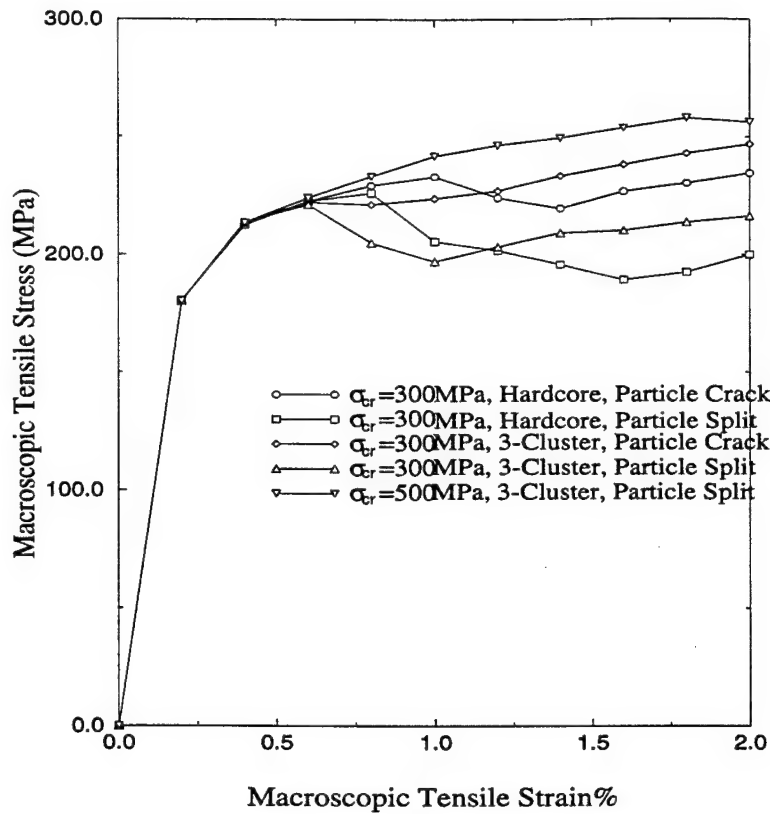


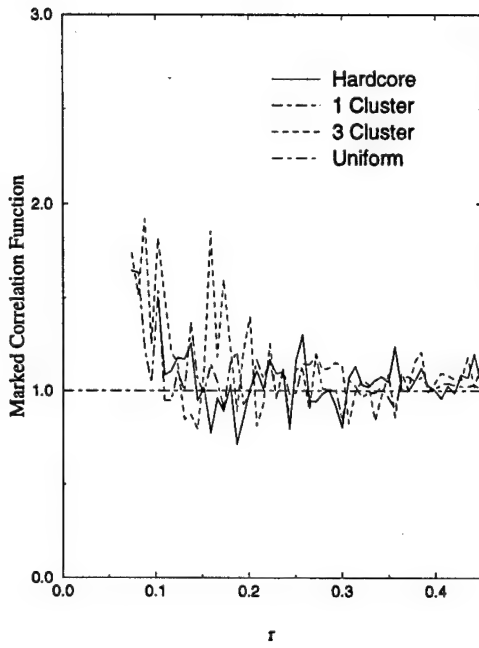
Figure 3.6: Macroscopic stress-strain response for computer generated microstructures due to particle cracking and splitting.

characterizes evolving matrix failure due to presence of damaged particles.

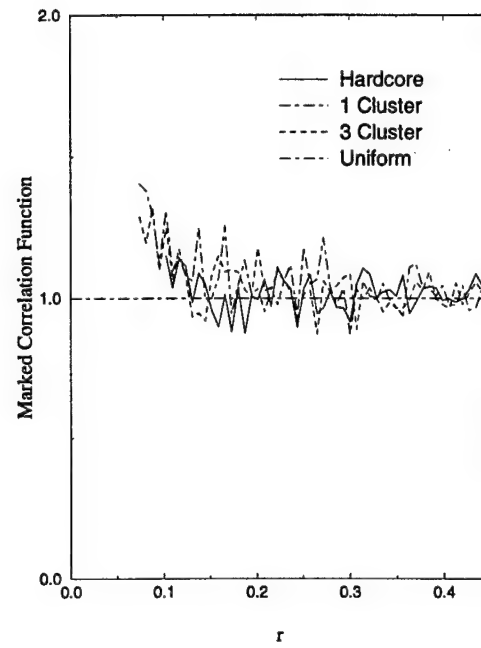
The marked correlation function  $M(r)$ , for which a mathematical formula is presented in [22], establishes the effect of microstructural morphology on the mark.  $M(r)$  for the two patterns and for a uniform microstructure ( $M(r)=1$ ) are compared in figure 3.4.1. For the hard core pattern the functions rapidly decay to unity, but for the clustered patterns the decay is considerably slower. Higher  $M(r)$  values for clustered patterns at short range sampling distances  $r$  represent larger influence of the damage marks. The high value of  $M(r)$  for  $\bar{\epsilon}^p$  at short sampling distances indicates severe matrix straining near damaged particles. The slower attenuation of  $M(r)$  for  $R_{ps}$  at short to medium range indicates that particle cracking is a major mode of damage evolution. This function is effective in understanding the sensitivity of damage variables to local perturbations in the morphology, and can provide a criterion for determining the optimal RME size.

### 3.4.2 Particle splitting simulation with actual micrographs

In this example, VCFEM analyses is conducted with micrographs obtained from serial sectioning of reinforced Al-Si-Mg alloys containing  $\approx 10\%$  or  $20\%$  by volume of Si particulates (see [29]). The material is developed at ALCOA Technical Center by rapid solidification of fine powders using a gas atomization process [22], to achieve equiaxed Si particles. The powder is consolidated by cold isostatic compaction, canned and degassed at  $454^\circ\text{C}$ , and finally consolidated to full density by hot isostatic pressing. Two types of microstructure are considered, viz. (a) a naturally aged  $20\%$  volume fraction composite with mean Si particle size of  $4.4\ \mu\text{m}$ , and (b) a naturally aged  $10\%$  volume fraction composite with mean Si particle size of  $3.9\ \mu\text{m}$ . Serial-sectioning of the specimens yield a series of 2-D sections as discussed in [29], which are then digitized.



(a)



(b)

Figure 3.7: Marked correlation function for (a) ratio of maximum principal stress to critical failure stress ( $\sigma_{cr}$ ) (b) average effective plastic strain in each Voronoi cells, for computer simulated microstructure.

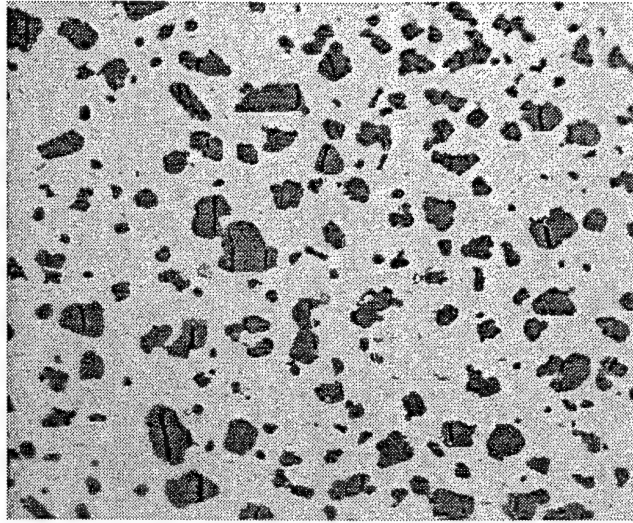
## Characterization

Equivalent microstructures that closely approximate the actual 2-D morphology of micrographs and yet are computationally less intensive are generated. In this process each particle of arbitrary shape is replaced by an equivalent ellipse, constructed by equating the 0-th, 1-st and 2-nd moments of the actual particles with those of the equivalent ellipses. The moments of actual particle are computed as the sum of moments of each pixel contained within the particle, while the moments of the ellipse are represented in terms of standard geometrical parameters. The procedure yields (i) the centroid  $(x_c, y_c)$ , (ii) lengths  $(a, b)$  of the major and minor axes, and (iii) angular orientation  $\theta$  of the major axis of the equivalent ellipse, details of which are discussed in [21]. An optical micrograph of a section, overlapped simulated and exact microstructures, and the Voronoi cell mesh obtained by surface to surface tessellation, are presented in figures (3.4.2a, b, and c) respectively.

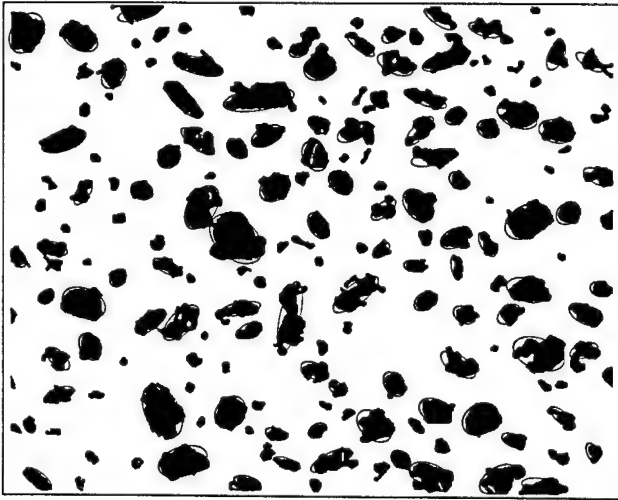
Two sections of each volume fraction 10% and 20% are analyzed. The  $V_f = 10\%$  sections have 77 and 89 Si particles, while the  $V_f = 20\%$  sections contain 97 and 106 Si particles. A majority of computer results are explained with respect to sections of the 20%  $V_f$ , for which the microstructural element has dimensions of  $205\mu \times 180\mu$ , and the two dimensional area fractions for the sections are calculated to be  $\approx A_f = 18.6\%$  and  $A_f = 18.9\%$  respectively (note that the 3-D  $V_f \sim 20\%$ ). Particle size distribution histograms (not shown) show considerable scatter within each section and also between sections. Cumulative ( $F$ ) and probability density distribution ( $f$ ) functions of the local area fraction ( $A$ ) and near-neighbor distance ( $d$ ) are plotted in figures 3.4.1(a,b,c and d). A comparison of the distribution functions in figures 3.4.1 reveal that the particle distribution is more in line with the hard-core pattern. Similar observations are also made in the plots of the second order intensity function  $K(r)$  and the pair distribution function in figure 3.4.1, where the absence of local peaks in  $g(r)$  signals negligible clustering. These observation is consistent with the material fabrication process innwhich the Si particulates are randomly precipitated from the mixture.

## Damage Simulation

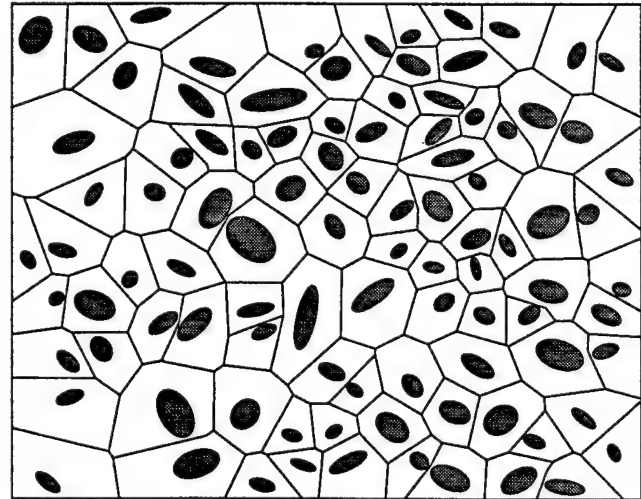
Material properties of the constituents are: For the Al-Si-Mg matrix: Young's modulus  $E = 69$  GPa, Poisson's ratio  $\nu = 0.33$ , and the post yield elastic-plastic behavior (non-linear isotropic hardening) is obtained from data on T4-matrix presented in figure (8) of Kiser et.al. [24]. For the Si inclusions: Young's modulus  $E = 161$  GPa, Poisson's ratio  $\nu = 0.2$  and mode I critical stress intensity factor for pure Si is found to be  $K_{IC} = 0.6 \text{ MPa}\sqrt{m}$ . In the fracture mechanics approach for determining the size dependent critical fracture stress  $\sigma_{cr}$  in equation (3.9), the initial flaw size  $c$  is assumed to be proportional to the average equivalent particle diameter of  $D_{avg}$ . The proportionality constant  $e$  is calibrated by analyses of auxiliary RMEs created from micrographs of other sections of the specimen. A comparison is made between the computer simulations and experimental observations with micrographs for (a) the number of cracked particles and (b) overall stress-strain behavior. The estimate is obtained to be  $e = \frac{c}{D} = .125$  or 12.5%, and therefore the critical stress to fracture is taken to be  $\sigma_{cr} = \frac{K_{IC}}{\sqrt{.125D} \pi}$ . For the approach with Weibull distribution, the two micrographs of 10%  $V_f$  are used for calculating parameters  $\sigma_{cr}$  and  $m$ , since they exhibit the onset of particle cracking at  $\bar{\epsilon}_{xx} = 3\%$ . The cross-sectional area  $A$  of each individual particle is calculated from the data on ellipses in figure 3.4.2(d). The maximum principal stress  $\sigma_I$  at  $\bar{\epsilon}_{xx} = 3\%$  is obtained from VCFE analysis without any particle damage. The probability of failure  $P_f(A, \sigma)$  in equation (3.10) is assumed to be  $\geq 0.95$ . The Weibull parameters are evaluated to be  $m = 2.37$  and  $\sigma_{cr} = 2.12$  GPa, by comparison with the micrograph observations and by fitting the



(a)



(b)



(c)

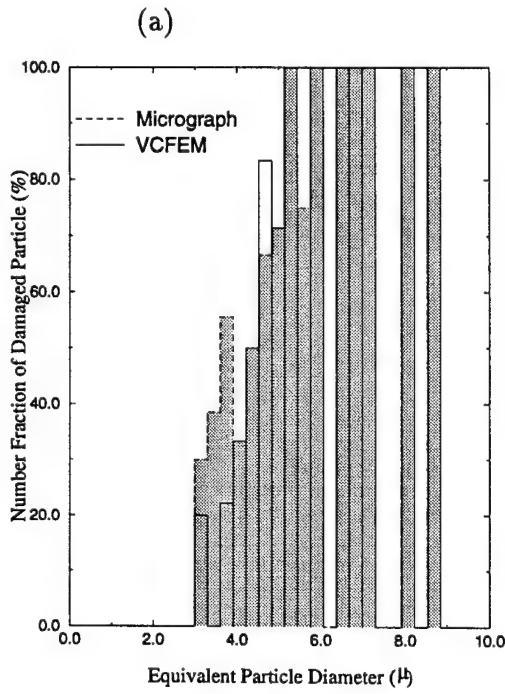
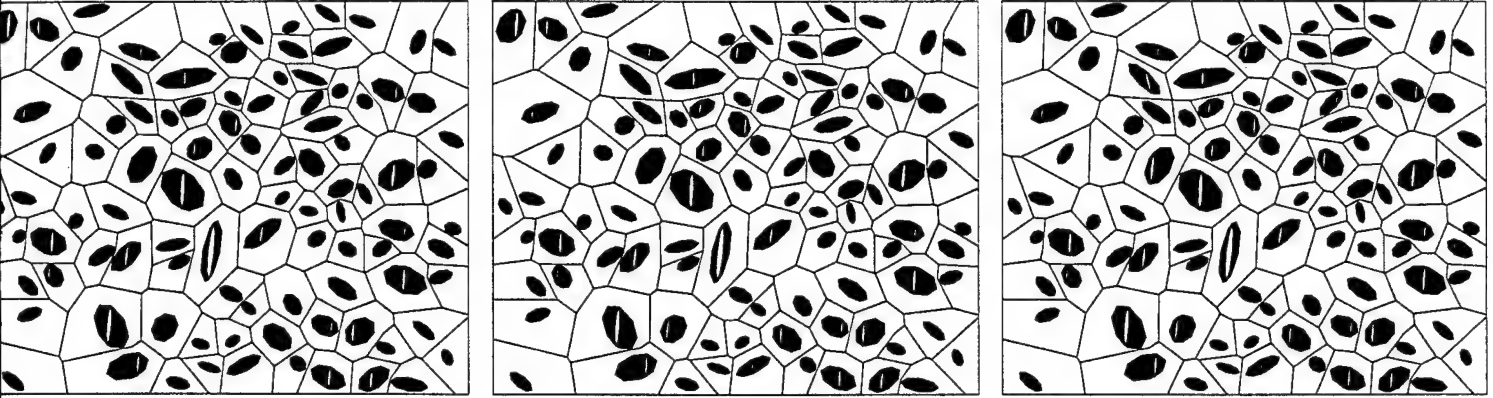
Figure 3.8: (a) Optical micrograph of a section of Al-Mg-Si composite ( $\text{Si } V_f = 20\%$ ) (b) simulated microstructure superimposed on the micrograph (c) Voronoi cell mesh resulting from tessellation.

data in a least-square sense. The probability function  $P_f$  of individual particles indicate that both particle size and stress levels contribute independently towards cracking. A qualitative comparison between the two approaches for evaluating critical stress, is made by VCFEM analysis with the 20% $V_f$  section of 97 particles strained to  $\bar{\epsilon}_{xx} = 6\%$ . Progression of damage in the microstructure with increasing strain is shown in figure (3.4.2a,b and c). Particles colored black are cracked while the grey particles are uncracked. A comparison of the fraction of different sized particles that are cracked by each approach, is made with actual micrographic observation (figure 3.4.2a) in histograms (3.4.2d and e). The fractions for the actual micrograph are shown in grey with dashed outline. The histograms indicate that while both criteria are good for large particles, the Weibull distribution based approach provides a better agreement with the micrographs at the smaller size range. Hence, it is used in all subsequent simulations.

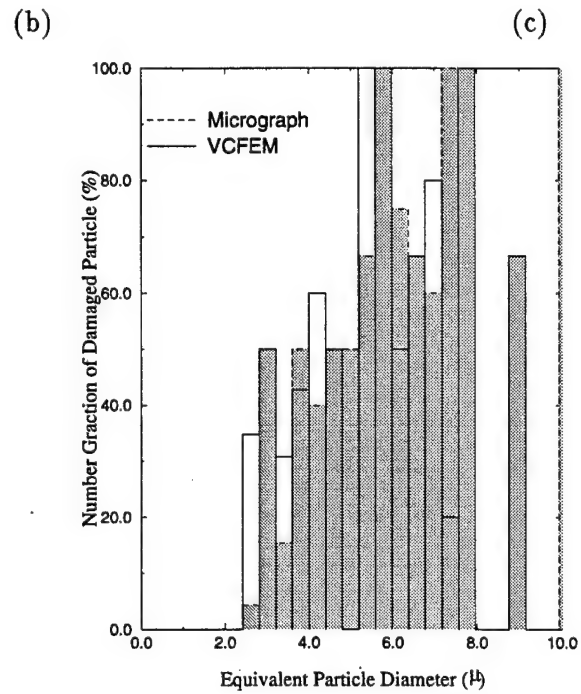
A damage parameter is defined as  $\rho = \frac{\text{Area of Cracked Particles}}{\text{Total Area of All Particles}}$ , which accounts for size, is plotted in figure 3.4.2a for each of the two sections of the  $V_f = 10\%$  & 20% composites as a function of increasing strain. Experimental values of the corresponding damage parameter are given in Hunt[22], where the areas are calculated by sectioning after straining to a certain level. Consequently a single data point is obtained from each specimen. Three experimental data points are plotted for the  $V_F = 20\%$  composite, while the  $V_F = 10\%$  has a single data point. Generally a good agreement is noted between simulated results and experimental data for the  $V_f = 20\%$  composite. Stress-strain response of nearly undamaged microstructures are shown in figure 3.4.2b by loading RMEs in compression to an average strain of  $\bar{\epsilon}_{xx} = 6\%$ . While the elastic response are not very different, the 20% $V_f$  composite has higher yield stress and higher flow stress than the 10% $V_f$  composite. The tensile response with particles cracking according the Weibull criterion is shown in figure 3.4.2 c. Results of VCFEM analyses for each volume fraction are averaged over the two sections and are compared with experimental results of Kiser and Zok [24]. While VCFEM analysis is in 2-D and the experimental results are for 3-D, the comparisons have a good qualitative agreement. The cross-over point at which the 20% $V_f$  composite becomes less stronger than the 10% $V_f$  composite, is approximately at  $\bar{\epsilon}_{xx} \approx 1.2 - 1.8\%$ , and compares well with the experimental value of  $\bar{\epsilon}_{xx} \approx 1.8\%$ . The stress capacity is in general higher for VCFEM predictions, which may be attributed to the constrained plastic flow arising from plane strain constraints. Additionally, the present simulation does not allow matrix softening which can also lower the load capacity. The stress-strain behavior of a uniform (square edge) microstructure with a single circular inclusion of volume fractions 10% and 20% are also plotted. The 10% uniform composite does not crack for the range of strains considered and predicts a stiff response. Failure of the single particle in the 20% $V_f$  composite results in an abrupt drop in load capacity and yields unreasonable predictions.

Contour plots of particle failure probability and effective plastic strains for the 20% $V_f$  composite are illustrated in figures (3.4.2) and (3.4.2) respectively. Damaged particles are in white with cracks in figure (3.4.2), and the contour plots are for undamaged particles indicating the likelihood of damage. An interesting observation made from these plots is that some large particles which exhibit a higher tendency to crack at early stages of loading, may remain intact throughout due to failure of neighboring particles and load redistribution. This phenomenon, also noticed with particle clusters in the previous example, illustrates the influence of evolving microstructural morphology on the propagation of damage. A particle crack induces large plastic flow in the neighboring matrix which causes the stress to rise in particles in this region and eventually initiate a crack. The plastic strain distribution in figure (3.4.2 a) shows localized bands of severe deformations emanating from crack





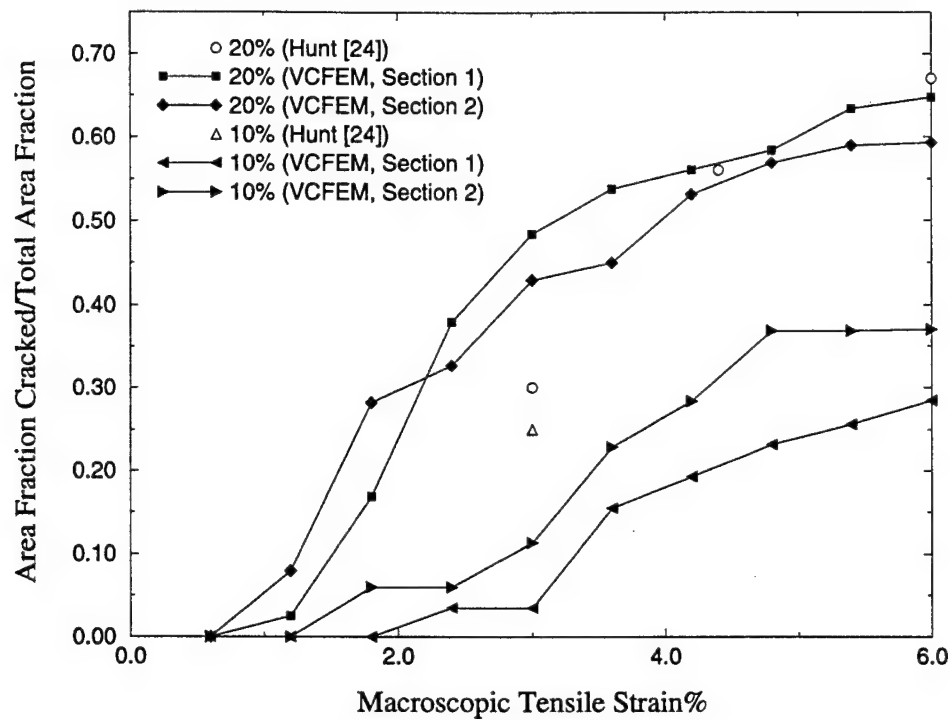
(d)



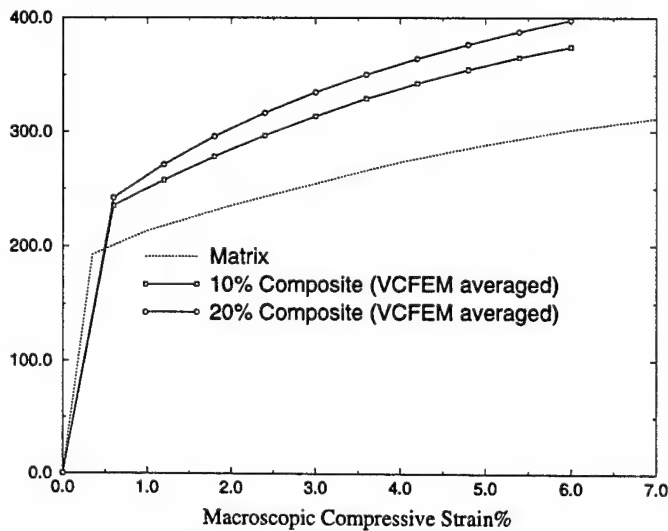
(e)

Figure 3.9: Simulated configurations of evolving damage at (a)  $\bar{\epsilon}_{xx} = 3.0\%$ , (b)  $\bar{\epsilon}_{xx} = 4.2\%$  and (c)  $\bar{\epsilon}_{xx} = 6.0\%$  with a Weibull distribution based damage criterion; (d,e) Histograms of number of damaged particles at  $\bar{\epsilon}_{yy} = 6\%$ , by Weibull distribution and fracture mechanics based damage criteria respectively.

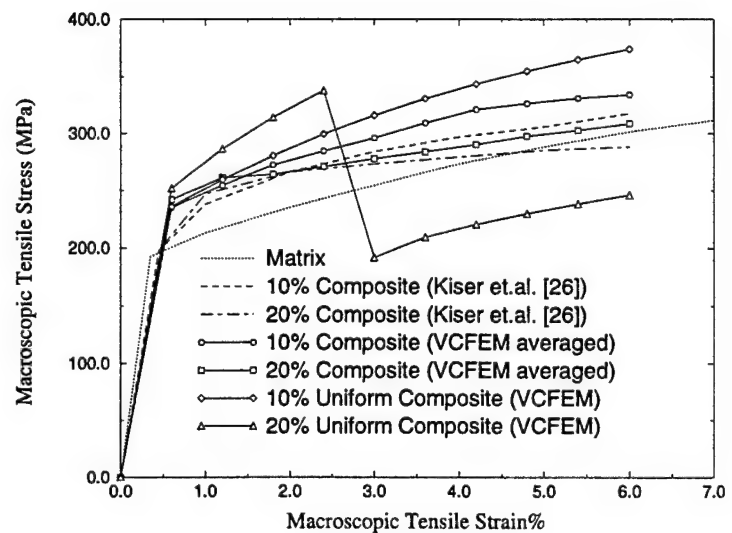




(a)



(b)



(c)

Figure 3.10: (a) Area fraction of cracked particles as a function of the macroscopic strain. Macroscopic stress-strain response for the Al-Si-Mg composite microstructures at two volume fractions (b) compressive response (c) tensile response.

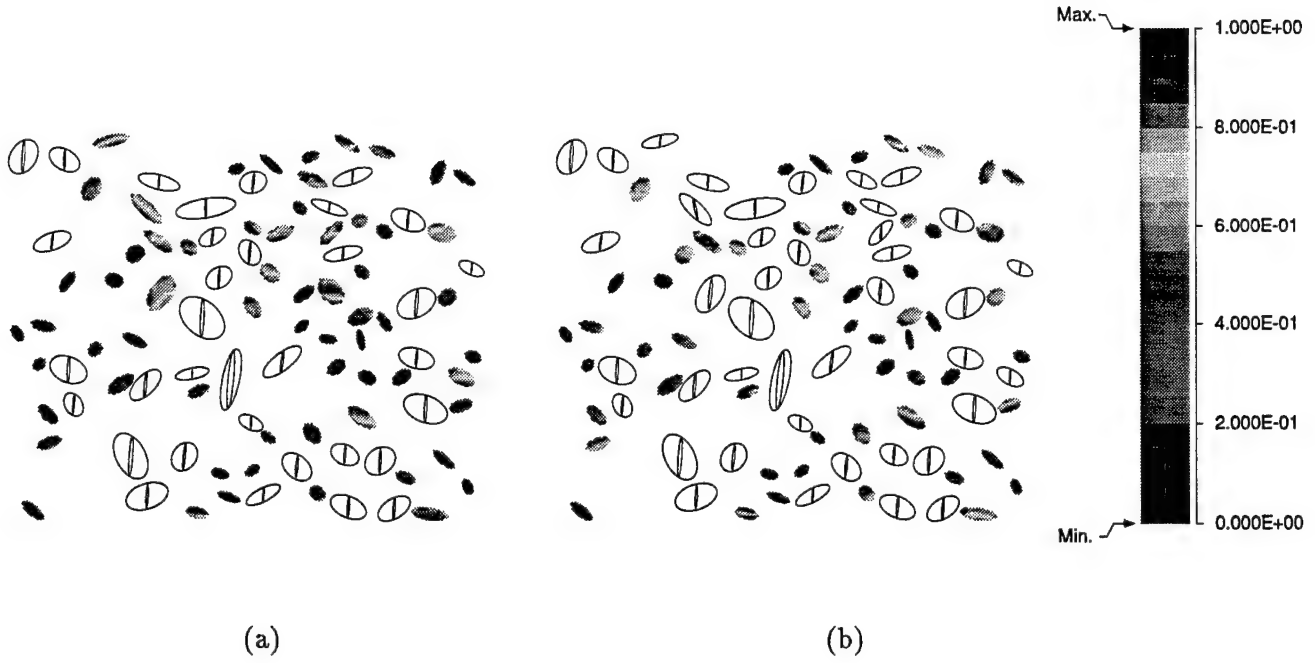


Figure 3.11: Contour plots of particle fracture probability by the Weibull damage criterion immediately before (a)  $\bar{\epsilon}_{xx} = 4.2\%$  and (b)  $\bar{\epsilon}_{xx} = 6.0\%$  for the Al-Si-Mg composite microstructure ( $V_f = 20\%$ ). (Damaged particles are in white with cracks).

tips and propagating to neighboring particles with cracks. The remainder of the matrix undergoes relatively smaller deformations. Marked correlation functions  $M(r)$  are plotted in figure (3.4.2) as functions of distance and particle shapes, for the two sections of  $20\%V_f$  composite. Two marks viz. (a) particle fracture probability  $P_f$  and (b) effective plastic strain  $\bar{\epsilon}^p$  are selected as qualitative indicators of microstructural damage. Uniform  $M(r)$  plots of unit value occur for regular patterns and correspond to identical marks. Figure (3.4.2a and b) of  $M(r)$  with respect to the sampling distance  $r$  shows that the functions for  $P_f$  quickly stabilize near the unit value, while the decay is slower for  $\bar{\epsilon}^p$  with a few abrupt peaks. The lack of strong clustering in these patterns leads to smaller influence regions for these microstructures. Marked correlation functions with respect to the relative difference in form factors  $F_f$  are plotted in figure (3.4.2c and d). The form factor is an indicator of the deviation in shape from a perfect circle ( $F_f=1$ ), and for an elliptical shape, may be expressed as (see [28]):

$$F_f = \frac{4\pi R^2}{\text{perimeter}^2} \quad ; \quad R = \sqrt{ab} \quad ; \quad \text{perimeter} \approx \pi[1.5(a+b) - \sqrt{ab}] \quad (3.11)$$

where  $a$  and  $b$  are the major and minor axes. The maximum observed form factor  $F_f$  is computed to be 0.97 while the minimum is 0.48. The figures (3.4.2c and d) depict increasing correlation functions especially for  $\bar{\epsilon}^p$ . This infers that shape has significant influence on the damage in these microstructures.

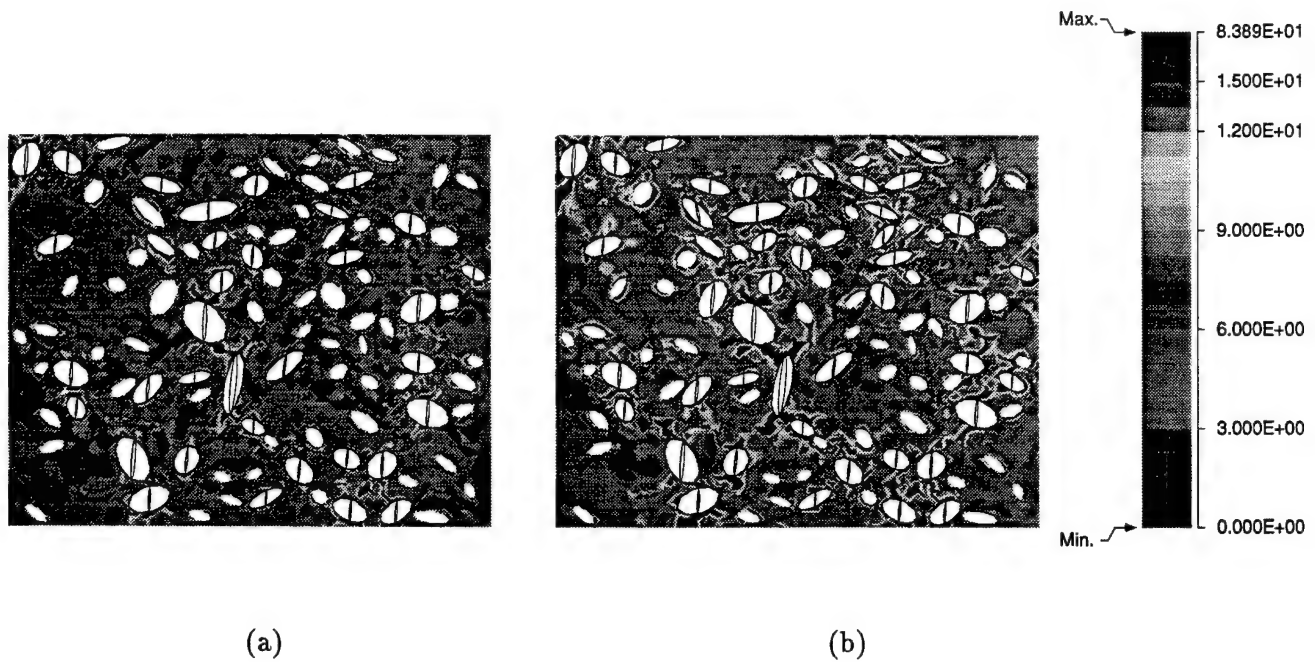


Figure 3.12: Effective plastic strain (%) contours at (a)  $\bar{\epsilon}_{xx} = 4.2\%$  and (b)  $\bar{\epsilon}_{xx} = 6.0\%$  for the Al-Si-Mg composite microstructure ( $V_f = 20\%$ ).

### 3.5 Conclusions

This work is devoted to stress analysis of non-uniform, ductile matrix composite microstructures with particle cracking, by the Voronoi Cell finite element method (VCFEM). The computational model assumes complete cracking at the onset of damage, and differentiates between the behavior of fully cracked particles and split particles. The uniqueness of this model lies in its ability to model, continuously changing element topology due to progressive material failure, with no user interference. Validation of the computation model for damage is done through various studies, including comparison with other numerical studies in the literature that use conventional finite element codes. These studies have predominantly analyzed simple uniform distributions with pre-existing cracks. Good agreement is obtained in these comparison studies, both from a macroscopic and microscopic point of view.

A major advantage of VCFEM is that it can be used for analyzing damage in nonuniform real micrographs without making major morphological simplifications. A set of computer generated hard-core and clustered microstructures are simulated to understand the effect of spatial distribution on damage evolution. Damage initiates within each cluster, propagates within the cluster and finally links up with damage in the neighboring clusters. Regions of severe plastic flow exist in the matrix ahead of split particles, indicating possible sites of matrix failure. Particle splitting is found to yield much softer overall response than particle cracking. In a concluding example, the VCFEM model is directly constructed from a digitized optical micrograph of an Al-Si-Mg compos-

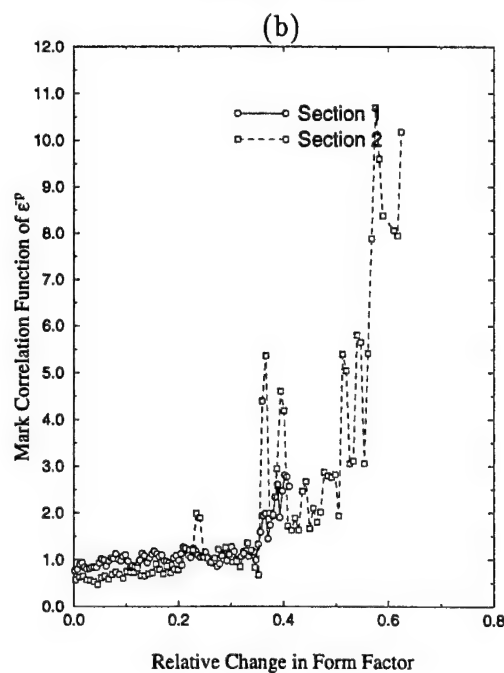
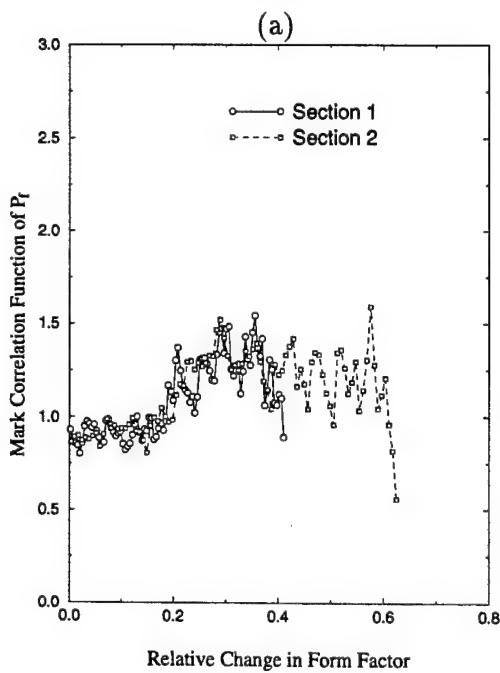
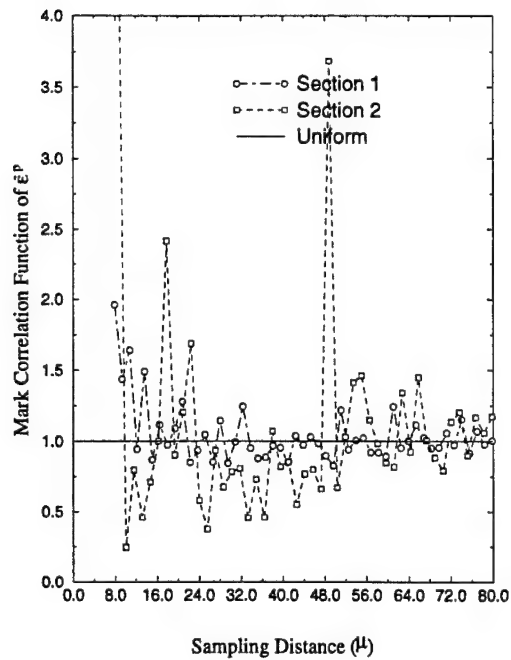
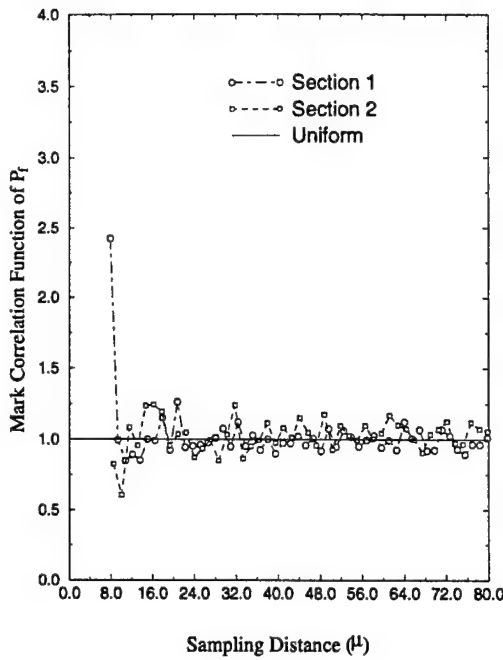


Figure 3.13: Marked correlation functions of (a) failure probability and (b) average effective plastic strain in each Voronoi cell as a function of radial distance, and marked correlation functions of (c) failure probability and (d) average effective plastic strain in each Voronoi cell as a function of form factor; for the Al-Si-Mg composite microstructure ( $V_f = 20\%$ ).

ite system. VCFEM results are compared with results of experiments with this material for two volume fractions. Good concurrence is obtained in the overall stress-strain behavior, as well as in the number of damaged particles in the microstructure. Larger particles tend to fail at lower load levels and therefore serve as sites of damage initiation. Nevertheless, smaller particles may also damage with loading, due to stereological factors like proximity with other particles and relative shape. It is noted that damage evolution in real microstructures is a gradual process, and takes place by progressive particle failure. Material behavior is therefore misrepresented with the single cell models where particle cracking result in abrupt changes in response. Statistical descriptors are used as indicators of morphological influence on the damage state. The efficiency of the VCFEM codes is noteworthy. A comparison with conventional FEM packages for undamaged-nonuniform and damaged-uniform materials show a  $\sim 30$ -50 times reduction in computing time. Currently, matrix cracking phenomenon is being incorporated in VCFEM and this will be reported in future.

# Bibliography

- [1] Y. Brechet, J.D. Embury, S. Tao and L. Luo, *Acta Metall. et Mater.*, **39**, 1781 (1991).
- [2] T. Christman, A. Needleman and S. Suresh, *Acta Metall. et Mater.*, **37**, 3029 (1989).
- [3] Z. Hashin, *Jour. Mech. Phys. Solids*, **36**, 719 (1988).
- [4] Y.-Z. Chen, *Eng. Fract. Mech.*, **38**, 379 (1984).
- [5] T.E. Lacy, D.L. McDowell and P.A. Willice, *ASTM* (submitted for publication).
- [6] C.F. Shih and R.J. Asaro, *J. Appl. Mech.*, **56**, 763 (1989).
- [7] A.G. Evans, B.J. Dagleish, M.Y. He and J.W. Hutchinson, *Acta Metall. et Mater.*, **37**, 3249 (1989).
- [8] A. Needleman, *J. Appl. Mech.*, **54**, 525 (1987).
- [9] A. Needleman, *J. Mech. Phys. Solids*, **38**, 289 (1990).
- [10] V. Tvergaard, *Jour. Mech. Phys. Solids*, **41**, 1309 (1991).
- [11] G. Bao, *Acta Metall. et Mater.*, **40**, 2547 (1992).
- [12] C.L. Hom, P.A. Mataga and R. M. McMeeking, *Int. Jour. Numer. Meth. Engrg.*, **27**, 233 (1989).
- [13] Y. Sugimura, P.G. Lim, C.F. Shih and S. Suresh, *Acta Metall. et Mater.*, **43**, 1157 (1995).
- [14] M. Finot, Y.-L. Shen, A. Needleman and S. Suresh, *Metall. Mat. Trans. A*, **25A**, 2403 (1994).
- [15] J.R. Brockenbrough, S.Suresh and W.A.Weinecke, *Acta Metall. et Mater.*, **39**, 735 (1991).
- [16] P.E. McHugh, R.J. Asaro and C.F. Shih, *Acta Metall. et Mater.*, **41**, 1461 (1993).
- [17] S. Moorthy and S. Ghosh, *Int. Jour. Numer. Meth. Engrg.*, **39**, 2363 (1996).
- [18] S. Ghosh and S. Moorthy, *Comp. Meth. Appl. Mech. Engrg.*, **121**, 373 (1995).
- [19] S. Moorthy and S. Ghosh, *Comp. Meth. Appl. Mech. Engrg.*, (in press), 1997.
- [20] N.I. Muskhelishvili, *Some Basic Problems in the Mathematical Theory of Elasticity*, P.Nordhoff Ltd., (1965).

- [21] S. Moorthy, Ph.D. Thesis, Ohio-State University (1997).
- [22] W.H. Hunt, *A thesis*, Carnegie Mellon University, (1992).
- [23] W.H.Hunt, J.R.Brockenbrough and P.E.Magnusen, *Scripta Metall. et Mater.*, **25**, 15 (1991).
- [24] M.T. Kiser, F.W. Zok and D.S. Wilkinson, *Acta Metall. et Mater.*, **9**, 3465 (1996).
- [25] W.A. Curtin, *Jour. Amer. Cer. Soc.*, **77**, 1075 (1994).
- [26] J.R. Brockenbrough and F.W. Zok, *Acta Metall. et Mater.*, **40**, 2547 (1993).
- [27] S. Ghosh, Z. Nowak and K. Lee, *Acta Metall. et Mater.*, **45**, No. 6, 2215 (1997).
- [28] S. Ghosh, Z. Nowak and K. Lee, *Comp. Sci. Tech.*, (in press).
- [29] M. Li, S. Ghosh, T.N. Rouns, H. Weiland and O. Richmond, (submitted for publication).
- [30] R. Pyrz, *Comp. Sci. Tech.*, **50**, 197 (1994).

## Chapter 4

# Multi-level Computational Model For Multiscale Damage Analysis In Composite And Porous Materials

### 4.1 Introduction

Heterogeneous structures with second phase inclusions or voids in the microstructure are conventionally analyzed with macroscopic properties obtained from homogenization of response at smaller (meso-, micro-) length scales. The mathematical homogenization theory, which uses asymptotic expansions of displacement, strain and stress fields about macroscopic values, has been used as a tool for analyzing multiple scale responses in [1, 2, 3, 4]. The method is based on assumptions of spatial periodicity of microscopic representative volume elements (RVE) and local uniformity of macroscopic fields within each RVE. It decomposes the multiscale boundary value problem into a decoupled set of micro-scale RVE problem and a macro-scale problem. Concurrent finite element analyses are executed at the each scale for information transfer between the scales. Multiple scale analysis of linear elastic reinforced composites by this method have been conducted by Fish et. al. [5, 6], Kikuchi et. al. [7, 8]. For nonlinear materials, the homogenization methods have been extended by Suquet [9], Fish et.al. [10], Guedes [11] and Cheng [12]. The method has also been implemented to simulate damage by fiber-matrix debonding in linear elastostatics [13] and fiber rupture using a phenomenological damage model [14].

Despite its advantages, asymptotic homogenization has suffered shortcomings arising from efficiency and accuracy considerations. Enormous computational efforts can result with this method due to the fact that at each integration point in the macroscopic model, boundary value problems of the microstructural RVE should be solved twice. To economize computations, many studies have assumed simple unit cells models of the microscopic RVE. Such idealizations may however be unrealistic for deformation and failure analysis of many materials. The homogenization method has another major limitation stemming from its basic assumptions, viz. (a) uniformity of the macroscopic fields within each RVE and (b) spatial periodicity of the RVE. The uniformity assumption is not appropriate in critical regions of high gradients, where the macroscopic fields can vary considerably. Free edges, interfaces, macrocracks, neighborhood of material discontinuities and most importantly



in the regions of evolving microscopic damage and instability are potential sites of nonuniformity. Furthermore, statistical periodicity implies that the RVE may be repeated to represent the entire neighborhood of a macroscopic point. For non-uniform microstructures sufficiently large portions should be considered as RVE for homogenization analysis. Unit cell models are severely limited in this respect. Even higher order theories of homogenization may be computationally unviable. A few effective global local techniques based on hierarchical decomposition and superposition of field variables have been proposed by Belytschko [15], Reddy [16] and Hughes [17]. Pagano and Rybicki [19] had discussed the breakdown of effective modulus theory for composite laminates with free edges and the need for global-local techniques. Fish et.al. [6, 18] have used global-local techniques with multigrid methods to extend the multiple scale modeling to non-periodic materials. Zohdi and Oden [20, 21] have developed a homogenized Dirichlet projection method (HDPM) which resolves the microstructural effects at different scales on the macroscopic response of heterogeneous structures.

To improve the accuracy of multiple scale analyses involving microstructural damage of elastic-plastic composite and porous structures without computational efficiency, an adaptive multi-level method is proposed in this work. It uses computational hierarchy in the different levels to concurrently predict evolution of variables at the structural and microstructural scales, as well as to track the incidence and propagation of damage. Analysis of microstructural response with arbitrary distributions, shapes and sizes of heterogeneities is conveniently done by the Voronoi Cell finite element model (VCFEM) [22, 23, 24, 25]. The VCFE model naturally evolves by tessellation of the microstructure, to generate a morphology based network of multi-sided Voronoi polygons. Each Voronoi cell with the embedded heterogeneity is treated as a FEM element in this model. Incorporation of micromechanics based assumptions into a hybrid finite element formulation imparts a high level of computational efficiency with sufficient accuracy and resolution in this method. Furthermore, pre-processing efforts in generating microstructural models are drastically reduced. Various thermo-elastic and elastic-plastic problems of composite and porous materials have been successfully analyzed by VCFEM [22, 24, 25]. Progressive damage by particle cracking has been done in [23] and VCFEM has been used to relate image analysis and quantitative characterization with microstructural response in [24]. For periodic representative volume elements (RVE) of elastic and elastic-plastic materials, the microstructural VCFEM has been coupled with structural analysis codes by using asymptotic homogenization in [26, 27]. When the method fails due to questionable assumptions of macroscopic uniformity and statistical periodicity, a combination of homogenization and global-local methods is a necessity. This implementation is a nontrivial undertaking due to lack of apriori knowledge of regions requiring differential resolution. The adaptive multi-level methodology developed in this work addresses this challenge. The model differentiates between non-critical and critical regions for which the model ranges from macroscopic computations using continuum constitutive relations to zooming in at 'hotspots' for pure microscopic simulations. The adaptive process significantly increases the efficiency while retaining appropriate level of accuracy in the hierarchy. The chapter begins with a discussion on two scale computations. It introduces three levels of the computational domain which include macro, macro-micro and microscopic analysis. Numerical examples are conducted for heterogeneous materials with a variety of microscopic architectures to support its development.

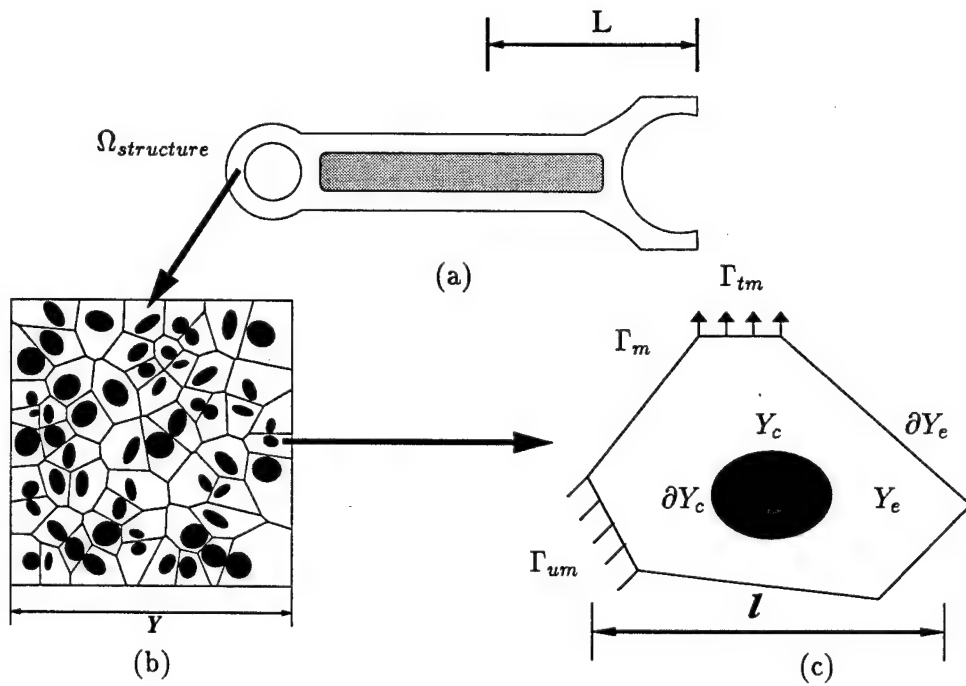


Figure 4.1: A heterogeneous structure showing various scales: (a) The structure at the macroscopic scale of applied loads (b) A representative volume element (RVE) at the microscopic scale with the VCFE model and (c) A Voronoi cell element at the scale of a single heterogeneity or basic structural element.

## 4.2 Two Way Coupling for Multiple Scale Modeling

Multiple scale modeling of heterogeneous materials is necessary to concurrently account for spatial variability at the macro- and micro-scales. An effective model of this class requires two-way coupling for efficient computing, as well as for accurate representation of the necessary variables at different scales. The first is a 'bottom up' coupling for determination of equivalent homogeneous behavior at a macroscopic point  $\mathbf{x}$ , as a function of the microstructural geometry and behavior of the constitutive phases, but independent of applied loads to the structure. In the homogenization procedure, an isolated representative volume element (RVE)  $\mathbf{Y}(\mathbf{x}) \subset \mathbb{R}^3$  is identified at microstructural scale of heterogeneities (figure 4.1b). The scale  $\mathbf{y}$  of the RVE domain  $\mathbf{Y}(\mathbf{x})$  may be large with respect to the characteristic length  $l$  of microscopic heterogeneities, but is significantly small compared to the macroscopic length scale  $L$  of the structure and applied loads. Homogenized variables at the macroscopic scale are obtained by volume averaging of variables in the RVE, following the definition

$$\langle f \rangle_Y = \frac{1}{Y} \int_Y f(y) dy \quad (4.1)$$

The condition for macroscopic homogeneity, according to the Hill-Mandel hypothesis [29], assumes equivalence of strain energy for the actual and equivalent homogenized media. Thus for a statically admissible stress field  $\boldsymbol{\sigma}(\mathbf{y})$  and kinematically admissible strain field  $\boldsymbol{\epsilon}(\mathbf{y})$ ,

$$\langle \boldsymbol{\sigma} : \boldsymbol{\epsilon} \rangle_Y = \langle \boldsymbol{\sigma} \rangle_Y : \langle \boldsymbol{\epsilon} \rangle_Y \quad \forall \mathbf{y} \in \mathbf{Y} \quad (4.2)$$

The microscopic stress  $\boldsymbol{\sigma}(\mathbf{y})$  and strain  $\boldsymbol{\epsilon}(\mathbf{y})$  fields satisfying the homogeneity condition (4.2) may be obtained by solving boundary value problems for the RVE  $\mathbf{Y}$  with prescribed homogeneous stress/strain or periodicity boundary conditions, stated as:

$$\mathbf{T}^b = \langle \boldsymbol{\sigma} \rangle_Y \cdot \mathbf{n}(\mathbf{y}) = \boldsymbol{\sigma} \cdot \mathbf{n}(\mathbf{y}) \text{ on } \partial \mathbf{Y} : \text{ Uniform Traction} \quad (\text{a})$$

$$\mathbf{u}^b = \langle \boldsymbol{\epsilon} \rangle_Y \cdot \mathbf{y} \text{ on } \partial \mathbf{Y} : \text{ Uniform Strain} \quad (\text{b})$$

$$\mathbf{u}^b = \langle \boldsymbol{\epsilon} \rangle_Y \cdot \mathbf{y} + \hat{\mathbf{u}} = \langle \boldsymbol{\epsilon} \rangle_Y \cdot \mathbf{y} + \hat{\mathbf{u}} + \mathbf{k} \hat{\mathbf{Y}} \text{ on } \partial \mathbf{Y} : \text{ Y-Periodicity} \quad (\text{c}) \quad (4.3)$$

where  $\mathbf{k}$  is an integer and  $\hat{\mathbf{Y}}$  is the basic period of the  $\mathbf{Y}$ -periodic displacement functions. The macroscopic constitutive equations are obtained by solving a boundary value problem of the RVE  $\mathbf{Y}$  with one of the three sets of boundary conditions in equation (4.3), followed by the averaging process in equation (4.1). For linear elastic constituent phases in  $\mathbf{Y}$ , the relation between the strain energy functions has been established in Suquet [30] as:

$$\langle \boldsymbol{\epsilon} \rangle : \mathbf{E}_{tr}^h : \langle \boldsymbol{\epsilon} \rangle \leq \langle \boldsymbol{\epsilon} \rangle : \mathbf{E}_{per}^h : \langle \boldsymbol{\epsilon} \rangle \leq \langle \boldsymbol{\epsilon} \rangle : \mathbf{E}_{str}^h : \langle \boldsymbol{\epsilon} \rangle \quad \forall \mathbf{E} \in \mathbb{R}^9 \quad (4.4)$$

where  $\mathbf{E}_{tr}^h$ ,  $\mathbf{E}_{per}^h$ ,  $\mathbf{E}_{str}^h$  are respectively the homogenized stiffness tensors evaluated with uniform traction, periodicity and uniform strain boundary conditions, and  $\langle \boldsymbol{\epsilon} \rangle$  is the macroscopic (applied or averaged) strain field. The discrepancy with the kinematic and kinetic boundary conditions reduce with increasing size of  $\mathbf{Y}$ . It is generally concluded [8], that for the same RVE size, the periodicity boundary conditions are expected to yield more accurate statistically homogenized constitutive parameters and macroscopic properties.

The other coupling is the ‘top down’ where the evolution of variables are evaluated in the microstructure from known macroscopic variables, by a process termed as *localization*. In those regions, where the microstructure may admit a RVE  $\mathbf{Y}$ , the microscopic variables can be evaluated by solving a boundary value problem with imposed macroscopic strains and the local periodicity condition in equation 4.3c. In other regions, where assumptions of local periodicity of the RVE may be unrealistic, the localization process will entail direct interfacing of the microstructural and macroscopic regions.

### 4.3 A Multi Level Model for Coupling Different Scales

In the spirit of true two way coupling of multiple scale problems, the computational domain is adaptively decomposed into three levels of hierarchy based on requirements of resolution. Such hierarchy is intended to increase computational efficiency as well as accuracy in concurrent prediction of variables at the continuum and microstructural scales. As proposed in [31], the model uses homogenization of microstructural RVE solutions to evaluate homogenized properties and cascades down the scales at hotspots of evolving damage. The three levels of hierarchy with requirements of increasing resolution (figure 4.2) are as follows.

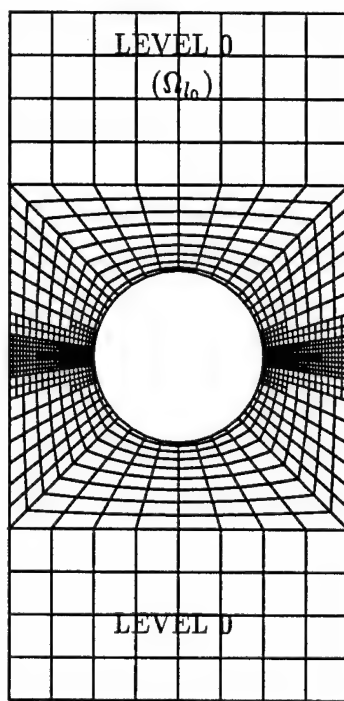
**•i. Computational Subdomain Level-0:**

These correspond to non-critical macroscopic regions in figure 4.2a, where deformation variables are relatively uniform and periodicity conditions may be assumed for the underlying material RVE. Scale effects are negligible in this region and local constitutive relations may be derived from postulates of the RVE approaching zero volume. Continuum level anisotropic plasticity constitutive relations, that are consistent with the actual microstructural constitution, are developed for macroscopic modeling of these regions.

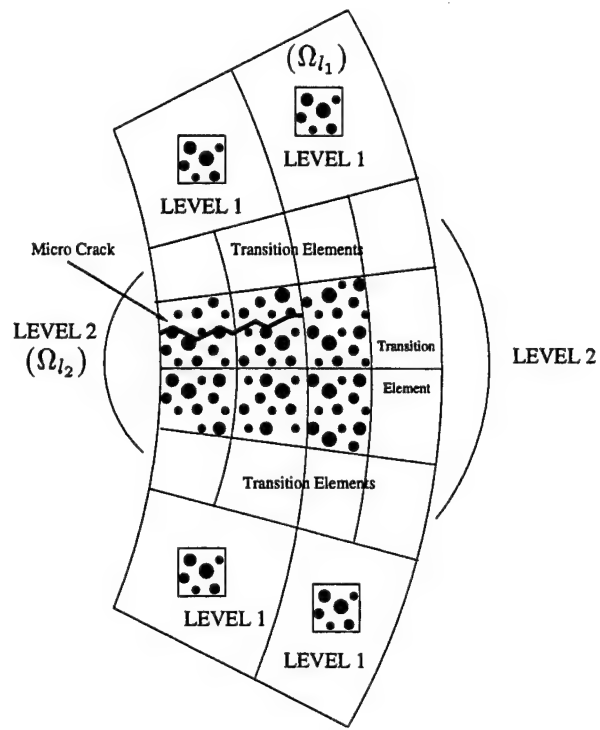
The *level-0* macroscopic simulations are accompanied by element refinement or *h-adaptation* for two reasons. The first is to identify and reduce a chosen ‘error measure’ in the macroscopic computational model. A second attribute is that it enables the computational model to ‘zoom in’ on regions of evolving nonuniformity due to microscopic non-homogeneity. This reduces the disparity in size of the macro- and micro- scale elements by successive refinement of macroscopic elements in the critical regions as shown in figure 4.2a.

**•ii. Computational Subdomain Level-1:** These are regions that face imminent microscopic non-homogeneity and resulting macroscopic nonuniformities (figure 4.2a,b). Though the computations are still macroscopic, concurrent monitoring of the development of damage and instabilities in the RVE is possible in this level. For concurrent macro- and micro- scale analyses the asymptotic homogenization methods, which is based on the existence of an RVE, is used. Macroscopic element refinement by *h-adaptation* continues for this level.

**•iii. Computational Subdomain Level-2:** These critical regions materialize with the evolution of microstructural damage in the form of evolved microcracks or instabilities (figure 4.2b), leading to high macroscopic field gradients. The assumptions of macroscopic uniformity and local periodicity are unrealistic. To realize scale effects, it is required that the level-1 macro-micro computational model switch to a completely microscopic model, encompassing large portions of the microstructure. A detailed flow chart of the adaptive hierarchical process is depicted in figure 4.3.



(a)



(b)

Figure 4.2: A hierarchical multi-level computational domain; Level-0 for macroscale continuum modeling (b) Level-1 for coupled macro-microscopic (RVE) modeling with asymptotic homogenization and (c) Level-2 for pure microscopic modeling

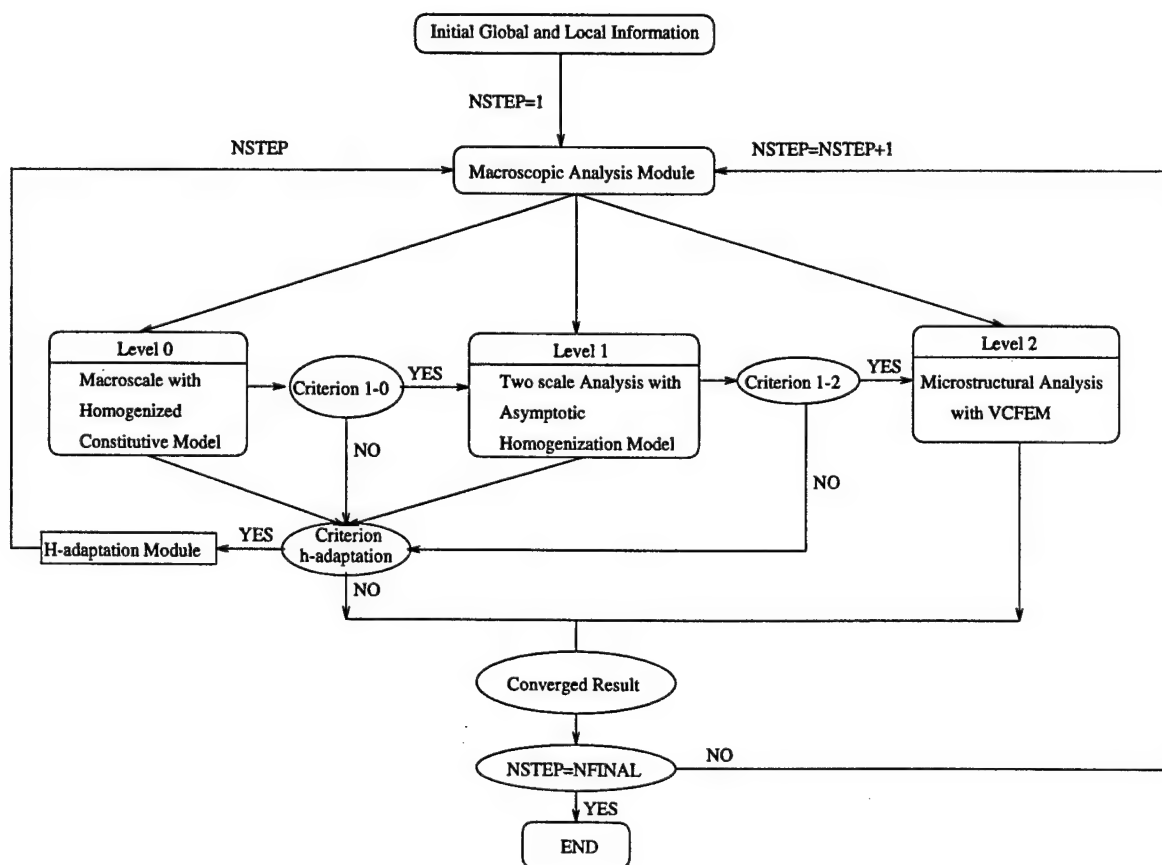


Figure 4.3: Flow chart of the sequence of operations in the multiple-scale model.

The substructured computational domain is delineated as an elastic-plastic body of material domain  $\Omega_{MAT}$  that consists of regions  $\Omega_{MAT(p)}$  for which the RVE is repeated periodically, and also of regions  $\Omega_{MAT(np)}$  where the periodicity assumptions do not hold, i.e.

$$\Omega_{MAT}(\mathbf{x}, \mathbf{u}) = \Omega_{MAT(p)}(\mathbf{x}, \mathbf{u}) \cup \Omega_{MAT(np)}(\mathbf{x}, \mathbf{u}) \quad (4.5)$$

The macroscopic regions of periodicity are further constituted of repeating a large number of RVE's  $\mathbf{Y}$ , i.e.

$$\Omega_{MAT(p)} = \cup_{k=1}^{N(p)} \bar{\mathbf{Y}}_k^{MAT(p)} \quad \text{where} \quad \bar{\mathbf{Y}}_k^{MAT(p)} = \cup_{l=1}^{\infty} \mathbf{Y}_k^l \quad (4.6)$$

Here  $N(p)$  corresponds to the number of different RVE's  $\mathbf{Y}_k^l$  in the periodic regions, and for all practical purposes,  $\infty$  corresponds to a sufficiently large number. The non-periodic region  $\Omega_{MAT(np)}$  is defined as the set of all microstructural regions for which the  $N(np)$  RVE's are not repeated, i.e.

$$\Omega_{MAT(np)} = \cup_{k=1}^{N(np)} \mathbf{Y}_k^{MAT(np)} ; \quad \mathbf{Y}_k \cap \mathbf{Y}_l = 0 \quad \forall k \neq l \quad (4.7)$$

The level-0 and level-1 of the computational domain  $\Omega$  correspond to the periodic regions, while the level-2 belongs to the non-periodic regions as

$$\Omega_{l0} \cup \Omega_{l1} \subset \Omega_{MAT(p)} ; \quad \Omega_{l2} \subset \Omega_{MAT(np)} \quad (4.8)$$

## 4.4 Homogenization with Voronoi Cell FEM

### 4.4.1 Asymptotic homogenization with microstructural periodicity

Consider a heterogeneous structure occupying a region  $\Omega_{structure}$  (figure 4.1a), for which the heterogeneous microstructure constitutes of spatially repeated RVE's  $\mathbf{Y}(\mathbf{x})$  about a macroscopic point  $\mathbf{x}$  as shown in figure 4.1b. The RVE is discretized into a mesh of Voronoi cells, which naturally evolve from the microstructure by Dirichlet tessellation. In the Voronoi cell FEM (VCFEM), each Voronoi cell represents a basic structural element (BSE) which is the neighborhood of a heterogeneity in the microstructure. The dimensions of the  $\mathbf{Y}(\mathbf{x})$  are typically very small in comparison with the structural dimensions  $L$ , i.e.  $\frac{L}{\epsilon}$  is a very small positive number  $\epsilon$ . Due to variation of evolutionary variables in a small neighborhood  $\epsilon$  of the macroscopic point  $\mathbf{x}$ , all variables are assumed to exhibit dependence on both length scales i.e.  $\Phi^\epsilon = \Phi(\mathbf{x}, \frac{\mathbf{x}}{\epsilon})$ , where  $\mathbf{y} = \frac{\mathbf{x}}{\epsilon}$ . The superscript  $\epsilon$  denotes association of the function with the two length scales and hence  $\Omega^\epsilon$  corresponds to a connected structural and microstructural domain. The assumption of periodic repetition of the microstructure about  $\mathbf{x}$  makes the dependence of the function on  $\mathbf{y}(= \frac{\mathbf{x}}{\epsilon})$ ,  $\mathbf{Y}$ -periodic [7, 4, 8, 14]. For small deformation elasto-plasticity, the rate forms of the equilibrium, kinematic and constitutive relations are given as:

$$\begin{aligned} \text{Equilibrium: } \dot{\sigma}_{ij,j}^\epsilon &= -\dot{f}_i, & \text{Kinematics: } \dot{\epsilon}_{kl}^\epsilon &= \frac{1}{2} \left( \frac{\partial \dot{u}_k^\epsilon}{\partial x_l^\epsilon} + \frac{\partial \dot{u}_l^\epsilon}{\partial x_k^\epsilon} \right) \\ \text{Constitutive: } \dot{\sigma}_{ij}^\epsilon &= E_{ijkl}^\epsilon \dot{\epsilon}_{kl}^\epsilon & \text{in } \Omega^\epsilon \end{aligned} \quad (4.9)$$

where  $\dot{\sigma}_{ij}^\epsilon(\mathbf{x}, \mathbf{y})$ ,  $\dot{\epsilon}_{ij}^\epsilon(\mathbf{x}, \mathbf{y})$  and  $\dot{u}_i^\epsilon(\mathbf{x}, \mathbf{y})$  are  $\mathbf{Y}$ -periodic rates of stress, strain and displacement fields respectively. Furthermore the boundary tractions and displacements are assumed to satisfy the following prescribed conditions.

$$\dot{\sigma}_{ij}^\epsilon n_j = \dot{t}_i \quad \text{on } \Gamma_t, \quad \dot{u}_i^\epsilon = \dot{u}_i \quad \text{on } \Gamma_u \quad (4.10)$$

where  $\mathbf{n}$  is the unit normal to the boundary. The  $\mathbf{Y}$ -periodic displacement rate or increment field is approximated by an asymptotic expansion about  $\mathbf{x}$  with respect to the parameter  $\epsilon$ :

$$\dot{u}_i^\epsilon(\mathbf{x}) = \dot{u}_i^0(\mathbf{x}, \mathbf{y}) + \epsilon \dot{u}_i^1(\mathbf{x}, \mathbf{y}) + \epsilon^2 \dot{u}_i^2(\mathbf{x}, \mathbf{y}) + \dots, \quad \mathbf{y} = \frac{\mathbf{x}}{\epsilon} \quad (4.11)$$

Noting that the spatial  $\mathbf{x}^\epsilon$  derivative of any function depends on the two length scales and is given as:

$$\frac{\partial}{\partial x_i^\epsilon} \left( \Phi(\mathbf{x}, \mathbf{y} = \frac{\mathbf{x}}{\epsilon}) \right) = \frac{\partial \Phi}{\partial x_i} + \frac{1}{\epsilon} \frac{\partial \Phi}{\partial y_i} \quad (4.12)$$

the stress rate tensor  $\dot{\sigma}_{ij}^\epsilon$  can be expressed as

$$\dot{\sigma}_{ij}^\epsilon = \frac{1}{\epsilon} \dot{\sigma}_{ij}^0 + \dot{\sigma}_{ij}^1 + \epsilon \dot{\sigma}_{ij}^2 + \epsilon^2 \dot{\sigma}_{ij}^3 \dots \quad (4.13)$$

where

$$\dot{\sigma}_{ij}^0 = E_{ijkl} \frac{\partial \dot{u}_k^0}{\partial y_l}, \quad \dot{\sigma}_{ij}^1 = E_{ijkl} \left( \frac{\partial \dot{u}_k^0}{\partial x_l} + \frac{\partial \dot{u}_k^1}{\partial y_l} \right), \quad \dot{\sigma}_{ij}^2 = E_{ijkl} \left( \frac{\partial \dot{u}_k^1}{\partial x_l} + \frac{\partial \dot{u}_k^2}{\partial y_l} \right) \quad (4.14)$$

From equations 4.9 and 4.13, and using the periodicity condition on the RVE boundary  $\int_{\partial \Gamma_Y} f \, d\Gamma_Y = 0$ , it can be proved (see [26, 27]) that

$$\dot{\sigma}_{ij}^0 = 0, \quad \dot{u}_i^0 = \dot{u}_i^0(\mathbf{x}) \quad \text{and} \quad \frac{\partial \dot{\sigma}_{ij}^1}{\partial y_j} = \frac{\partial}{\partial y_j} [E_{ijkl} \{ \frac{\partial \dot{u}_k^0}{\partial y_l} + \frac{\partial \dot{u}_k^1}{\partial y_l} \}] = 0 \quad (4.15)$$

Furthermore, by neglecting the terms associated with  $\epsilon$  or higher in equation (4.13), the constitutive relation in the  $\mathbf{Y}$ -domain is expressed as

$$\dot{\sigma}_{ij}^\epsilon = \dot{\sigma}_{ij}^1 = E_{ijkl} \dot{e}_{kl}^\epsilon = E_{ijkl} \left( \frac{\partial \dot{u}_k^0}{\partial x_l} + \frac{\partial \dot{u}_k^1}{\partial y_l} \right) \quad (4.16)$$

Here  $\dot{e}_{kl}^\epsilon$  is the microstructural strain rate tensor, for which  $\frac{\partial \dot{u}_k^0}{\partial x_l}$  is an averaged macroscopic part and  $\frac{\partial \dot{u}_k^1}{\partial y_l}$  is denoted as a fluctuating strain rate tensor [9]. Due to linearity of the rate problem,  $\dot{\sigma}_{ij}^1$ ,  $\dot{u}_i^1$  and the microscopic equilibrium condition can be expressed as

$$\dot{\sigma}_{ij}^1 = \hat{\sigma}_{ij}^{kl}(\mathbf{y}) \frac{\partial \dot{u}_k^0}{\partial x_l}, \quad \dot{u}_i^1 = \chi(\mathbf{y})_i^{kl} \frac{\partial \dot{u}_k^0}{\partial x_l}, \quad \frac{\partial \hat{\sigma}_{ij}^{kl}(\mathbf{y})}{\partial y_j} = 0 \quad (4.17)$$

In equation (4.17),  $\hat{\sigma}_{ij}^{kl}$  is a  $\mathbf{Y}$ -antiperiodic function and  $\chi_i^{kl}$  is a  $\mathbf{Y}$ -periodic function representing characteristic modes of the deformation rate in the RVE. Substituting equation (4.17) in the constitutive relations of equation (4.9) yields the microscopic constitutive relations as:

$$\hat{\sigma}_{ij}^{kl}(\mathbf{y}) = E_{ijpm}^\epsilon [\delta_{kp} \delta_{lm} + \frac{\partial \chi_p^{kl}}{\partial y_m}] \quad (4.18)$$

where  $\delta_{ij}$  is Kronecker delta. The mean of equation (4.18) yields the homogenized elastic-plastic tangent modulus for use in the macroscopic analysis, in the form

$$E_{ijkl}^{hom} = \langle \hat{\sigma}_{ij}^{kl} \rangle_Y = \frac{1}{|\mathbf{Y}|} \int_Y \hat{\sigma}_{ij}^{kl} dY = \frac{1}{|\mathbf{Y}|} \int_Y E_{ijpm}^\epsilon (\delta_{kp} \delta_{lm} + \frac{\partial \chi_p^{kl}}{\partial y_m}) dY \quad (4.19)$$



The macroscopic stress and strain relation can thus be stated as

$$\dot{\Sigma}_{ij}(\mathbf{x}) = \langle E_{ijkl}^e (\delta_{km} \delta_{ln} + \frac{\partial \chi_k^{mn}}{\partial y_l}) \frac{\partial u_m^0}{\partial x_n} \rangle_Y = E_{ijmn}^H \dot{e}_{kl}(\mathbf{x}) \quad (4.20)$$

where the homogenized variables are  $\Sigma(\mathbf{x}) = \langle \sigma^e(\mathbf{x}, \mathbf{y}) \rangle_Y$  and  $\mathbf{e}(\mathbf{x}) = \langle \epsilon^e(\mathbf{x}, \mathbf{y}) \rangle_Y$ . The incremental small deformation analysis for elastic-plastic materials can be conducted with the homogenized modulus at the macroscopic level and by using the Voronoi cell finite element model (VCFEM) for solving the microscopic problem.

#### 4.4.2 The Voronoi cell FEM for microstructural analysis

The Voronoi cell finite element model has been successfully developed for composite and porous materials in [22, 23, 25]. Arbitrary dispersion patterns, shapes and sizes of heterogeneities are readily modeled by VCFEM. The computational model naturally evolves by Dirichlet tessellation of the microstructure as shown in figure 4.1b. Each Voronoi cell with the embedded inclusion or void is treated as an element in this formulation. Preprocessing efforts are drastically reduced, as a consequence. In [23, 28], the VCFEM formulation has been extended to include damage evolution in the form of particle cracking, where the crack is realized as an elliptical void. Each Voronoi cell element is amenable to change in topology from two constituent phases (matrix and inclusions) in undamaged cells, to three phases (matrix, inclusion and crack) in damaged cells. Complete particle cracking or splitting is assumed to occur at the very onset of damage.

The Voronoi cell finite element formulation constructs a hybrid element by combining the aspects of finite element methods with important micromechanics considerations. Use of a hybrid stress based formulation results in a high level of accuracy with a significantly reduced degree of freedom, compared to displacement based FEM models. Consider a typical representative volume element  $\mathbf{Y}$  consisting of  $N$  undamaged and/or damaged particles, that are contained in each of the  $N$  Voronoi cell elements, as shown in figure 4.1(b). The assumed stress hybrid formulation in the Voronoi cell finite element method (VCFEM) requires independent assumptions of an equilibrated stress field ( $\sigma$ ) in the interior of each element  $Y_e$ , and compatible displacement fields  $\mathbf{u}$  on the element boundary  $\partial Y_e$ ,  $\mathbf{u}'$  on the matrix-inclusion interface  $\partial Y_c$  and  $\mathbf{u}''$  on the crack boundary  $\partial Y_{cr}$ . In an incremental formulation for elasto-plasticity, the incremental variational formulation introduces an element energy functional,

$$\begin{aligned} \Pi_e^C(\Delta\sigma, \Delta\mathbf{u}) = & - \int_{Y_e} \Delta B(\sigma, \Delta\sigma) dY - \int_{Y_e} \epsilon : \Delta\sigma dY + \\ & \int_{\partial Y_e} (\sigma + \Delta\sigma) \cdot \mathbf{n}^e \cdot (\mathbf{u} + \Delta\mathbf{u}) d\partial Y \quad (\text{Inter-element Traction Reciprocity}) \\ & - \int_{\Gamma_{tm}} (\bar{\mathbf{t}} + \Delta\bar{\mathbf{t}}) \cdot (\mathbf{u} + \Delta\mathbf{u}) d\Gamma \quad (\text{Boundary Traction}) \\ & - \int_{\partial Y_c} (\sigma^m + \Delta\sigma^m - \sigma^c - \Delta\sigma^c) \cdot \mathbf{n}^c \cdot (\mathbf{u}' + \Delta\mathbf{u}') \partial Y \quad (\text{Matrix-Inclusion Interface Traction}) \\ & - \int_{\partial Y_{cr}} (\sigma^c + \Delta\sigma^c) \cdot \mathbf{n}^{cr} \cdot (\mathbf{u}'' + \Delta\mathbf{u}'') \partial Y \quad (\text{Crack Boundary Traction}) \end{aligned} \quad (4.21)$$

where  $\Delta B$  is the increment of complimentary energy density. Variables  $(\sigma, \mathbf{u})$  correspond to values at the beginning of an increment, while variables  $(\Delta\sigma, \Delta\mathbf{u})$  are the corresponding increments in

a load increment or step. Outward normals on  $\partial Y_e$ ,  $\partial Y_c$  and  $\partial Y_{cr}$  are denoted by  $\mathbf{n}^e$ ,  $\mathbf{n}^c$  and  $\mathbf{n}^{cr}$  respectively. Superscripts  $m$ ,  $c$  and  $cr$  are associated with the matrix, inclusion and crack phases respectively in each Voronoi cell element. The total energy for the entire RVE of  $N$  Voronoi cells is obtained as  $\Pi^C = \sum_{e=1}^N \Pi_e^C$ . Setting the first variation of  $\Pi_e^C$  in equation (4.21) with respect to stress increments  $\Delta \sigma$  to zero yields the element compatibility as the Euler equation, while setting the first variations of  $\Pi^C$  with respect to the independent boundary displacements  $\Delta \mathbf{u}$ ,  $\Delta \mathbf{u}'$  and  $\Delta \mathbf{u}''$  to zero, yield the inter-element boundary traction reciprocity, matrix-inclusion interface traction reciprocity and zero traction crack boundary condition respectively. Independent assumptions on stress increments  $\Delta \sigma$  are made in the matrix and inclusion phases in each element, thus allowing stress discontinuities across the interface. In this process special forms of the Airy's stress function  $\Phi(x, y)$  to enhance computational efficiency, has been developed in [22, 23] for equilibrated stress fields. The functions facilitate stress concentration near the interface and crack boundary, accounting for the shape of the inclusion and crack and also help satisfy traction reciprocity at the interfaces  $\partial Y_c$  and  $\partial Y_{cr}$ . Furthermore, they decay at large distances from the interfaces. Compatible displacement increments are generated on each of the boundaries/interfaces  $\partial Y_e$ ,  $\partial Y_c$  and  $\partial Y_{cr}$  by interpolation in terms of generalized nodal displacements as ,

$$\{\Delta \mathbf{u}\} = [\mathbf{L}^e]\{\Delta \mathbf{q}\} \quad , \quad \{\Delta \mathbf{u}'\} = [\mathbf{L}^c]\{\Delta \mathbf{q}'\} \quad , \quad \{\Delta \mathbf{u}''\} = [\mathbf{L}^{cr}]\{\Delta \mathbf{q}''\} \quad (4.22)$$

where  $\{\Delta \mathbf{q}\}$ ,  $\{\Delta \mathbf{q}'\}$  and  $\{\Delta \mathbf{q}''\}$  are the nodal displacement increment vectors, and  $[\mathbf{L}^e]$ ,  $[\mathbf{L}^c]$  and  $[\mathbf{L}^{cr}]$  are the corresponding interpolation matrices. Details of the solution process are provided in [22, 23].

#### 4.4.3 Coupling asymptotic homogenization with VCFEM

The incremental energy functional for each Voronoi cell element in equation (4.21) is modified for the asymptotic homogenization process as:

$$\begin{aligned} \Pi_e^C = & - \int_{Y_e} \frac{1}{2} S_{ijkl}^e \Delta \sigma_{ij}^e \Delta \sigma_{kl}^e dY - \int_{Y_e} \epsilon^e : \Delta \sigma^e dY + \\ & \int_{\partial Y_e} (\sigma^e + \Delta \sigma)^e \cdot \mathbf{n}^e \cdot (\mathbf{u}^1 + \Delta \mathbf{u}^1) d\partial Y - \int_{\partial Y_c} (\sigma^{em} + \Delta \sigma^{em} - \sigma^{ec} - \Delta \sigma^{ec}) \cdot \mathbf{n}^c \cdot (\mathbf{u}^{1'} + \Delta \mathbf{u}^{1'}) d\partial Y \\ & - \int_{\partial Y_{cr}} (\sigma^{ec} + \Delta \sigma^{ec}) \cdot \mathbf{n}^{cr} \cdot (\mathbf{u}^{1''} + \Delta \mathbf{u}^{1''}) d\partial Y + \int_{Y_e} (\mathbf{e} + \Delta \mathbf{e}) \Delta \sigma^e dY \end{aligned} \quad (4.23)$$

where  $S_{ijkl}^e$  is an instantaneous elastic-plastic compliance tensor. The last term in equation (4.23) incorporates the effect of macroscopic strains  $\mathbf{e}$  in the microstructure. The stationary condition of  $\Pi_e^C$  with respect to stress increment  $\Delta \sigma_{ij}^e$  yields as Euler's equations, the incremental form of kinematic relations

$$e_{ij}^e + \Delta e_{ij}^e = e_{ij} + \Delta e_{ij} + \frac{\partial(u_i^1 + \Delta u_i^1)}{\partial y_j} \quad (4.24)$$

where  $\Delta u_i^1$  is the microscopic displacement in equation (4.17). Stationarity of the total energy functional  $\Pi = \sum_{e=1}^N \Pi_e^C$  with respect to displacement increments  $\Delta u_i^1$ ,  $\Delta u_i^{1'}$  and  $\Delta u_i^{1''}$ , result in the inter-element, interface and crack boundary traction reciprocity conditions respectively. The Voronoi cell finite element module is incorporated in a macroscopic analysis module with the interface being created by the homogenization procedure in [26, 27]. A displacement based finite

element code with plane strain QUAD4 elements with one-point reduced integration and hourglass control is used for macroscopic analysis. Material constitutive relations at each integration point of elements are obtained from homogenization of microscopic VCFEM results. Microscopic stresses  $\sigma_{ij}^e$  are averaged to yield macroscopic stresses  $\Sigma_{ij}$ . The microscopic VCFEM is also invoked to evaluate the homogenized elastic-plastic tangent modulus  $E^H$  by applying unit components of macroscopic strain.

## 4.5 Computational Subdomain Level-0 in the Hierarchical Model

Level-0 corresponds to macroscopic regions ( $\Omega_{l0} \subset \Omega_{MAT(p)}$ ) in figure 4.2a, where deformation variables like stresses and strains are relatively uniform in their macroscopic behavior. Scale effects are negligible and local constitutive relations may be derived from postulates of zero RVE volume in the limit and periodicity. It is assumed that macroscopic analyses with homogenized constitutive relations are sufficient for these regions. Anisotropic constitutive relations with varying parameters are developed for continuum analysis of heterogeneous microstructures with elastic-plastic constituent phases. To account for details of microstructural morphology, the constitutive model is based on two scale analysis using the asymptotic homogenization method and microstructural analysis by VCFEM. A continuum constitutive model can greatly enhance computational efficiency over two-scale analysis.

### 4.5.1 An elastic-plastic constitutive model

Various continuum constitutive models have been proposed, based on unit cell analyses of composite and porous microstructures. One parameter plastic potential functions with assumptions of anisotropy have been introduced in [32, 33] for composite materials, where the parameter is determined by least squares fitting of unit cell characteristic responses. Bao et. al. [34] have used the same hardening exponent for the composite as for the matrix material. A widely used continuum constitutive model for porous materials is that of Gurson [35], which has been modified by Tvergaard [36] with unit cell analysis to incorporate the effects of void growth and coalescence. Besides the limitations in representing actual microstructural heterogeneities, a number of these constitutive models do not adequately accommodate variations in constitutive parameters with evolving deformation and do not account for post-yield anisotropy. Terada and Kikuchi [37] have tried to overcome this by using the asymptotic homogenization to develop an extensive numerical response database in the strain space. Instantaneous overall composite properties are determined from discrete values of homogenized stress-strain values at points of this database. This approach, however leads to huge database to cover all possible deformation paths and requires solving an inordinately large number of RVE boundary value problems. Fish et. al. [10] have used the idea of transformation strain fields, introduced by Dvorak et.al [38], to develop a two point averaging scheme based on the mathematical homogenization theory with piecewise constant transformation fields. However, approximating the eigenstrains with low order polynomial functions may not be able to fully account for large gradients in stresses and strains between phases.

Motivated by two considerations, a piecewise continuous elastic-plastic constitutive model with an anisotropic yield function is developed. The first is an accuracy consideration, in that it should

account for the microstructural morphology, e.g. spatial distributions, shapes, sizes and properties of the individual phases, phase interactions, as well as the evolving stress and strain fields. This can be achieved if the model is developed from detailed finite element analyses of the RVE (e.g. VCFEM analysis), subjected to a wide variety of loading conditions. The second is an efficiency consideration, since the creation of a prohibitively large numerical database with a very large number of numerical experiments is of no consequence. The efficient development of a constitutive model, accounting for underlying evolution of state variables, is accomplished by generating piecewise continuous model parameters from data in a discretized strain space (see figure 4.4). Numerical data points in the strain space are systematically created through a sequence of computational RVE analyses subject to an ordered set of macroscopic strains and strain paths. The strain space in figure 4.4 is discretized into cubic elements, each containing 32 nodes or data points. From the computational RVE analysis, constitutive parameters like yield function coefficients and plastic work are generated for each nodal point. The constitutive relation at any point in the strain space are then obtained by interpolating nodal values using conventional shape functions. Elastic-plastic models developed in the ensuing sections are for plane strain assumptions.

## Linear Elasticity

Orthotropic homogenized elastic material properties are obtained by asymptotic homogenization in conjunction with the VCFE analysis of the composite and porous microstructures from equation (4.19) as explained in [27]. With plane strain assumptions, three separate VCFE analyses are conducted, each corresponding to an independent component of the macroscopic strain  $\{e_{xx}, e_{yy}, e_{xy}\}$ . The orthotropic elasticity tensor is stored for macroscopic analysis.

### 4.5.2 Elasto-plasticity with anisotropic yield function

The inclusion phase in composites are assumed to be linear elastic, while the matrix phase is assumed elastic-plastic for both composite and porous materials. In plane strain modeling, an assumption that the total plastic strain in the out of plane or 'third' direction is zero, is made. The yield function can then be described in terms of the macroscopic in-plane stress components  $(\Sigma_{xx}, \Sigma_{yy}$  and  $\Sigma_{xy})$ . The yield function for porous and composite are written using Hill's 1948 anisotropic yield function [39, 33] in conjunction with the hydrostatic stress dependent models of the Tvergaard-Gurson [35, 36] as :

$$\Phi = \frac{C(\Sigma_{xx} - \Sigma_{yy})^2 + 3 \Sigma_{xy}^2}{Y_f^2(W_p)} + H \cosh \left( \frac{\sqrt{3}(\Sigma_{xx} + \Sigma_{yy})}{2 Y_f(W_p)} \right) - 1 = 0 \quad (4.25)$$

where  $e_{xx}, e_{yy}, e_{xy}$  are the macroscopic in-plane strains,  $C(e_{xx}, e_{yy}, e_{xy}, W_p)$  is a strain dependent yield surface parameter and  $Y_f(W_p)$  is the flow stress in shear. For the composite materials the dependence of pressure on yielding is deemed negligible and the hydrostatic stress coefficient  $H$  is ignored. Coefficients  $C(e_{xx}, e_{yy}, e_{xy}, W_p)$ ,  $Y_f(W_p)$  and  $H$  are determined from computational experiments detailed next. The increment of plastic strain is obtained from the yield function  $\Phi$  by using the associated flow rule for hardening materials, i.e.  $\dot{e}_{ij}^p = \dot{\lambda} \frac{\partial \Phi}{\partial \Sigma_{ij}}$ .

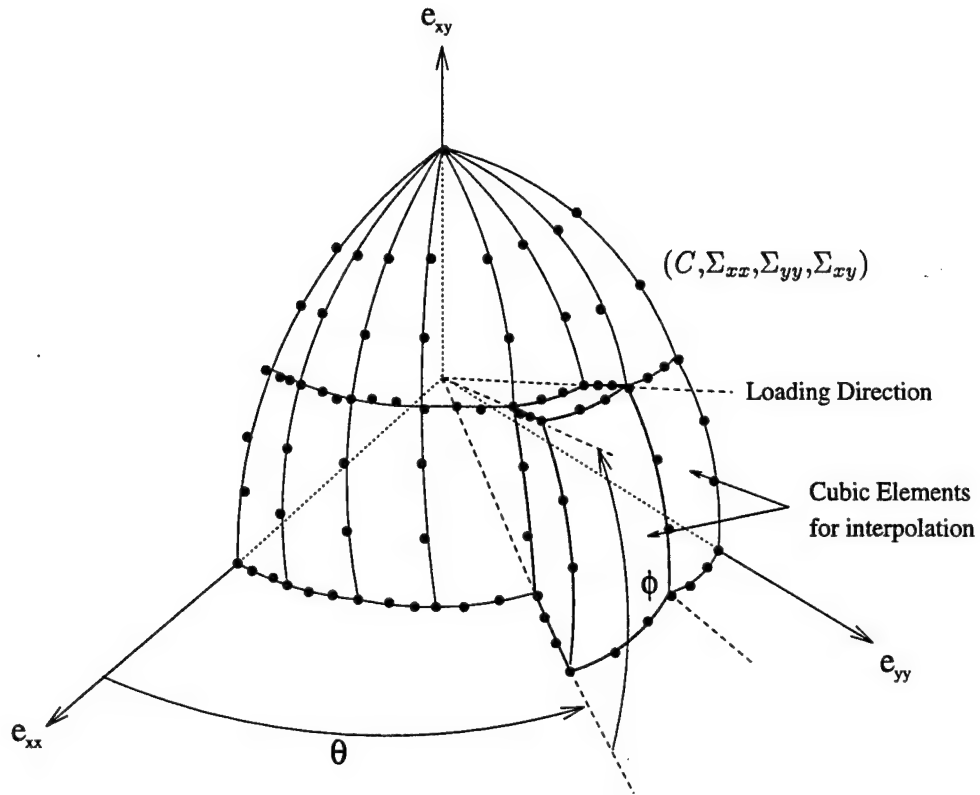


Figure 4.4: A  $e_{xx} - e_{yy} - e_{xy}$  strain sub-space, discretized into cubic elements for interpolating constitutive model parameters. The nodal values of stresses and plastic work are numerically generated.

## Coefficient Evaluation

### A. $H$ and $Y_f(W_p)$

Computational exercises indicate that the variation of  $H$  with increasing hydrostatic loading is not significant. It is therefore assumed to be a constant for all load histories. This assumption is consistent with the Tvergaard-Gurson models [35, 36], where  $H$  is determined in terms of the initial void volume fraction. The constitutive parameters  $H$  and  $Y_f(W_p)$  are evaluated in a coupled manner by solving the microstructural RVE boundary value problems with two distinct loading conditions viz. (i) biaxial tension loading ( $\Sigma_{xx} = \Sigma_{yy} = \Sigma_{hyd}$ ,  $\Sigma_{xy} = 0$ ) and (ii) pure shear loading ( $\Sigma_{xy} = \Sigma_{sh}$ ,  $\Sigma_{xx} = \Sigma_{yy} = 0$ ). For load condition (i), equation (4.25) becomes:

$$\Phi(\Sigma_{hyd}, \Sigma_{hyd}, 0, W_p) = H \cosh \left( \sqrt{3} \frac{\Sigma_{hyd}}{Y_f(W_p)} \right) - 1 = 0 \quad (4.26)$$

and for load condition (ii), it becomes:

$$\Phi(0, 0, \Sigma_{sh}, W_p) = \frac{3 \Sigma_{sh}^2}{Y_f^2(W_p)} + H - 1 = 0 \quad \text{or} \quad Y_f(W_p) = \sqrt{\frac{3 \Sigma_{sh}^2}{1 - H}} \quad (4.27)$$

The values of  $H$  and  $Y_f(W_p)$  are determined iteratively from equation (4.27) and further validated against equation (4.26). The steps are as follows.

1. Solve a macro-micro boundary value problem with RVE homogenization, with incremental pure shear loading. Obtain macroscopic plastic work by averaging the the microstructural plastic work ( $\dot{W}_p = \frac{1}{V_{RVE}} \int_{\Omega} \sigma_{ij} \dot{\epsilon}_{ij}^p d\Omega$ ) and plot the macroscopic shear stress as a function of plastic work  $W_p$ .
2. Assume a starting value for  $H$  (e.g.  $3\star f_0$  as in [35, 36]) and evaluate  $Y_f(W_p)$  from equation (4.27).
3. Solve a pure macroscopic boundary value problem with incremental biaxial loading, using the homogenized elastic-plastic constitutive relation and associated flow rule with yield function (4.25).
4. Plot the  $e_{xx} - \Sigma_{hyd}$  and  $e_{yy} - \Sigma_{hyd}$  curves for the entire history of biaxial loading.
5. Solve a macro-micro boundary value problem with RVE homogenization with the same incremental biaxial loading as in the previous step. Plot the  $\Sigma_{hyd} - e_{xx}$  and  $\Sigma_{hyd} - e_{yy}$  curves for the entire history of loading.
6. Compare the results of steps 4 and 5. If the two curves from both methods are within a preset tolerance everywhere, then the process is terminated and value of  $H$  in step 2 is accepted. Otherwise, the entire sequence is repeated with a different value of  $H$ .

### B. $C(e_{ij}, W_p)$

The coefficient  $C$  in equation (4.25) is found to vary considerably with evolution of plastic deformation and examples of its variation with straining and plastic work are shown in figures 4.5.

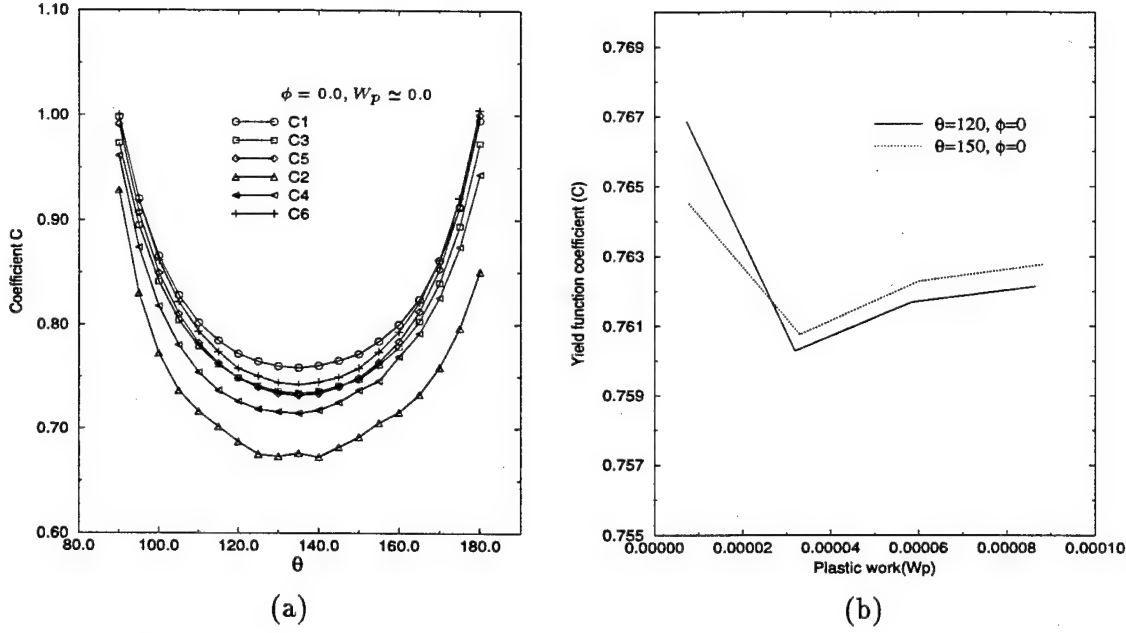


Figure 4.5: Variation of the yield function coefficient  $C(e_{xx}, e_{yy}, e_{xy}, W_p)$ , (a) as a function of  $\theta$  or normal strains for different microstructures, (b) as a function of plastic work  $W_p$ .

While it is assumed to be a function of the total strain and plastic work, its dependence on load history is assumed to be negligible. In the discretized strain space of figure 4.4, the value of a piecewise continuous  $C$  at any point may then be obtained by interpolation from nodal values according to

$$C(e_{xx}, e_{yy}, e_{xy}, W_p) = \sum_{\alpha=1}^{32} C_{\alpha}(W_p) N_{\alpha}(e_{xx}, e_{yy}, e_{xy}) \quad (4.28)$$

where  $C_{\alpha}$  are the nodal values and  $N_{\alpha}$  are shape functions for a 32-noded brick element.

#### Generation of Discretized Strain Space and Nodal Parameters

The nodal values of macroscopic stresses ( $\Sigma_{xx}, \Sigma_{yy}, \Sigma_{xy}$ ) and the corresponding plastic work  $W_p$  are first evaluated at each nodal point in a subspace of the  $e_{xx} - e_{yy} - e_{xy}$  space by solving incremental macro-microscopic boundary value problems with VCFEM and asymptotic homogenization. In this process, macroscopic strain increments are applied to the RVE subjected to periodic boundary conditions [26, 27]. Strain increments are applied along a radial line in the strain space, such that a constant ratio between strain components is maintained, i.e.  $\Delta e_{xx} : \Delta e_{yy} : \Delta e_{xy} = 1 : \tan \theta : (1 + \tan^2 \theta) \tan \phi$ , where  $\theta$  and  $\phi$  are the angular coordinates in the strain space of figure 4.4. The flow stress  $Y_f(W_p)$  at each node in figure 4.4 can be obtained from the shear stress-plastic work plot and equation (4.27). From the values of macroscopic variables ( $\Sigma_{xx}, \Sigma_{yy}, \Sigma_{xy}, Y_f(W_p)$ ) at a node corresponding to the end of an increment, the coefficient  $C(e_{xx}, e_{yy}, e_{xy}, W_p)$  is calculated using equation (4.25).

From the symmetry conditions, only a quarter of the  $e_{xx} - e_{yy} - e_{xy}$  strain space is considered for loading such that  $0^\circ \leq \theta \leq 180^\circ$  in the  $e_{xx} - e_{yy}$  plane and  $0^\circ \leq \phi \leq 90^\circ$  outside of this plane. This is indicated in figure 4.4. This chosen subspace of the strain space is divided into 16 cubic brick element with 32 nodal points each. The location of elements in the strain space are selected to optimally account for the variations in  $C$ . These variations in  $C$  with the coordinate angle  $\theta$  (location in the  $e_{xx} - e_{yy}$  plane) and the plastic work  $W_p$  for the different microstructures are plotted in figure 4.5. The parabolic form of  $C$  in figure 4.5a is consistent with the quadratic term  $(\Sigma_{xx} - \Sigma_{yy})^2$  in the yield function. The minimum values occur near  $\theta = 135^\circ$  corresponding to a pure deviatoric state. The coefficient subsequently increases to account for the increase in plastic work in the yield function  $\Phi$ . In figure 4.5b, the coefficient  $C$  as a function of the plastic work, which corresponds to the radial direction in the strain space, is plotted. The value of  $C$  stabilizes beyond a value of the plastic work, which is used as the outer boundary of the strain space envelope in figure 4.4.

### 4.5.3 Numerical implementation of the constitutive model

The elastic-plastic constitutive model for composite and porous materials is derived from the anisotropic yield function (4.25) with associated flow rule and isotropic hardening. In an incremental form, the stress increments  $\Delta\Sigma_{ij}$  are related to elastic increments of strains  $(\Delta e_{kl} - \Delta e_{kl}^p)$  admitting additive decomposition, as

$$\Delta\Sigma_{ij} = E_{ijkl}^H (\Delta e_{kl} - \Delta e_{kl}^p) \quad (4.29)$$

where  $E_{ijkl}^H$  is the homogenized elasticity tensor. Using associated flow rule, components of the plastic strain increment are obtained as:

$$\Delta e_{ij}^p = \Delta\lambda \frac{\partial\Phi}{\partial\Sigma_{ij}} \quad (4.30)$$

Elimination of the flow parameter  $\Delta\lambda$  from the above equations results in the two equations

$$\Delta e_{xx}^p \left( \frac{\partial\Phi}{\partial\Sigma_{yy}} \right) - \Delta e_{yy}^p \left( \frac{\partial\Phi}{\partial\Sigma_{xx}} \right) = 0 \quad , \quad \Delta e_{xx}^p \left( \frac{\partial\Phi}{\partial\Sigma_{xy}} \right) - \Delta e_{xy}^p \left( \frac{\partial\Phi}{\partial\Sigma_{xx}} \right) = 0 \quad (4.31)$$

These equations are solved using the backward Euler integration method, with gradients evaluated at the end of the increment. With known increments of strain, the resulting set of equations (4.31) together with the yield function (4.25) are solved iteratively by using the Newton-Raphson method. The stress increments are obtained by the following steps.

1. Initialize values of  $\Delta\Sigma_{xx}$ ,  $\Delta\Sigma_{yy}$  and  $\Delta\Sigma_{xy}$ .
2. Calculate the gradient  $\left( \frac{\partial\Phi}{\partial\Sigma_{ij}} \right)$  of the yield function and solve for the increments of plastic strain  $\Delta e_{xx}^p$ ,  $\Delta e_{yy}^p$  and  $\Delta e_{xy}^p$  from equations (4.29) and (4.31). Update the stresses and plastic work using the relation  $\Delta W_p = \Sigma_{xx}\Delta e_{xx}^p + \Sigma_{yy}\Delta e_{yy}^p + \Sigma_{xy}\Delta e_{xy}^p$ .
3. If  $\Phi \leq tol_1$  and correction to plastic strain increment  $\delta e_{ij}^p \leq tol_2$ , where  $tol_1$  and  $tol_2$  are prescribed tolerances, then stop. Otherwise go to step 2.

The parameter  $C$  is then obtained from the interpolation equation (4.28).



#### 4.5.4 Numerical examples with the continuum constitutive model

The elastic-plastic constitutive model is validated by comparing the results of macroscopic numerical simulations with those generated by macro-micro scale analysis using asymptotic homogenization. Examples are conducted for both composite and porous materials with different microstructure morphologies, viz. different shapes, sizes and spatial distributions of the heterogeneities.

##### Analysis of Composite Microstructures

Six microstructural RVE's of 20%  $V_f$  Alumina-aluminum composite with Alumina fiber in aluminum matrix, as shown in figure 4.6, are analyzed. The RVEs are classified as:

- (a): Square edge pattern with a circular inclusion (C1)
- (b): Square edge pattern with an elliptical inclusion (aspect ratio  $\frac{a}{b} = 3$ ) (C2)
- (c): Random pattern with 25 identical circular inclusions (C3)
- (d): Horizontally aligned random pattern with 25 identical elliptical inclusions (C4)
- (e): Randomly oriented random pattern with 25 identical elliptical inclusions (C5)
- (f): Random pattern with 17 random shape and size inclusions (C6)

The material properties for the elastic Alumina fiber are:

Young's Modulus ( $E_c$ )= 344.5GPa, Poisson Ratio ( $\nu_c$ )= 0.26;

and for the elastic-plastic Aluminum matrix are:

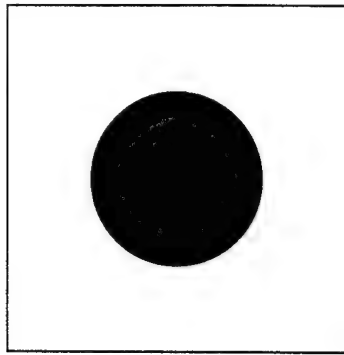
Young's Modulus ( $E_m$ )= 68.3 GPa, Poisson Ratio ( $\nu_m$ )=0.30, Initial Yield Stress ( $Y_0$ ): 55 MPa, and Post Yield hardening law:  $\sigma_{eqv} = Y_0 + 2.08\epsilon_{eqv}^{pl}$ .

The RVEs are subjected to four different types of loading viz.

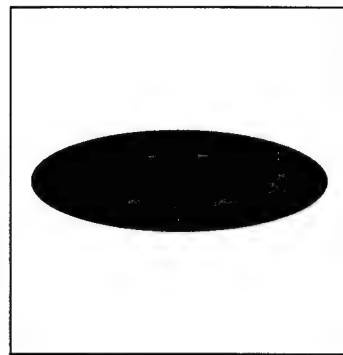
- L1: Pure shear loading with increments ( $\Delta\Sigma_{xx} = \Delta\Sigma_{yy} = 0, \Delta\Sigma_{xy} = \Delta\Sigma$ )
- L2: Uniaxial tension loading with increments ( $\Delta\Sigma_{xx} = \Delta\Sigma, \Delta\Sigma_{yy} = \Delta\Sigma_{xy} = 0$ )
- L3: Biaxial tension loading with increments ( $\Delta\Sigma_{xx} = \Delta\Sigma_{yy} = \Delta\Sigma, \Delta\Sigma_{xy} = 0$ )
- L4: Biaxial tension-compression loading with increments ( $\Delta\Sigma_{xx} = -\Delta\Sigma_{yy} = \Delta\Sigma, \Delta\Sigma_{xy} = 0$ )

The stress-strain response of the six composite microstructural RVEs with the four loading conditions are conducted and the results for simple tension (L1) are depicted in figure 4.7. The results by the constitutive model and two-scale asymptotic homogenization approach are generally found to agree very well for the entire range of loading upto fairly high level of straining. The only discrepancy is found with the biaxial tension loading condition (L3), for which the deviation strains are shown in table 1. However the deviations occurs at high strains levels, for which the stresses are nearly twice the matrix yield stress. It is important to note that the deviation of continuum model response from the two-scale asymptotic homogenization response can be used as a signal for switching from the former to the latter type of analysis in a multiple scale simulation.

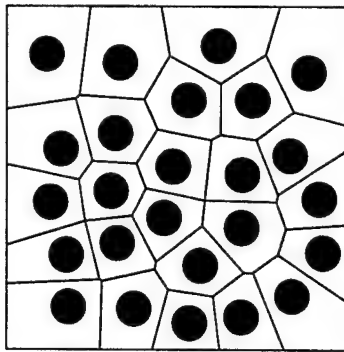
As an example of a structural analysis with the two approaches, a square plate with a square hole is solved with tension loading on two opposite faces. A quarter of the plate with symmetry and loading conditions is shown in figure 4.8a. A total traction of 55 MPa is applied in 10 equal increments. The material is a 20 %  $V_f$  Alumina-aluminum composite with the microstructural RVE consisting of 15 identical circular inclusions dispersed randomly in the matrix (figure 4.8b). The material properties are the same as in the previous example. Comparison of the results are



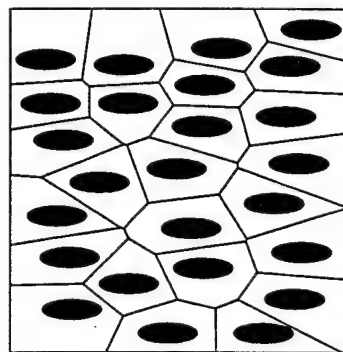
(C1,V1)



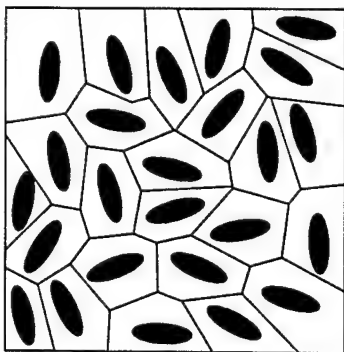
(C2,V2)



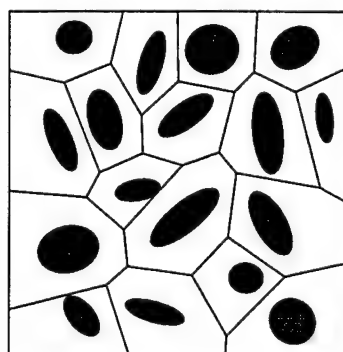
(C3,V3)



(C4,V4)

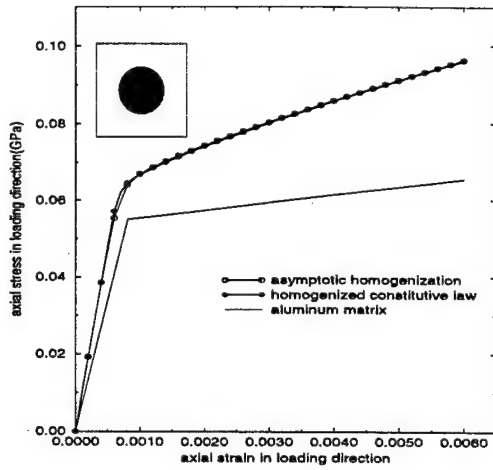


(C5,V5)

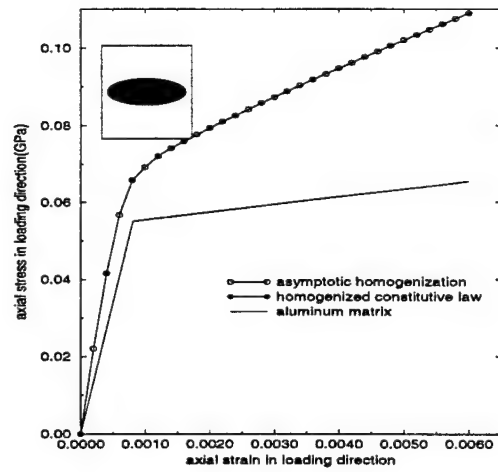


(C6,V6)

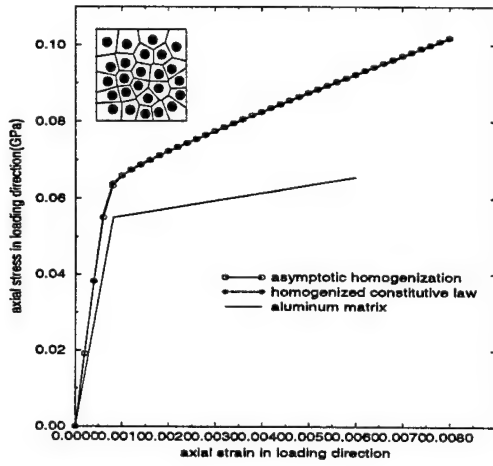
Figure 4.6: Microstructures with different shape, size, orientation and spatial distribution, for 20% volume fraction composite (C1,C2,C3,C4,C5,C6) and porous (V1,V2,V3,V4,V5,V6) materials.



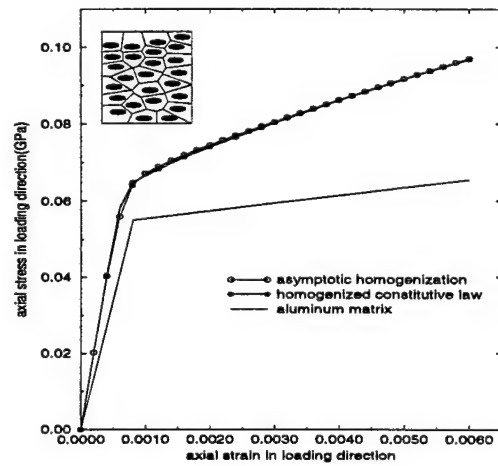
(a)



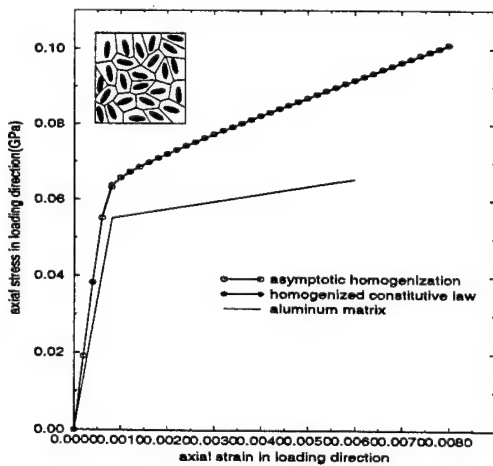
(b)



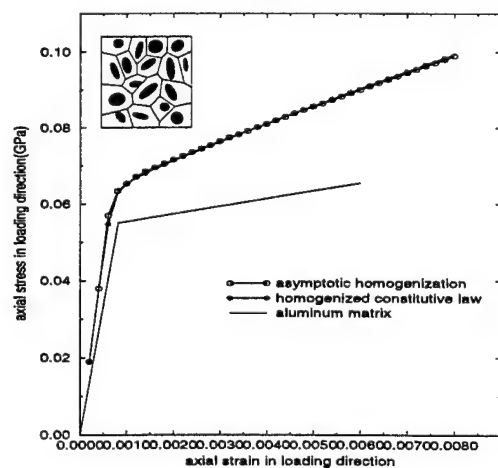
(c)



(d)



(e)



(f)

Figure 4.7: Comparison of the stress-strain results in the composite for the uniaxial loading test by (i) macroscopic analysis with the homogenized constitutive model and (ii) two-scale analysis with asymptotic homogenization model for: (a) C1, (b) C2, (c) C3, (d) C4, (e) C5 and (f) C6 microstructures.

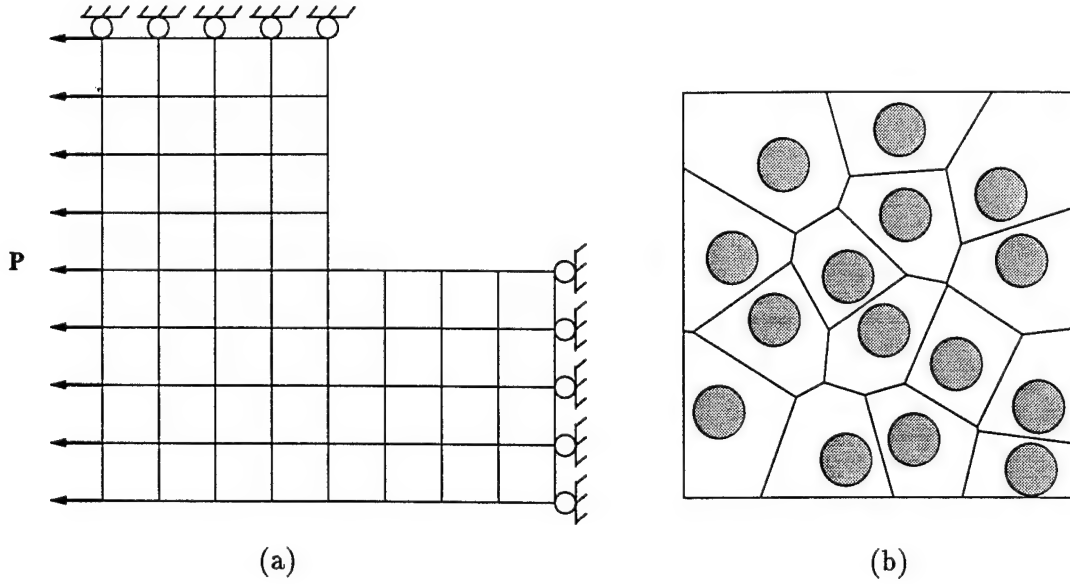


Figure 4.8: (a) Finite element model for a quarter of the square composite plate with square hole and (b) the VCFE model of the microstructural composite RVE.

made through contour plots of the macroscopic stress  $\Sigma_{xx}$  (shown in figure 4.9) and macroscopic plastic work  $W_p$  (not shown). The figures reveal that at all locations the difference in the two approaches is less than 1%. However, the computational efficiency of the macroscopic analysis with the continuum constitutive model is far superior than the two scale analysis. The scale up in efficiency for this problem is approximately 75000%, and is therefore very desirable when only macroscopic results are of interest.

### Analysis of Porous Microstructures

The six microstructural RVEs are analyzed again for porous materials, with voids replacing the inclusions in figure 4.6. The material considered is an aluminum alloy with 20% void volume fraction and the following elastic-plastic properties:

Young's Modulus ( $E_m$ ) = 68.3 GPa, Poisson Ratio ( $\nu_m$ ) = 0.30, Initial Yield Stress ( $Y_0$ ) = 55 MPa, and Post Yield hardening law:  $\sigma_{eqv} = Y_0 + 2.08\epsilon_{eqv}^p$ . The same four load histories (L1,L2,L3,L4) are applied. An important difference between the composite and porous microstructures, is that in the latter plastic strain localization in small regions is a common occurrence depending on the void morphology and the nature of loading. Such nonhomogeneous distribution of plastic strains is a major source of discrepancies between responses by the two approaches and act as 'limiters' for the range of application of the continuum model. Microstructures with homogeneous and nonhomogeneous distributions of plastic strain are shown in figure 4.10. For the microstructure V1 (square edge pattern with a circular void) the strain distribution is quite uniform in pure shear loading, while for the microstructure V2 (square edge with an elliptical void) there is intense localization with narrow ligaments. Consequently the continuum model ceases to be effective.

As in the case with composites, the main challenge for the homogenized constitutive model is encountered during simulations with biaxial tension loading, i.e. ( $\Delta\Sigma_{xx} = \Delta\Sigma_{yy} = \Delta\Sigma_b$  and

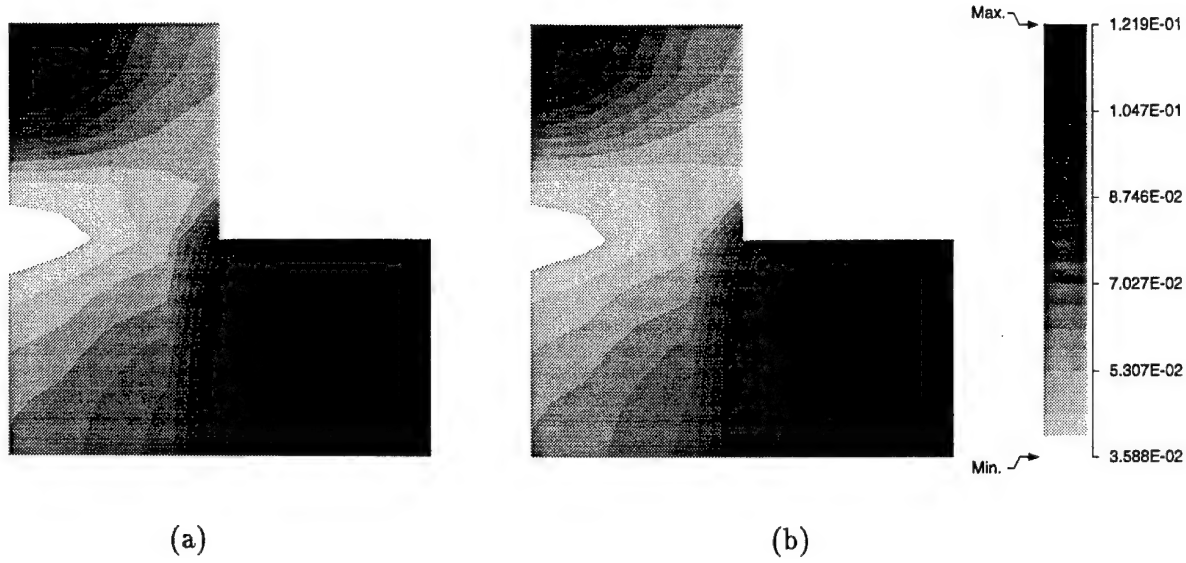
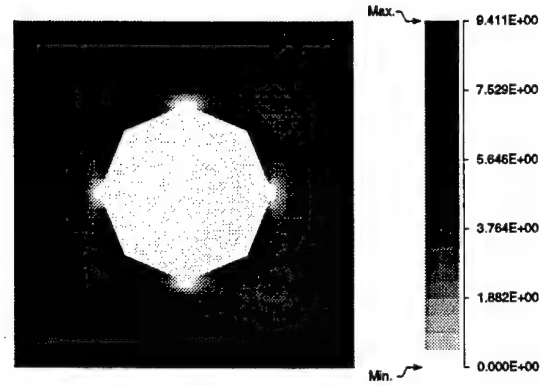


Figure 4.9: Comparison of macroscopic stress ( $\Sigma_{xx}$ ) contours in composite material with (a) the homogenized constitutive model and (b) two-scale analysis with asymptotic homogenization.

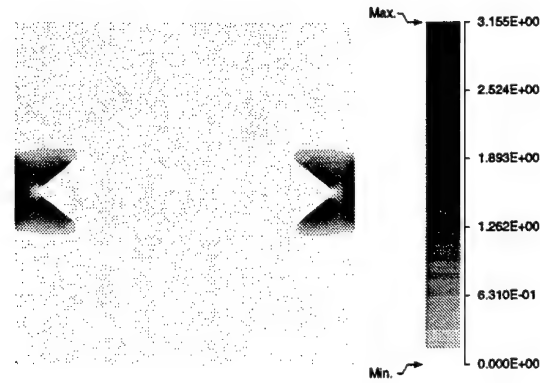
$\Delta\Sigma_{xy} = 0$ ). The first term in the yield function (4.25) drops out for this loading and the model delivers the same amounts of plastic strains in the  $x$  and  $y$  directions. Due to the lack of anisotropy in the hydrostatic term in the yield function, the continuum model is effective only for those microstructures that exhibit near-isotropic plastic behavior for this loading. Microstructures V2 (square edge with elliptical void) and V4 (horizontally aligned elliptical voids with random spatial distribution) shows very different strain responses for each direction with biaxial loading. Thus the continuum constitutive model is largely ineffective for these RVEs. The microstructures V5 (randomly oriented identical elliptical voids with random spatial distribution) and V6 (random spatial distribution with random shape and size) also show significant plastically induced directional effects and the constitutive models are therefore restricted to the elastic range. The list of performance and strain ranges of all the microstructures with the different loadings are given in table 2. The microstructures V1 and V3 exhibit relatively isotropic responses and yield satisfactory agreement between responses by the constitutive model and the two-scale asymptotic homogenization. Comparisons of stress-strain responses for biaxially and uniaxially loaded RVEs are made in figures 4.11. These show very good agreement. The RVEs V2 and V4 exhibit intense localization early on in the straining, while the RVEs V5 and V6 exhibit marked anisotropy with biaxial loading. Plastic flow predictions for these RVE's with the continuum model are therefore not reliable.

#### 4.6 Computational Subdomain Level-1 in the Hierarchical Model

The level-1 regions ( $\Omega_{l1} \subset \Omega_{MAT(p)}$ ) in the computational domain are identified by locally high gradients of macroscopic variables e.g. stresses, strains strain energy etc.. These are generally indicators of imminent damage evolution or localization in the microstructure. In these regions, the assumptions of macroscopic uniformity and statistical periodicity of the RVE are still assumed to

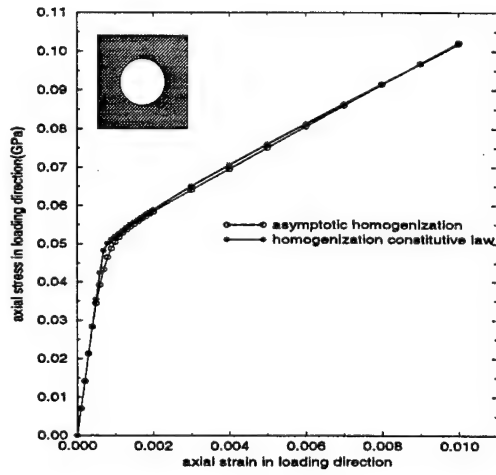


(a)

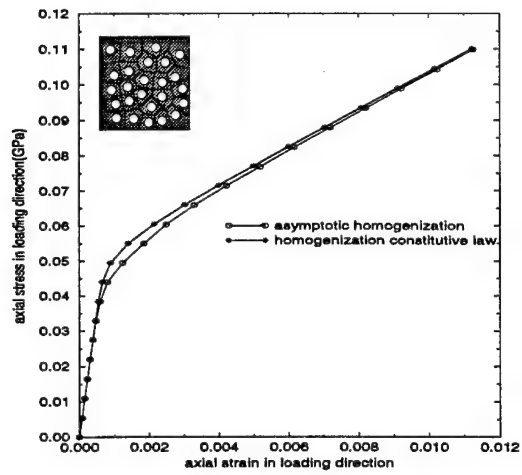


(b)

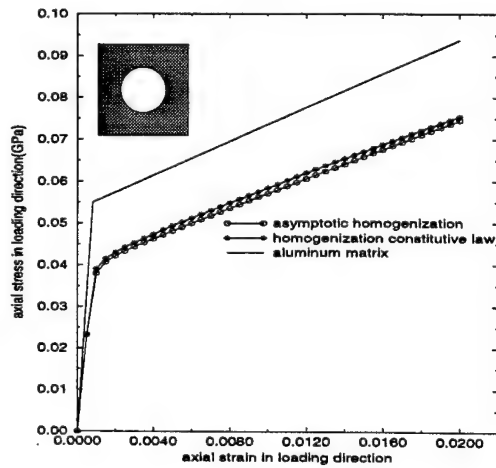
Figure 4.10: Contour plot of the microscopic plastic strain  $\bar{\epsilon}^p$  in the voided microstructures under pure shear loading condition, for (a) V1 (b) V2 microstructures.



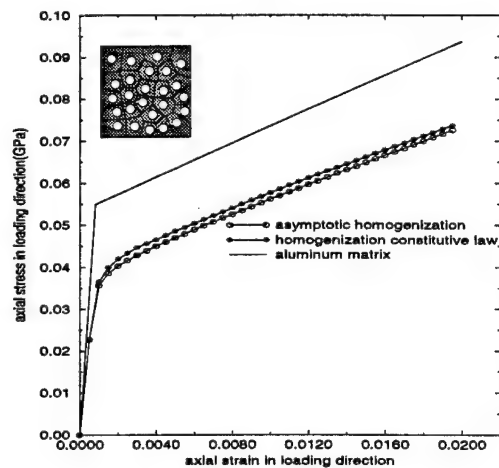
(a)



(b)



(c)



(d)

Figure 4.11: Comparison of the stress-strain results in the porous material for (a) bi-axial tension for V1 microstructure (b) bi-axial tension for V3 microstructure, (c) uniaxial tension for V1 microstructure and (d) uniaxial tension for V3 microstructure.

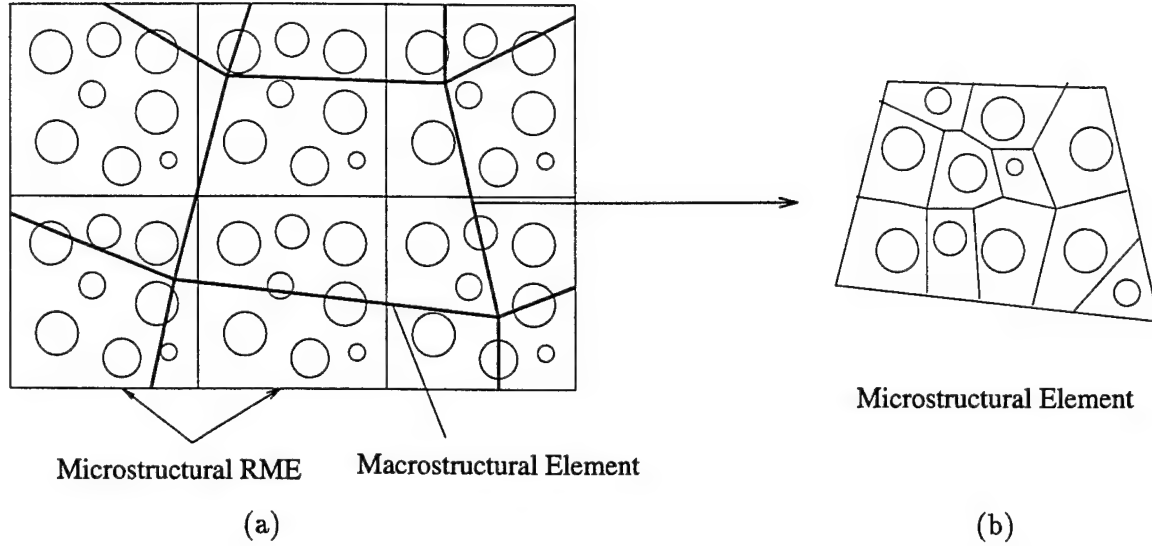


Figure 4.12: Creating extended microstructure; (a) a mesh of macroscopic elements with an underlying microstructure of repeated RVEs, (b) the extended microstructure by Voronoi tessellation.

hold. However, these assumptions may cease to hold soon, with additional deformation. Thus, in concurrence with macroscopic simulations, computations are necessary at the microstructural scale to monitor the initiation and growth of damage and instabilities. The RVE response for level-1 elements is explicitly calculated using asymptotic homogenization and VCFEM analysis. In its computational implementation, a sequence of finite element analyses are executed as follows:

- (a) Microstructural analysis by VCFEM with unit strains or increments and periodicity boundary conditions to generate homogenized material parameters ( $E_{ijkl}^H$ ),
  - (b) Macroscopic analysis of structural components with homogenized coefficients,
  - (c) Microstructural analysis by VCFEM with imposed macroscopic strains or increments and periodicity boundary conditions for simulating the evolution of microscopic stresses, strains ( $\sigma^e, \epsilon^e$ ) etc. .
- The computational requirements of this level are considerably higher than that for level 0, since at each integration point in the macroscopic computational mesh, a complete microstructural RVE problem has to be solved twice. It is also critical that this level be discontinued once the microstructural damage or instability evolved beyond pre-determined threshold values.

## 4.7 Computational Subdomain Level-2 in the Hierarchical Model

Level-2 regions (figure 4.2b) are classified as those with severe microstructural nonuniformities in the form of evolving damage. This results in loss of statistical periodicity of the assumed RVE and these regions may be identified with  $\Omega_{MAT(np)}$  in equation (4.5). In the computational model, the level-2 elements ( $\Omega_{l2} \subset \Omega_{MAT(np)}$ ) materialize from the microstructure of level-1 elements. It is assumed that prior to this transition, the level-1 elements have been refined to reach sufficiently high spatial resolution. In  $\Omega_{l2}$ , the macro-micro model of level-1 switches to a completely microscopic model.



The method of generating the level-2 microstructure in each element is illustrated in figure (4.12). An extended microstructure is first created by repeating RVEs in succession, to cover the entire region of the macroscopic level-1 elements in transition to level-2. In equation (4.7), a local non-periodic region is created as :

$$\mathbf{Y}_k^{MAT(np)} = \cup_{l=1}^{N^\infty} \mathbf{Y}_k^l \quad (4.32)$$

where  $\mathbf{Y}_k^l$  corresponds to the RVEs in a periodic domain, adjusted for microscopic evolution. This is then overlayed by the macroscopic elements to accurately encase the level-2 region with clearly delineated boundaries. Each level-2 element now contains a heterogeneous material distribution ( $\mathbf{Y}_k^e$ ) that is defined as the intersection of the non-periodic material region  $\mathbf{Y}_k^{MAT(np)}$  and the element domain  $\Omega_{l2}^e$

$$\mathbf{Y}_k^e = \mathbf{Y}_k^{MAT(np)} \cap \Omega_{l2}^e \quad (4.33)$$

This region is subsequently tessellated into a mesh of Voronoi cell elements (figure 4.12b). Traction continuity between level-2 microstructural region and neighboring level-0/level-1 elements is incorporated through a layer of transition elements.

#### 4.7.1 Damage criterion for particle cracking in level-2

The level-2 VCFEM modeling consist of brittle reinforcing particles and a ductile matrix material. For the brittle particulate materials, microstructural damage initiation is assumed to be governed by a maximum principal stress based criterion. In this criterion, a crack is initiated when the maximum principal stress in tension exceeds a critical fracture stress  $\sigma^{cr}$  at a point. In the computational procedure, complete particle splitting is assumed to occur in the form of an elliptical void, normal to the principal direction, as soon as the principal tensile stress reaches  $\sigma^{cr}$ . In the case of particle splitting, the crack tip extends nominally into the matrix. In the incremental computational procedure, more than one point may exceed the critical  $\sigma^{cr}$  value during increment. The location of a single crack is determined by a weighted averaging method as:

$$x_{damage} = \frac{\sum x \frac{\sigma_I^c(x,y)}{\sigma^{cr}}}{\sum \frac{\sigma_I^c(x,y)}{\sigma^{cr}}} \quad , \quad y_{damage} = \frac{\sum y \frac{\sigma_I^c(x,y)}{\sigma^{cr}}}{\sum \frac{\sigma_I^c(x,y)}{\sigma^{cr}}} \quad \forall \quad [\sigma_I^c(x,y) \geq \sigma^{cr}] \quad (4.34)$$

where  $\sigma_I^c(x,y)$  corresponds to all values of maximum tensile principal stress larger than  $\sigma^{cr}$  in the particle. The crack is oriented at right angles to the principal stress directions at  $(x_{damage}, y_{damage})$  and extends to the interface on both sides.

### 4.8 Coupling the Levels in the Hierarchical FEM

While level-0 elements ( $E_{l0} \in \Omega_{l0}$ ) and level-1 elements ( $E_{l1} \in \Omega_{l1}$ ) are coupled naturally through the familiar assembly process, the interfacing of level-2 ( $E_{l2} \in \Omega_{l2}$ ) elements with either of the first two requires more attention. The mismatch in the number of boundary nodes in these elements necessitate the introduction of transition elements ( $E_{tr} \in \Omega_{l2}$ ), acting as buffer zones as shown in figure 4.13. Both  $E_{l2}$  and  $E_{tr}$  elements employ VCFEM for setting up the element stiffness matrices and load vectors. The entire computational domain is thus comprised of

$$\Omega^e = \{\Omega_{l0} \cup \Omega_{l1} \cup \Omega_{l2} : \Omega_{l0} = \cup_{k=1}^{N_{l0}} E_{l0}; \Omega_{l1} = \cup_{k=1}^{N_{l1}} E_{l1}; \Omega_{l2} = \cup_{k=1}^{N_{l2}} E_{l2} \cup \cup_{k=1}^{N_{tr}} E_{tr}\}$$

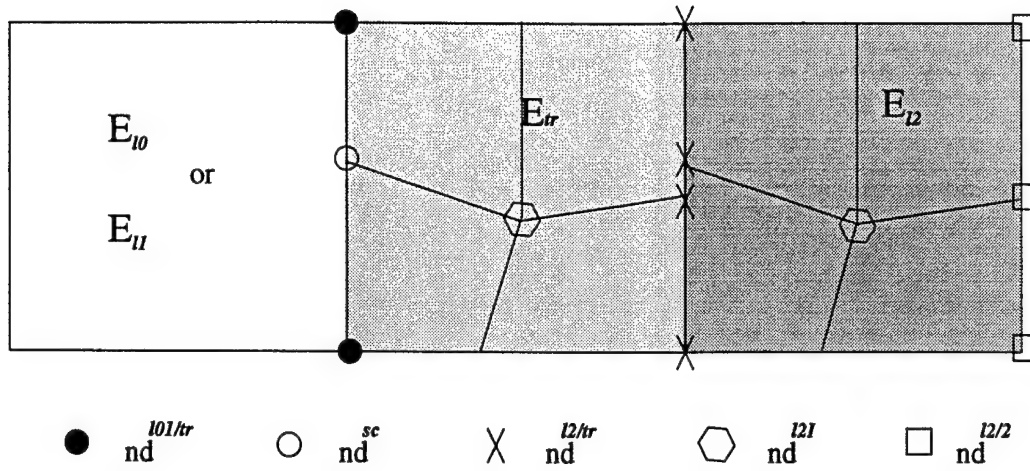


Figure 4.13: Interfaces between the level0/1  $E_{l0}$  and  $E_{l1}$  elements, transition  $E_{tr}$  elements and the level-2  $E_{l2}$  elements.

for which the nodes are differentiated as (see figure 4.13):

- (i)  $(\mathbf{nd}^{l2l})$  or internal level-2 Voronoi cell element nodes that are not on any interface or boundary,
- (ii)  $(\mathbf{nd}^{l2/2})$  or Voronoi cell element nodes on the  $E_{l2}$ - $E_{l2}$  interface,
- (iii)  $(\mathbf{nd}^{l2/tr})$  or Voronoi cell element nodes on  $E_{l2}$ - $E_{tr}$  interface,
- (iv)  $(\mathbf{nd}^{l0l/tr})$  or nodes on  $E_{l0/1}$ - $E_{tr}$  interface that belong to  $E_{l0}$  and  $E_{l1}$  elements,
- (v)  $(\mathbf{nd}^{sc})$  or Voronoi cell element nodes on  $E_{l0/1}$ - $E_{tr}$  interface that do not belong to  $E_{l0}$  and  $E_{l1}$  and need to be statically condensed. In an incremental analysis for elasto-plasticity, the principle of virtual work for the computational domain at the end of the  $n$  -  $th$  increment may be written as a scalar valued function  $G$  in terms of variables at different levels as:

$$\begin{aligned}
 G^{n+1}(\Delta \mathbf{u}, \delta \mathbf{u}) = & \int_{\Omega_{l0}^{n+1}} \Sigma_{ij}(\mathbf{u}^n + \Delta \mathbf{u}) \frac{\partial \delta u_i}{\partial x_j} d\Omega - \int_{\Omega_{l0}^{n+1}} f_i \delta u_i d\Omega \\
 & + \int_{\Omega_{l1}^{n+1}} \Sigma_{ij}(\mathbf{u}^n + \Delta \mathbf{u}) \frac{\partial \delta u_i}{\partial x_j} d\Omega - \int_{\Omega_{l1}^{n+1}} f_i \delta u_i d\Omega \\
 & + \int_{\Omega_{l2}^{n+1}} \sigma_{ij}(\mathbf{u}^n + \Delta \mathbf{u}) \frac{\partial \delta u_i}{\partial x_j} d\Omega - \int_{\Omega_{l2}^{n+1}} f_i \delta u_i d\Omega \\
 & - \int_{\Gamma_{l0}^{n+1}} t_i \delta u_i d\Gamma - \int_{\Gamma_{l1}^{n+1}} t_i \delta u_i d\Gamma - \int_{\Gamma_{l2}^{n+1}} t_i \delta u_i d\Gamma
 \end{aligned} \tag{4.35}$$

In an iterative solution process with the Newton-Raphson method, a consistent linearization by taking the directional derivative of  $G^{n+1}$  along incremental displacement vector  $\Delta \mathbf{u}$ , yields the tangent stiffness matrix. For the  $i$  -  $th$  iteration, the assembled equations have the following

structure.

$$\begin{bmatrix} K^{l0/1,l0/1} & K^{l0/1,l2} \\ K^{l2,l0/1} & K^{l2,l2} \end{bmatrix}^i \begin{Bmatrix} \Delta U^{l0/1} \\ \Delta U^{l2B} \end{Bmatrix}^i = \begin{Bmatrix} \Delta F^{l0/1} \\ \Delta F^{l2} \end{Bmatrix}^i \quad (4.36)$$

Here  $\Delta U^{l0/1}$  corresponds to displacements at nodes ( $\mathbf{nd}^{l0/1}$ ) that belong to elements  $E_{l0}$  and  $E_{l1}$  in the computational region  $\Omega_{l0} \cup \Omega_{l1}$  as shown in figure 4.13. It should be noted that they also include nodes at the interface of elements  $E_{l0}/E_{l1}$  and elements  $E_{tr}$ . The displacements  $\Delta U^{l2B}$  on the other hand corresponds to nodes ( $\mathbf{nd}^{l2/tr}$ ) on the interfaces of elements  $E_{tr}$  and elements  $E_{l2}$  or to nodes ( $\mathbf{nd}^{l2/2}$ ) on the interfaces between two  $E_{l2}$  elements. Contributions to the stiffness matrix  $[K]$  and load vector  $\{F\}$  for elements in  $\Omega_{l0} \cup \Omega_{l1}$  may be obtained as

$$(K_{i\alpha j\beta}^{l0/1,l0/1})^i = \int_{\Omega_{l0}^{n+1} \cup \Omega_{l1}^{n+1}} \frac{\partial N_\alpha^G}{\partial x_i} \frac{\partial \Sigma_{ij}}{\partial e_{kl}} \frac{\partial N_\beta^G}{\partial x_l} d\Omega$$

$$(F_{i\alpha}^{l0/1})^i = \int_{\Omega_{l0}^{n+1} \cup \Omega_{l1}^{n+1}} f_i N_\alpha^G d\Omega + \int_{\Gamma_{l0}^{n+1} \cup \Gamma_{l1}^{n+1}} t_i N_\alpha^G d\Gamma - \int_{\Omega_{l0}^{n+1} \cup \Omega_{l1}^{n+1}} \Sigma_{ij} (\mathbf{u}_n + \Delta \mathbf{u})^i \frac{\partial N_\alpha^G}{\partial x_j} d\Omega$$

$\alpha, \beta$  correspond to the node numbers and  $N_\alpha$  are the shape functions of macroscopic elements. For the elements  $E_{tr}$  and  $E_{l2}$  belonging to  $\Omega_{l2}$ , contributions to the stiffness matrix and load vectors are obtained by VCFEM calculations, together with static condensation. The transition element facilitates continuous variation from microscopic to macroscopic elements without jumps or discontinuities. On the  $E_{l0/1}$ - $E_{tr}$  interfaces, this is accomplished by constraining displacements at nodes  $\mathbf{nd}^{sc}$  to conform to displacement interpolation of the adjacent  $E_{l0}$  or  $E_{l1}$  elements. The constraints at the nodes  $\mathbf{nd}^{sc}$  are applied in terms of displacements at  $\mathbf{nd}^{l01/tr}$  as

$$\{\Delta U^{sc}\} = [Q] \{\Delta U^{l01/tr}\} \quad (4.37)$$

where  $[Q]$  is the constraining matrix. For bilinear QUAD4 level-0/1 elements, each row of  $[Q]$  consists of the inverse of the distance of the constrained node to the corner nodes. The interfaces with the  $E_{l2}$  elements, i.e. the  $E_{l2}$ - $E_{tr}$  interfaces are treated in the same way as  $E_{l2}$ - $E_{l2}$  interfaces.

The displacements  $\Delta U^{l2B}$  in equation (4.36) correspond to those at the boundary nodes ( $\mathbf{nd}^{l2/2}$ ,  $\mathbf{nd}^{l2/tr}$ ,  $\mathbf{nd}^{l01/tr}$  and  $\mathbf{nd}^{sc}$ ) of level-2 elements that contain the microstructural VCFE model. To account for the contribution of the internal nodes ( $\mathbf{nd}^{l2I}$ ), it is therefore necessary to use static condensation and recovery process for representing the VCFEM displacement solutions at the internal nodes  $\Delta U^{l2I}$  in terms of the displacements at boundary nodes  $\Delta U^{l2B}$ , where

$$\begin{Bmatrix} \Delta U^{l2B} \end{Bmatrix} = \begin{Bmatrix} \Delta U^{l2/2} \\ \Delta U^{l2/tr} \\ \Delta U^{l01/tr} \\ \Delta U^{sc} \end{Bmatrix} = \begin{bmatrix} I & 0 & 0 & 0 \\ 0 & I & 0 & 0 \\ 0 & 0 & I & 0 \\ 0 & 0 & 0 & Q \end{bmatrix} \begin{Bmatrix} \Delta U^{l2/2} \\ \Delta U^{l2/tr} \\ \Delta U^{l01/tr} \end{Bmatrix} \quad (4.38)$$

where  $[I]$  and  $[Q]$  are the identity and constraint matrices respectively. In a VCFEM solution process the stiffness matrix and the load vector may be partitioned accordingly as

$$\begin{bmatrix} K^{l2B,l2B} & K^{l2B,l2I} \\ K^{l2I,l2B} & K^{l2I,l2I} \end{bmatrix} \begin{Bmatrix} \Delta U^{l2B} \\ \Delta U^{l2I} \end{Bmatrix} = \begin{Bmatrix} \Delta F^{l2B} \\ \Delta F^{l2I} \end{Bmatrix} \quad (4.39)$$

Static condensation of the internal degrees of freedom yields

$$\left[ \left[ K^{I2B, I2B} \right] - \left[ K^{I2B, I2I} \right] \left[ K^{I2I, I2I} \right]^{-1} \left[ K^{I2I, I2B} \right] \right] \left\{ \Delta U^{I2B} \right\} = \left\{ \Delta F^{I2B} \right\} - \left[ K^{I2B, I2I} \right] \left[ K^{I2I, I2I} \right]^{-1} \left\{ \Delta F^{I2I} \right\} \quad (4.40)$$

These stiffness matrices and load vectors are then used in the assembly process of equation (4.36).

## 4.9 Adaptation Criteria for Various Levels

It is evident that appropriate criteria need to be established for transitioning the computational subdomains from one level to another. In addition to level transitions, element refinement by *h-adaptation* is also executed in level-0 and level-1 regions for two reasons. The first is to identify and reduce any suitably chosen 'error measure' in the computational model. Secondly, the *h-adaptation* enables the computational model to 'zoom in' on regions of evolving localization due to microscopic non-homogeneity. It reduces the disparity in the macro- and micro- scale elements by successive refinement of macroscopic elements in the critical regions as shown in figures (4.2a, 4.16). The criteria used for element refinement and level transition are delineated below.

• **Level 0/1 h-adaptation** may be executed based on an error measure may be defined as

$$E_e = \|f(\mathbf{u} - \mathbf{u}_h)\| \quad (4.41)$$

where  $\mathbf{u}$  is the true solution,  $\mathbf{u}_h$  is its finite element approximation,  $f$  is any appropriate function of deformation e.g. energy, stresses, strains etc., and  $\|\cdot\|$  denotes a norm of the function. Substantial work on *h*-method of mesh refinement e.g. [40, 41, 42] have proposed various forms of  $f$  and norms to optimize the computational effort and improve reliability. In this work, elements are subdivided based on an element level parameter defined as

$$(E_e)_{cr} = qi \frac{\|f(\mathbf{u}_h)\|}{\sqrt{NE}} \quad (4.42)$$

where  $(E_e)_{cr}$  corresponds to a threshold element parameter, above which the element needs to be refined and  $qi$  is a prescribed quality index.  $\|f(\mathbf{u}_h)\| = \sum_{e=1}^{NE} \|f(\mathbf{u}_h)\|_e$  is the sum of element norms of any function for the entire computational domain and  $NE$  is the number of elements. In this work  $\|f(\mathbf{u}_h)\|_e$  is taken to be the maximum difference in plastic work with neighboring elements. Accordingly a value of  $qi=1.5$  is found to be satisfactory for this study.

• **Level-0 to level-1 transition** of  $E_{I0}$  elements takes place in accordance with criteria based on macroscopic variables e.g.  $(\Sigma, \mathbf{e})$  in the continuum model that are related to critical microscopic variables. Additionally, this transition is activated when the continuum level model in section 4.5.1 starts to digresses considerably from the results of two-scale homogenization. Different criteria are used for composite and porous materials.

A. For composite microstructure with inclusions:

$$(\Sigma_I) \geq \Sigma^{cr} = r * \sigma^{cr} \quad \text{and/or} \quad \frac{(\Sigma_{xx} + \Sigma_{yy})}{2} \geq \Sigma_h^{cr} \quad (4.43)$$

Here  $\Sigma_I$  is the maximum principal stress in  $E_{I0}$ ,  $\Sigma^{cr}$  is a critical stress that is a pre-determined fraction  $r$  of the critical fracture stress ( $\sigma^{cr}$ ) for microstructural inclusions. The fraction  $r$  is

selected to be  $\frac{1}{3}$  in this study. The second condition is established since the earliest digression from the homogenization results is observed for biaxial loading, and  $\Sigma_h^{cr}$  established from the results of section 4.5.4.

B. For porous microstructure with voids: Strain based criteria are deemed more important in the case of damage in porous materials and hence transition is activated when

$$(\bar{\epsilon}^p) \geq (\bar{\epsilon}^p)^{cr} = r * (\epsilon^p)^{cr} \quad \text{and/or} \quad \frac{(e_{xx} + e_{yy})}{2} \geq e_H^{cr} \quad (4.44)$$

where  $\bar{\epsilon}^p (= \sqrt{\frac{1}{2} e_{ij}^p e_{ij}^p})$  is the macroscopic effective plastic strain in  $E_{l0}$  and  $(\bar{\epsilon}^p)^{cr}$  is a pre-determined fraction  $r$  of a suitably assessed high microstructural plastic strain  $(\epsilon^p)^{cr}$ . Again  $e_H^{cr}$  is established from the limiting values of biaxial strain in section 4.5.4.

• **Level-1 to level-2 transition** of  $E_{l1}$  elements occur when a sufficiently high spatial resolution is attained by h-refinement and when the RVE is deemed to be on the verge of significant damage evolution. The adaptive criteria, which monitor the transition from elements  $E_{l1}$  to  $E_{l2}$  are prescribed in terms of topological evolution of microscopic damage as:

A. For composite microstructure with inclusions:

$$R_{damage} = \frac{NDP}{NP} \geq R_{cr} \quad (4.45)$$

B. For porous microstructure with voids:

$$R_{damage} = \frac{ADR}{AR} \geq R_{cr} \quad (4.46)$$

where  $R_{damage}$  is the ratio of the number of damaged inclusions (NPD) to the total number of inclusions (NP) for composites. For porous microstructures, it is the ratio of the damaged area corresponding to regions which have high plastic strains to the total RVE area.  $R_{cr}$  is a prescribed critical ratio and varies from problem to problem.

## 4.10 Numerical Examples with the Adaptive Multilevel Model

Numerical examples are solved to understand the effect of structural geometry and microstructural morphologies on the macroscopic and microscopic responses. In all examples, the inclusions are assumed to be linear elastic which can crack by the principal stress criterion and the matrix is elastic-plastic. In the first example, a RVE consisting of a single circular inclusion is modeled by level-1 and level-2 elements under applied uniaxial tension loading. In the first case the  $E_{l1}$  macroscopic element is coupled with the microscopically periodic RVE by asymptotic homogenization, while in the second case, the tension load is directly applied on one edge of the Voronoi cell element  $E_{l2}$  model of the RVE. The loading is continued beyond the level of inclusion cracking. This is represented by the loss of stress carrying capacity in the averaged stress-strain plot of figure 4.14a. Though the response is similar in the initial elastic phase, it diverges with the onset of plastic flow. The damage occurs earlier in the level-1 element due to the additional constraint of periodicity. The contour plots of inclusion maximum principal stress, normalized by the critical stress  $\sigma^{cr}$ , are compared at a macroscopic strain 2.1% in figure 4.14. This is just before cracking by the level-1 model. A

considerably lower stress level is seen for the level-2 model. Such over-estimation of stresses with periodicity boundary condition near free boundaries necessitate the use of the proposed multi-level models.

#### 4.10.1 Effects of inhomogeneity size (Scale effect)

Neglecting scale effects, that reflect the actual size of microstructural constituents, is a characteristic of homogenization with assumptions of statistical periodicity of a vanishingly small RVE. While elements  $E_{l0}$  and  $E_{l1}$  conform to this restriction, the level-2 elements  $E_{l2}$  in this work depict the actual size of the microstructure through the multi-level coupling and hence scale effects prevail.

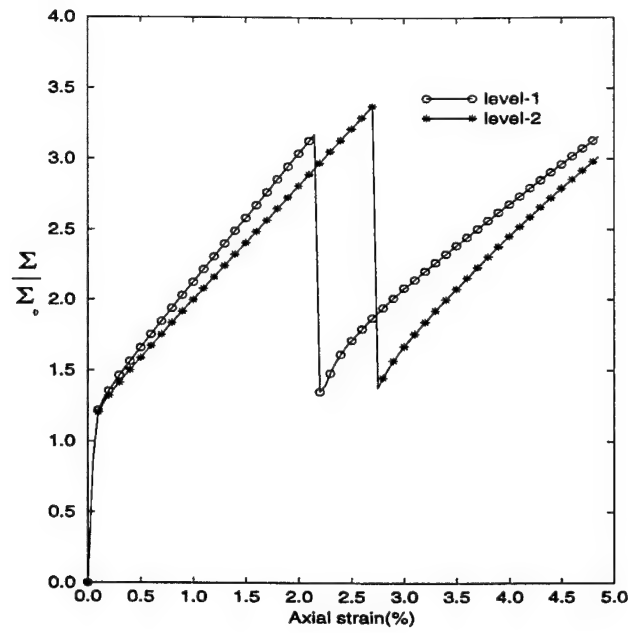
In this example the effect of particle or void size on the evolution of damage is investigated. The two different microstructural RVE's considered in figure 4.15b (i and ii) have identical distribution (square edge) and same particle or void area fraction of  $V - f = 20\%$ . But the RVE sizes are different in that, the size of the smaller RVE(i) is 0.5mm x 0.5mm while that of the larger RVE(ii) is 1mm x 1mm. The macroscopic structure is a square plate with a square hole, for which the initial level-0 mesh with dimensions is shown in figure 4.15a. Only a quarter of the plate is modeled from symmetry considerations. The smallest size of macroscopic element allowed in this analysis by  $h$  - adaptation is set to 1mm. Thus the  $E_{l2}$  elements contain only one element in the VCFEM model for the larger RVE(ii) but four elements in the VCFEM model for the smaller RVE(i). The material properties for both composite and porous materials are as follows.

Aluminum matrix (Elastic-Plastic): Young's Modulus ( $E_m$ )=68.3 GPa, Poisson Ratio ( $\nu_m$ )=0.30, Initial Yield Stress ( $Y_0$ )= 55 MPa, and Post Yield hardening law:  $\sigma_{eqv} = Y_0 + 2.08\epsilon_{eqv}^{pl}$

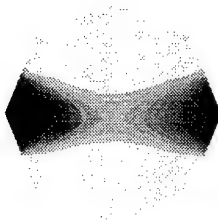
Alumina particle (Elastic): Young's Modulus ( $E_c$ )= 344.5GPa, Poisson Ratio ( $\nu_c$ )= 0.26, Critical particle cracking stress ( $\sigma^{cr}$ )=0.3GPa

The load is applied in 20 equal increments upto a total displacement of 1 mm as shown in figure 4.15a. For the composite microstructures, figure 4.16 depicts the evolved macroscopic and level-2 computational domains at the end of loading stages. The level-0, level-1, level-2 elements are shown in white, grey and black respectively for the adapted macroscopic mesh in 4.16a and b. The evolution of the levels and mesh with h-adaptation is provided in table 3. The effect of the microstructure size becomes more pronounced with increasing deformation. A larger level-2 domain (29 macroscopic elements) with a smaller level-0 domain is evidenced for the smaller RVE(i). The effect of RVE size on the pattern of particle cracking is very significant. The level-2 region shows 24 cracked particles for the RVE(i) as opposed to 6 cracked particles for the RVE(ii). The path of evolution of cracked particles is quite different for the two models. For the RVE(ii), the aggregate microscopic cracks is found to propagate perpendicular to the macroscopic loading direction and all the microcracks have the same orientation as the chain or macrocrack. For the smaller particles in RVE(i), the chain of microcracks or the macrocrack is observed to move at 45° to the loading direction with individual microcracks predominantly at 90° to the loading direction.

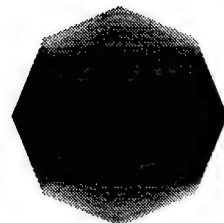
The contour plots of macroscopic and microscopic plastic strain distribution at the final loading stage are shown in figures 4.17 and 4.18 for the two microstructures. The macroscopic strain distribution for both models shows higher strain concentration at the corner of square hole with increased loading. While the macroscopic strains are not very different for the two RVE's, significantly larger local plastic strains are seen in the level-2 microstructure of RVE(i). A better representation of



(a)



(b)



(c)

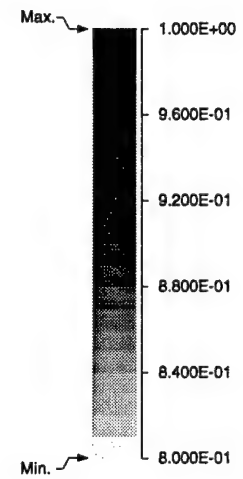


Figure 4.14: (a) Macroscopic axial stress-strain plots for a single RVE in tension modeled by level-1 and level-2 elements; Maximum principal stress distribution in the inclusion by (b) level-2 element and (c) level-1 element.

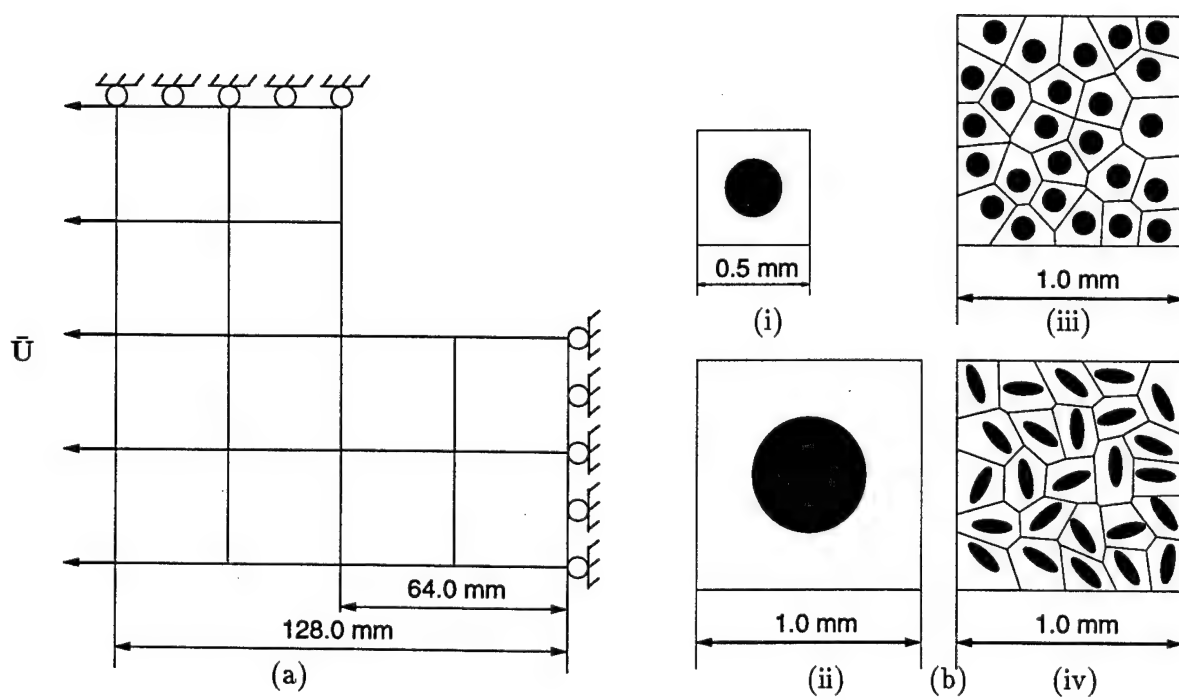
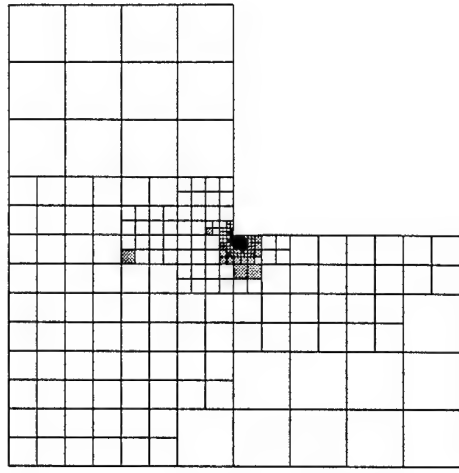
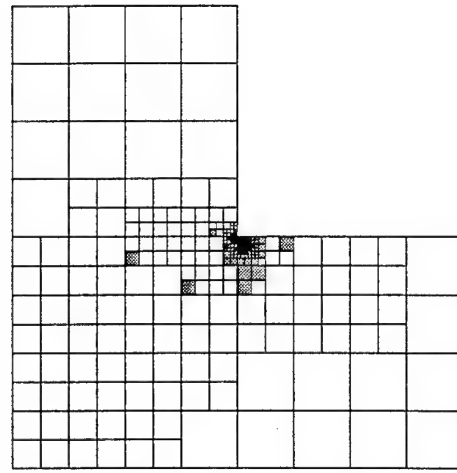


Figure 4.15: (a) A quarter of the level-0 starting macroscopic model of a square plate with a square hole, (b) four different microstructural RVE's for the plate model.

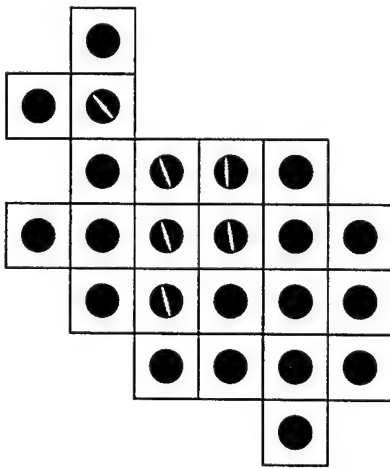




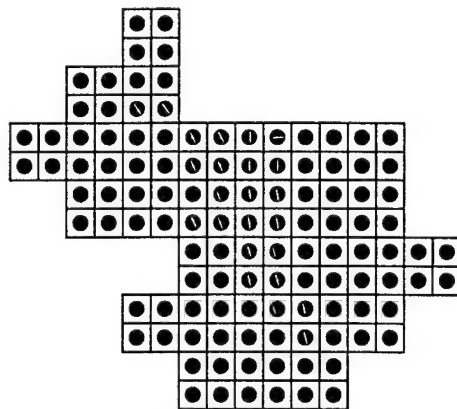
(a)



(b)



(c)



(d)

Figure 4.16: Macroscopic three level evolved mesh for the composite material at the end of the loading cycle for (a) the larger RVE (ii) and (b) smaller RVE (i); the corresponding level-2 region with the (c) the larger RVE (ii) and (d) smaller RVE (i). Level-0 is with white elements, level-1 is with grey elements and level-2 is with black elements.

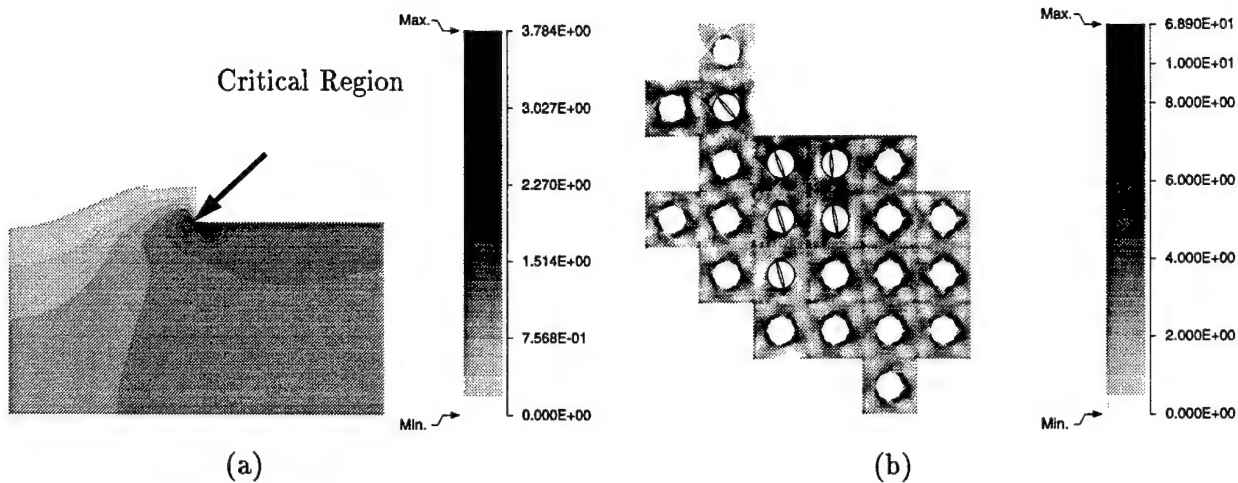


Figure 4.17: Contour plot of plastic strain  $\bar{\epsilon}^p$  for the composite square plate: (a) the macroscopic averaged strain and (b) the level-2 microscopic strain at the critical region for the larger RVE (ii) model.

this difference is seen in the graphs of figures 4.19 and 4.20. The macroscopic (averaged) stress  $\Sigma_{xx}$  history at the critical corner in figure 4.19 does not indicate significant difference and hence exhibits little scale effect. The stress drops in this figure correspond to particle damage. The histogram of the evolution of particle cracking however shows a considerably different pattern and a much higher rate of cracking for RVE(i).

The same problem is solved for porous microstructures with the two sized RVE's, but with a total displacement of 0.4mm. The evolved levels and meshes in the computational models at the end of loading are shown in figures 4.21a and b and the corresponding level-2 microstructures in figures 4.21c and d. The evolution of the computational domain is also charted in table 4. It is interesting to note that the difference in response for the two RVE's is insignificant in this case. This may be attributed to lack of matrix damage or softening in the model. The plastically hardening matrix does not trigger adequate difference in the adaptation criteria as the particle cracking does for composites. A larger level-1 domain opens up with the adaptation criteria for elements which appear to be on the verge of strain localization, but subsequently do not make the transition to level-2. The contour plots of macroscopic and microscopic plastic strain distribution in figures 4.22 and 4.23, show similar macroscopic strain distributions, but higher strains for the microscopic model with smaller porosity RVE(i), due to the proximity of voids. This again shows the scale effect on the solution.

#### 4.10.2 Homogenization vs. multi-level simulation

The effect introducing level-2 elements on both macroscopic and microscopic response is studied by comparing a pure level-1 simulation of the square composite plate in the previous example with a multi-level simulation. The results shown are for the larger particles in RVE(ii). The figure 4.24

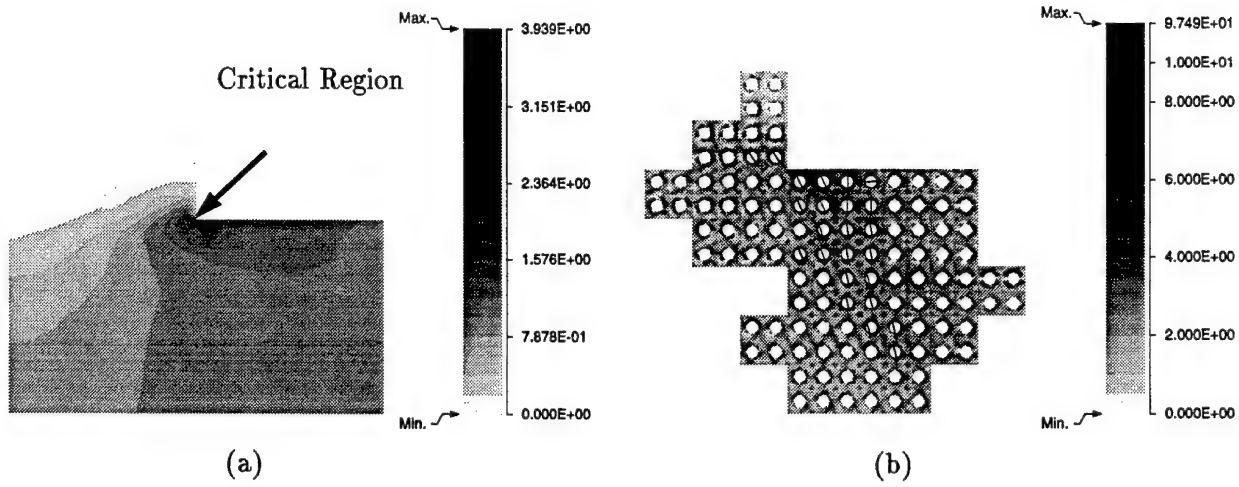


Figure 4.18: Contour plot of plastic strain  $\bar{\epsilon}^p$  for the composite square plate: (a) the macroscopic averaged strain and (b) the level-2 microscopic strain at the critical region for the smaller RVE (i) model.

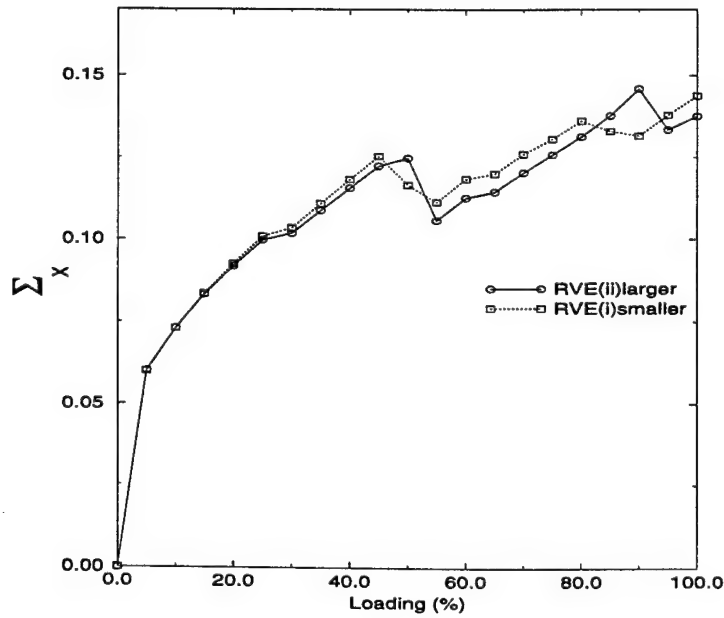


Figure 4.19: The evolution of  $\Sigma_{xx}$  at the corner node of square hole for the two microstructures.

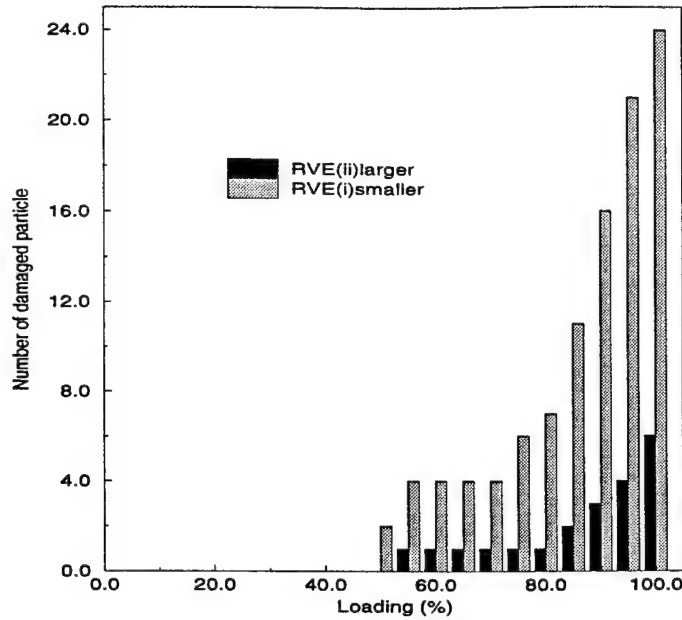


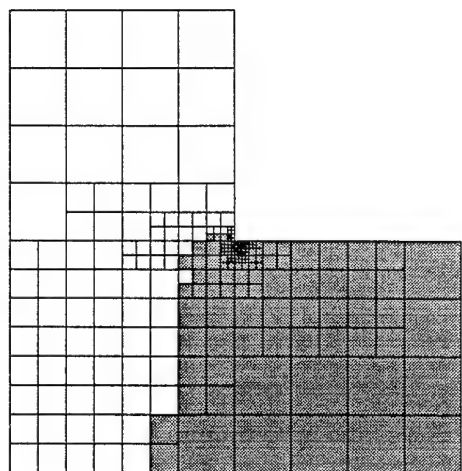
Figure 4.20: Histogram of the number of damaged particles as a function of straining.

shows the microstructure near the inside corner by the two models at the end of loading. The boxed RVE's in figure 4.24a symbolize their periodic repetition. The periodicity constraint results in a considerably large portion of the microstructure being damaged for the homogenized simulation. The direction of the damage evolution indicated by the homogenized model is also different from the level-2 simulations. The stress  $\Sigma_{xx}$  along the section A-B is plotted in figure 4.25 to evaluate the effect of homogenization on stress concentrations near the corner and free edge. The two models behave similarly upto the neighborhood of the corner. While the multi-level model predicts a higher peak near the corner, it subsides considerably to meet the traction free edge conditions. The corresponding microscopic level-2 stress variations for the multi-level model are shown in the inset.

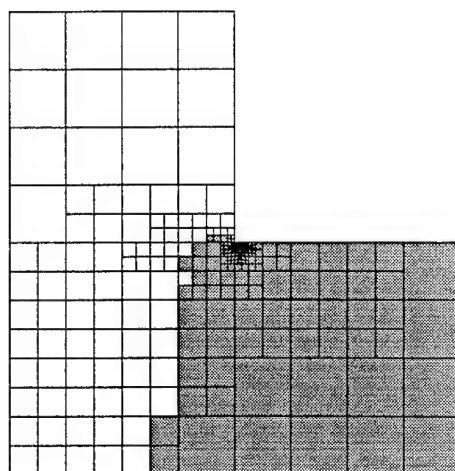
#### 4.10.3 Effect of heterogeneity distribution and shape

To illustrate the influence of particle distribution on the macro-microscopic damage response, two RVEs are selected with same volume fraction (20%), size (1.0mm) and number of particles (25). One has a hardcore distribution (figure 4.15b (iii)), which is a random distribution with a minimum permissible distance between particles, while the other has one cluster in a hardcore background. Proximity of particles within the cluster is known to initiate damage in discrete microstructures. The starting macroscopic mesh is the same as in the previous examples and a total displacement of 0.55mm is applied on the edge in equal increments. The smallest allowed size of macroscopic elements by h-adaptation is set to 1mm such that each  $E_{l2}$  element consists of one RVE.

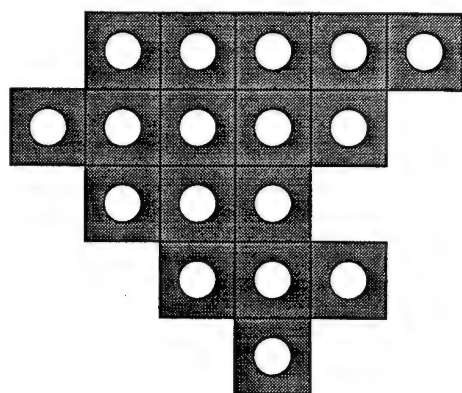
The evolved macroscopic models for the two RVE's, at the finish of the loading cycle, are shown in figures 4.26a and b. The level-2 region (black) for the clustered RVE is larger than that for



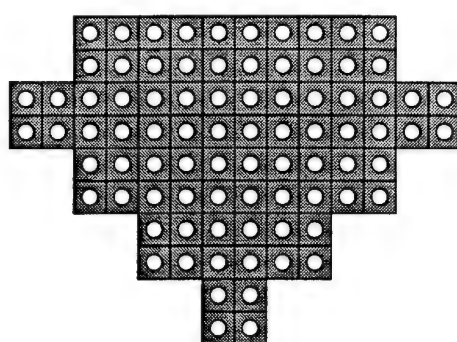
(a)



(b)



(c)



(d)

Figure 4.21: Macroscopic three level evolved mesh for the porous material at the end of the loading cycle, for (a) the larger RVE (ii) and (b) smaller RVE (i); The corresponding level-2 region with the (c) the larger RVE (ii) and (d) smaller RVE (i). Level-0 is with white elements, level-1 is with grey elements and level-2 is with black elements.

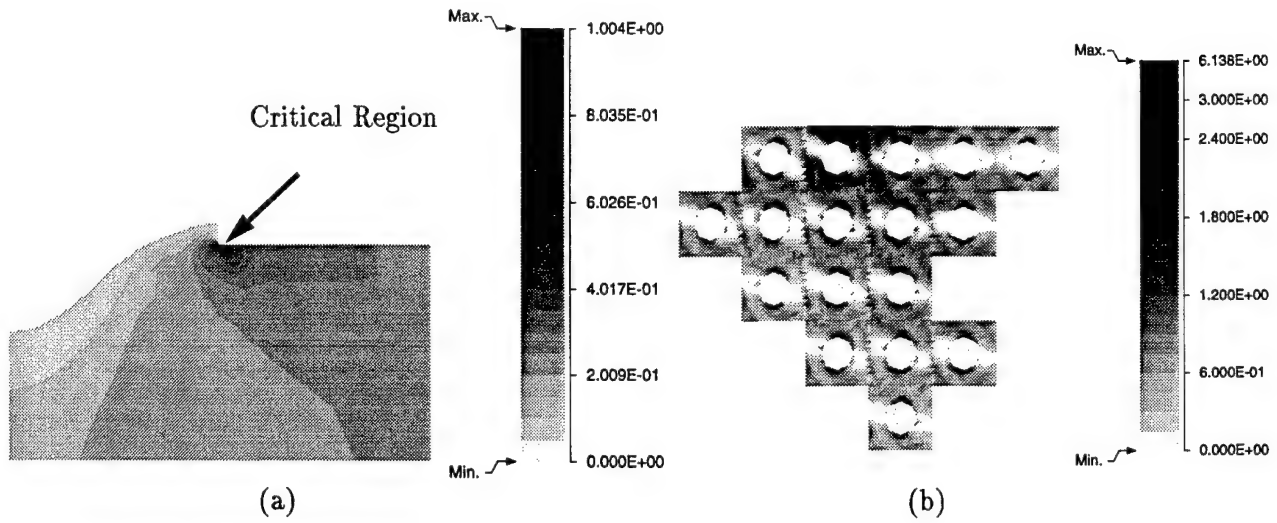


Figure 4.22: Contour plot of plastic strain  $\bar{\epsilon}^p$  for the porous square plate: (a) the macroscopic averaged strain and (b) the level-2 microscopic strain at the critical region for the smaller RVE (ii) model.

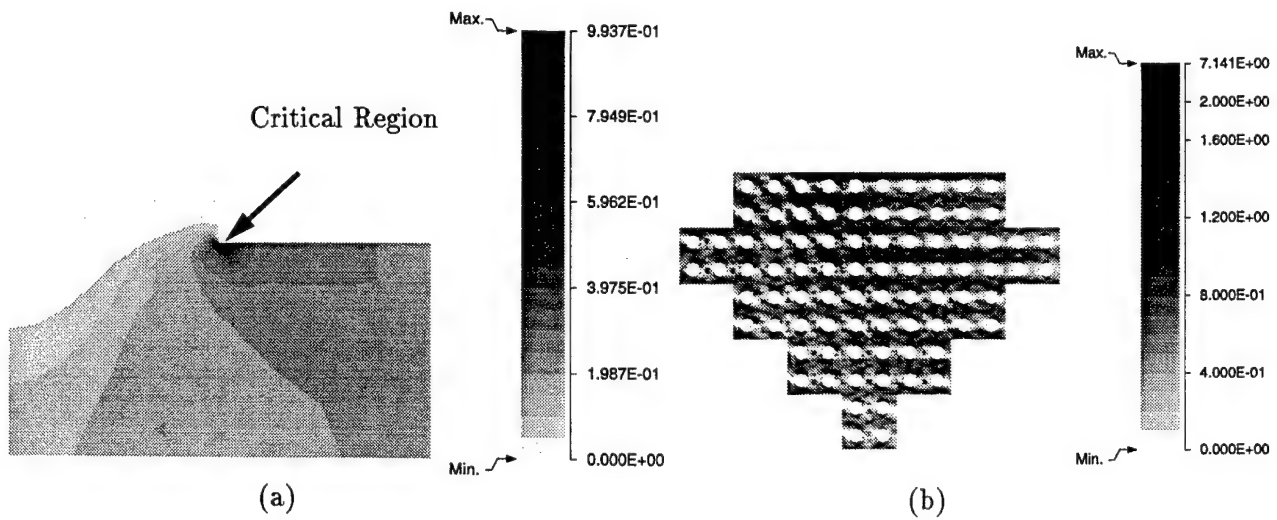


Figure 4.23: Contour plot of plastic strain  $\bar{\epsilon}^p$  for the porous square plate: (a) the macroscopic averaged strain and (b) the level-2 microscopic strain at the critical region for the smaller RVE (i) model.

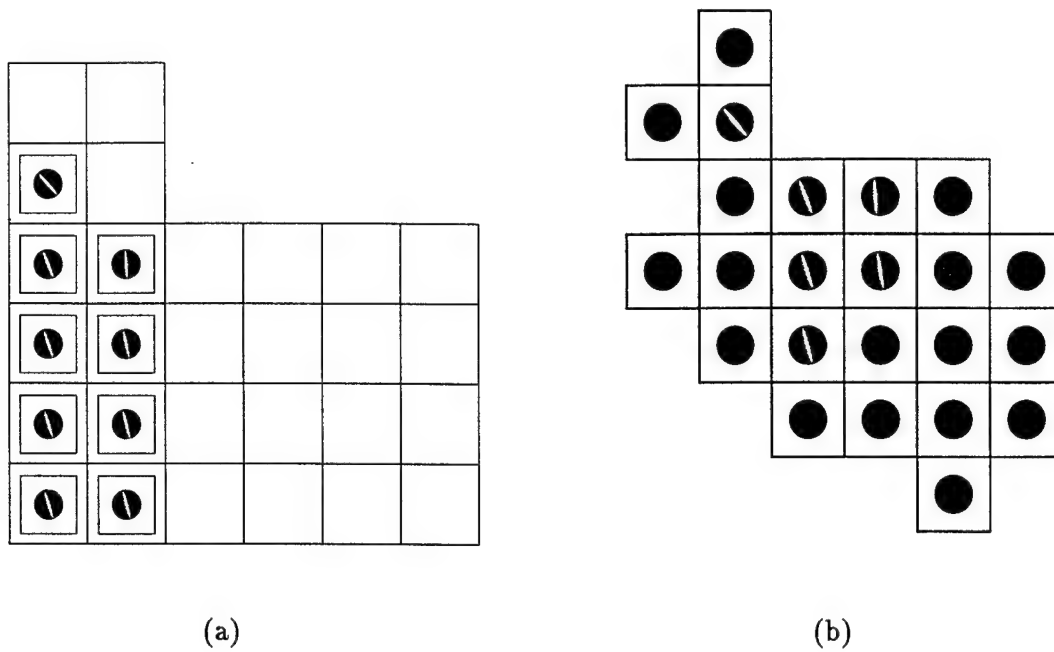


Figure 4.24: A comparison of the microstructural evolution near the inside corner by (a) complete level-1 analysis and (b) adaptive multi-level analysis.

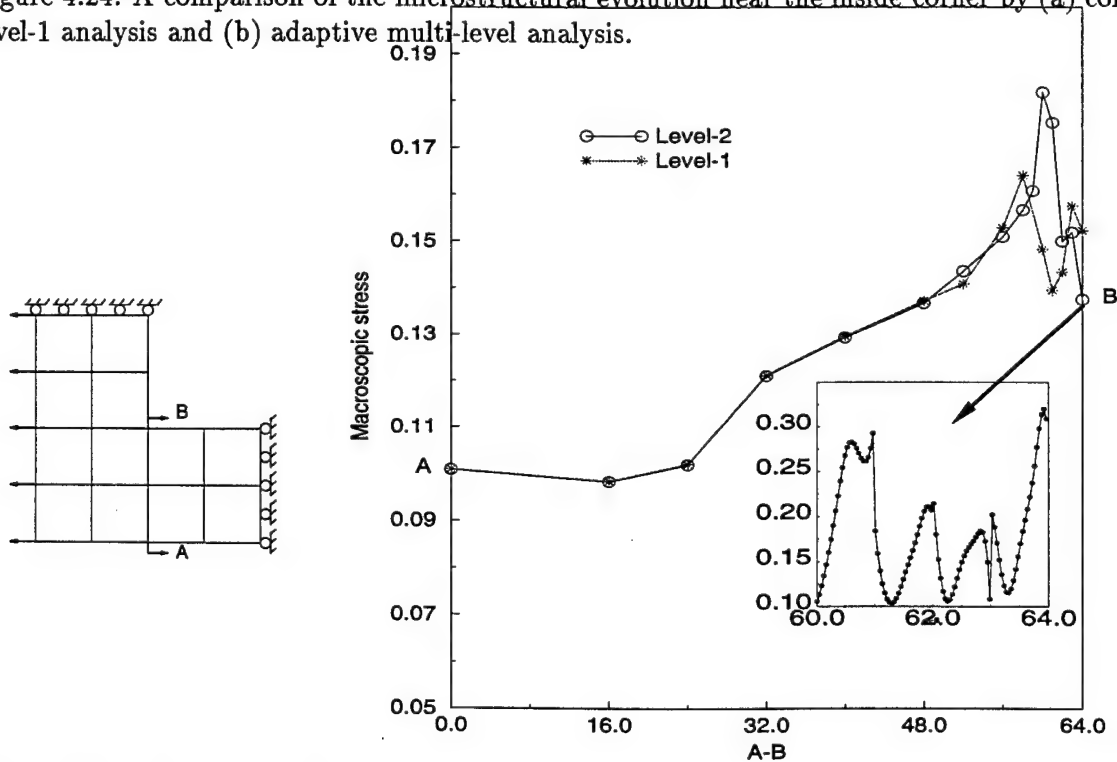


Figure 4.25: Comparison of macroscopic stress  $\Sigma_{xx}$  along section A-B by level-1 and multi-level analysis.

the hardcore RVE. Within the  $E_{l2}$  elements, only one element for the hardcore distribution experiences particle damage as shown in figure 4.26d. However, several  $E_{l2}$  elements for the clustered microstructure exhibit particle damage, mainly within the cluster (figure 4.26e). While the macroscopic averaged plastic strains show very little difference for the different microstructures in figures 4.27a and 4.28a, the microscopic plots in figures 4.27b and 4.28b clearly depict the influence of distribution. Much higher levels of effective plastic strain values are observed within the cluster, compared to significantly lower levels in the hardcore RVE. Figure 4.30 shows the evolution of macroscopic stress  $\Sigma_{xx}$  at the corner of the square hole and the number of damaged particles as a function of straining. The stress drops to lower values for the clustered RVE due to a larger damage microstructure. More than twice the number of particles are damaged for the clustered case as shown in the histogram.

To investigate the influence of shape, a RVE (see figure 4.15b (iv)) with the same volume fraction (20%), size (1.0mm) and number (25) is considered. The particles are elliptical with aspect ratio 3.0 and randomly distributed and oriented. The evolved macroscopic model in figures 4.26c shows a larger level-2 region compared with other two microstructures, with several  $E_{l2}$  elements exhibiting particle damage. The much larger number of cracked particles is also observed from the histogram of figure 4.30b. For this case, both macroscopic and microscopic plastic strains in figure 4.29 are also considerably larger. The macroscopic stress  $\Sigma_{xx}$  shows a larger drop due to the increased damage in the microstructure.

#### 4.10.4 A heterogeneous plate with a macroscopic holes

A different macroscopic domain, viz. a plate with periodically repeated square diagonal array of circular holes is considered in this final example. The plate is incrementally loaded using prescribed displacement on the top and bottom surfaces to a total extension of 0.15 mm. Due to periodicity and symmetry, only a part of domain is modeled as shown in figure 4.31. The radius of the circular holes are 50mm for the 100 mm x 100 mm square plate as shown in figure 4.31. The microstructural RVE is a 20% volume fraction 0.4 mm x 0.4 mm square region with a single circular particle. The same material properties as in the previous example are used with the only exception being that the critical particle cracking stress  $\sigma^{cr} = 0.2 \text{ GPa}$ .

The adapted multilevel computational domain is shown in figure 4.32 and the number of elements in each levels with increasing are tabulated in table 5. The level-2 elements are created along a clear path connecting the holes due to localization by particle cracking. Extended portions of the damaged microstructure in level-2 regions are shown in figure 4.32. The macroscopic plastic strain contour in figure 4.33a gives an indication of ‘hot spots’ of evolving damage near the central region. The microscopic strain plots in figure 4.33b show a large fraction of particles cracked and may be interpreted as the initiation of localization to cause failure between the holes.

### 4.11 Conclusions

In this work, an adaptive multi-level computational model is proposed to (a) concurrently predict the evolution of stresses and strains at the structural and microstructural scales and (b) to track the incidence and propagation of microstructural damage. The microstructural analysis is conducted with the Voronoi cell finite element model (VCFEM) for elastic-plastic constituents with



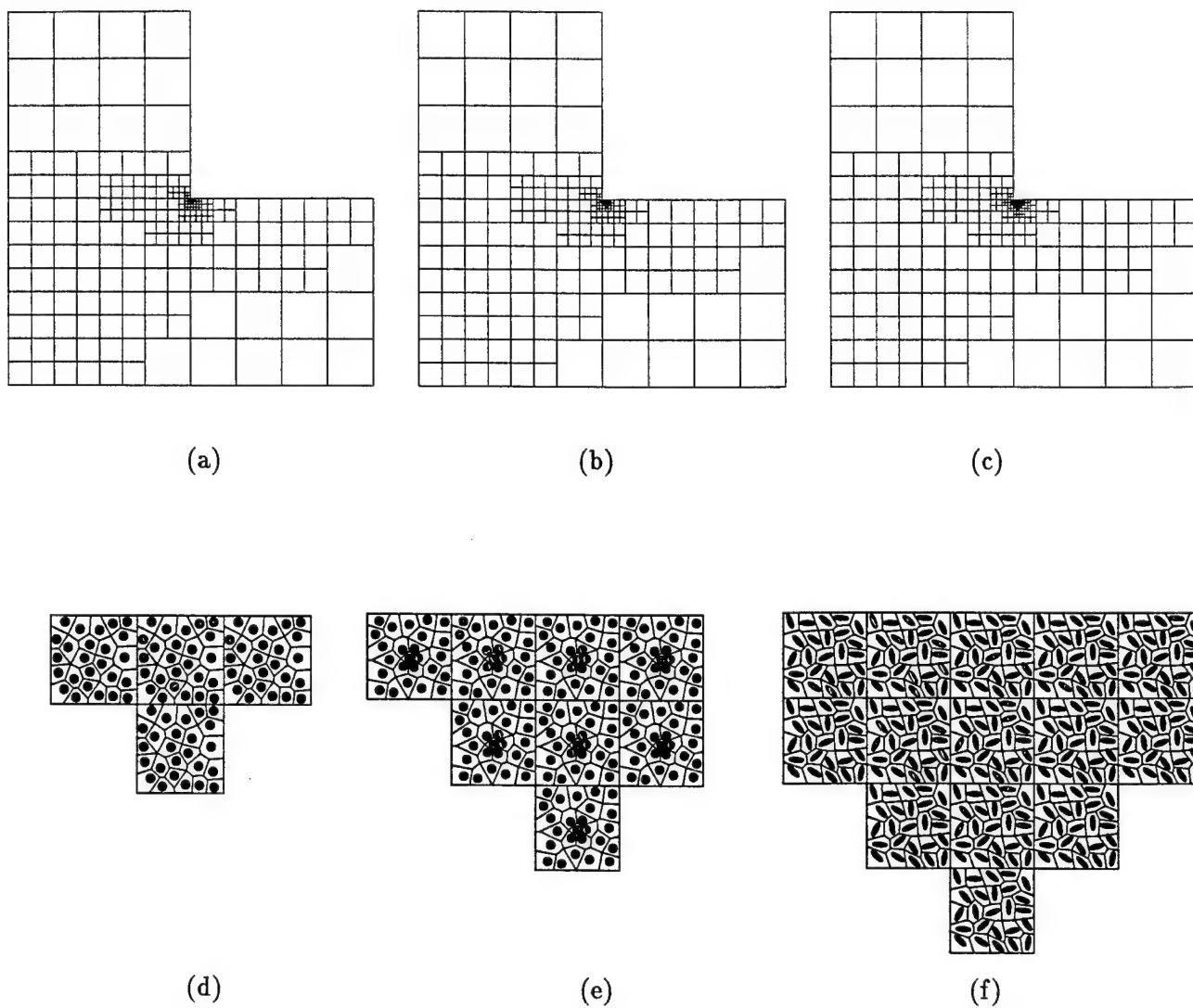


Figure 4.26: Macroscopic three level evolved mesh for the composite material at the end of the loading cycle for (a) hardcore distribution with circular particles, (b) clustered distribution with circular particles, and (c) hardcore distribution with elliptical particles; the corresponding level-2 microstructures for (d) hardcore (e) clustered and (f) elliptical RVE's.

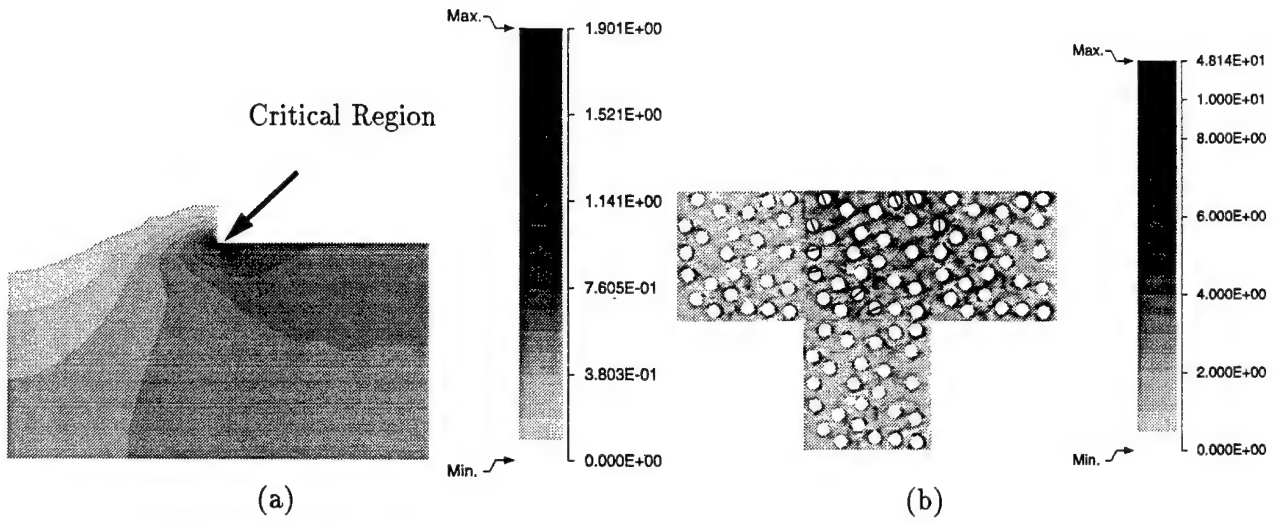


Figure 4.27: Contour plot of plastic strain  $\bar{\epsilon}^p$  for the composite square plate: (a) the macroscopic averaged strain and (b) the level-2 microscopic strain at the critical region for the hardcore RVE model.

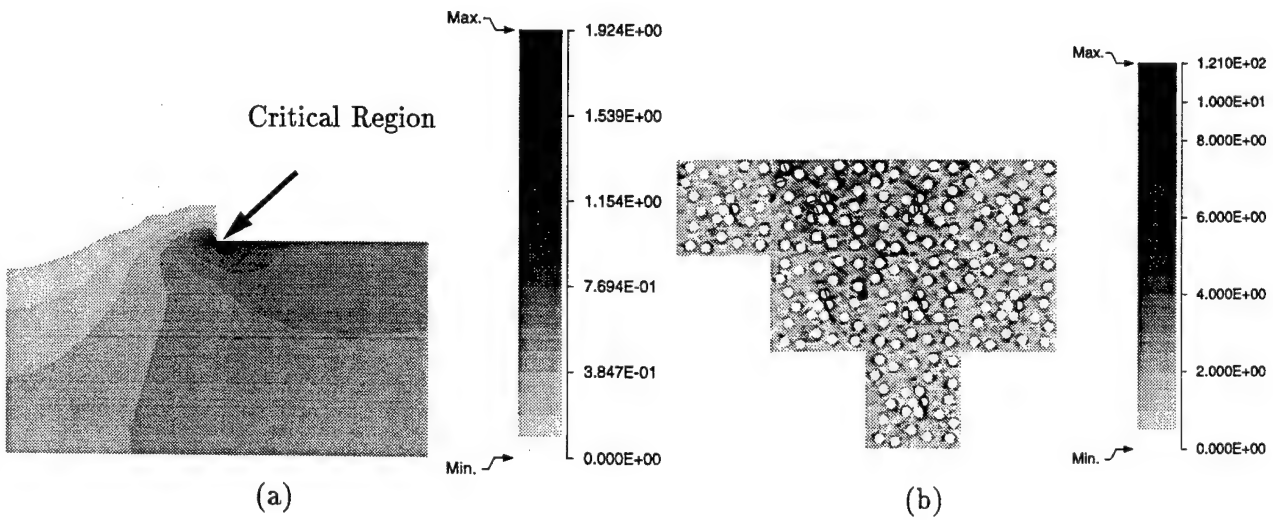


Figure 4.28: Contour plot of plastic strain  $\bar{\epsilon}^p$  for the composite square plate: (a) the macroscopic averaged strain and (b) the level-2 microscopic strain at the critical region for the clustered RVE model.

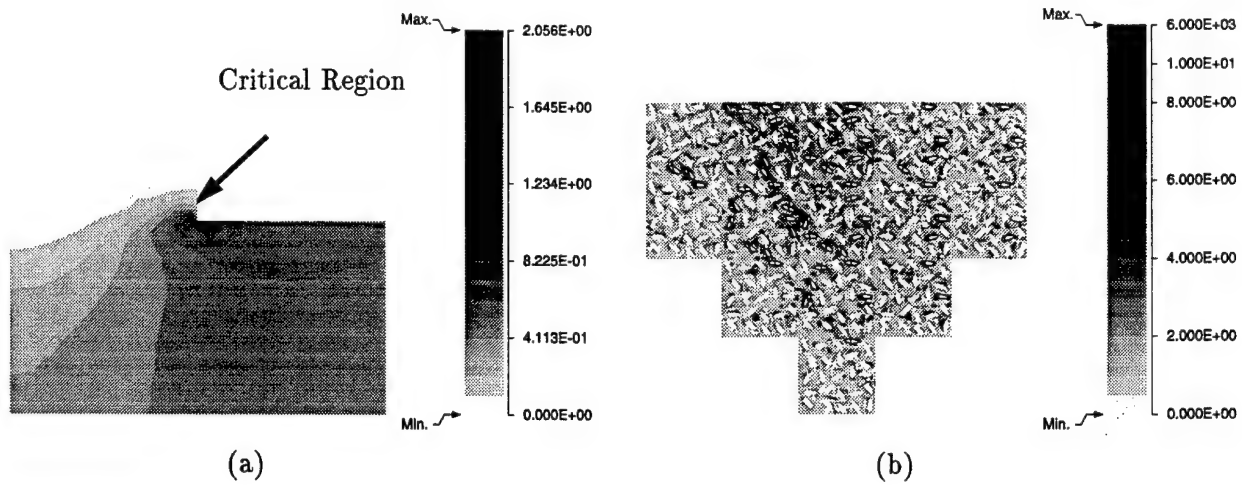


Figure 4.29: Contour plot of plastic strain  $\bar{\epsilon}^p$  for the composite square plate: (a) the macroscopic averaged strain and (b) the level-2 microscopic strain at the critical region for the elliptical RVE model.

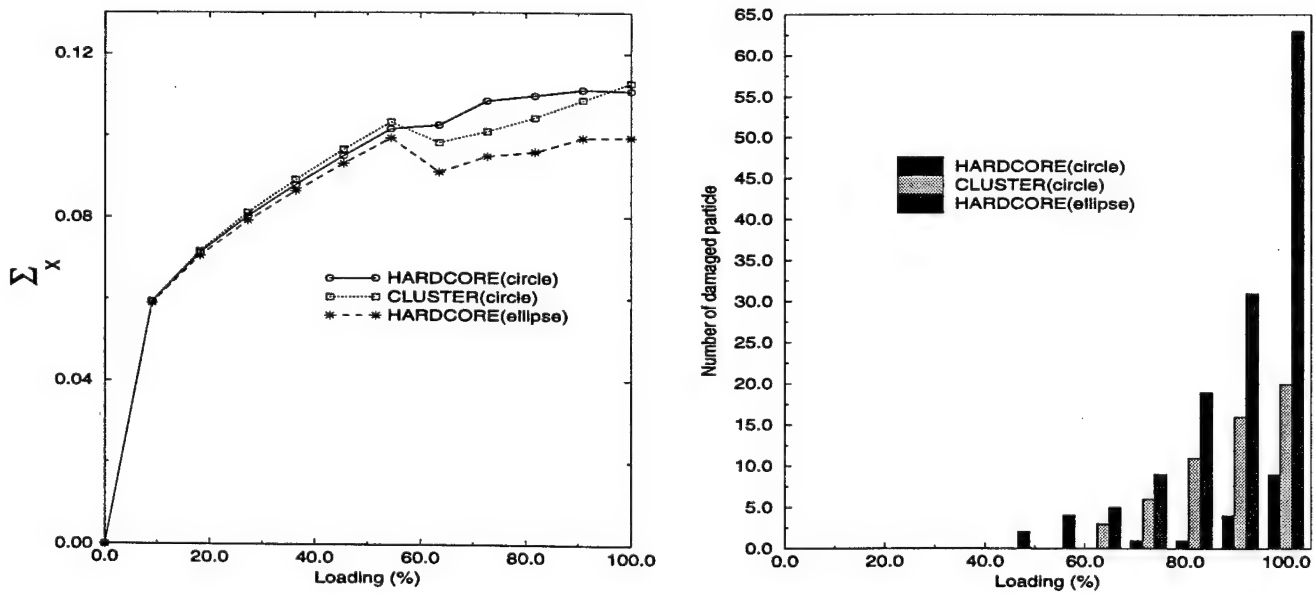


Figure 4.30: The evolution of (a)  $\Sigma_{xx}$  at the corner node of square hole and (b) the number of damaged particles for the three microstructures.

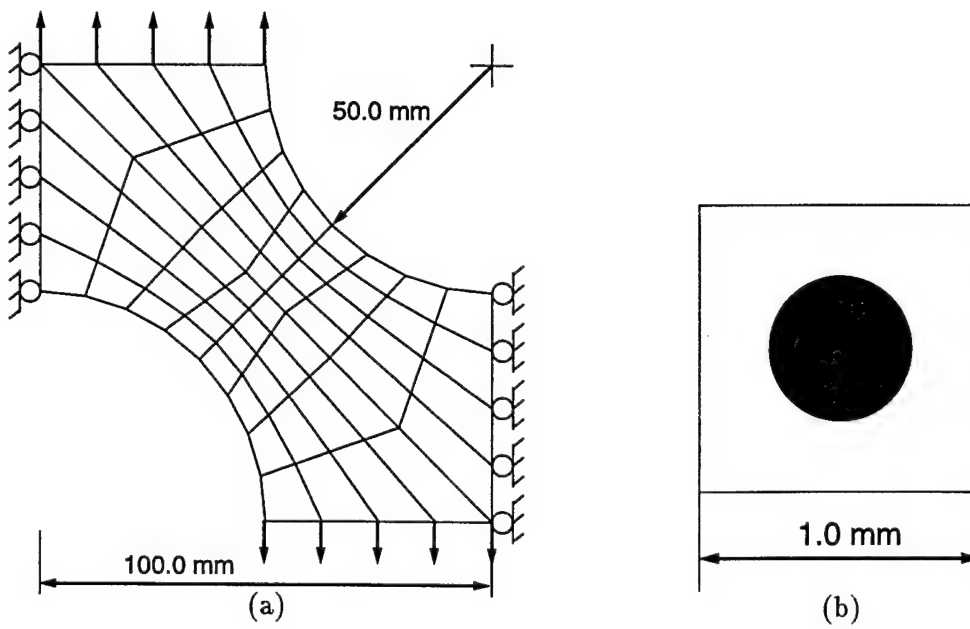


Figure 4.31: (a) Finite element model for a part of the composite plate with two circular holes and (b) the VCFE model of the microstructural composite RVE.

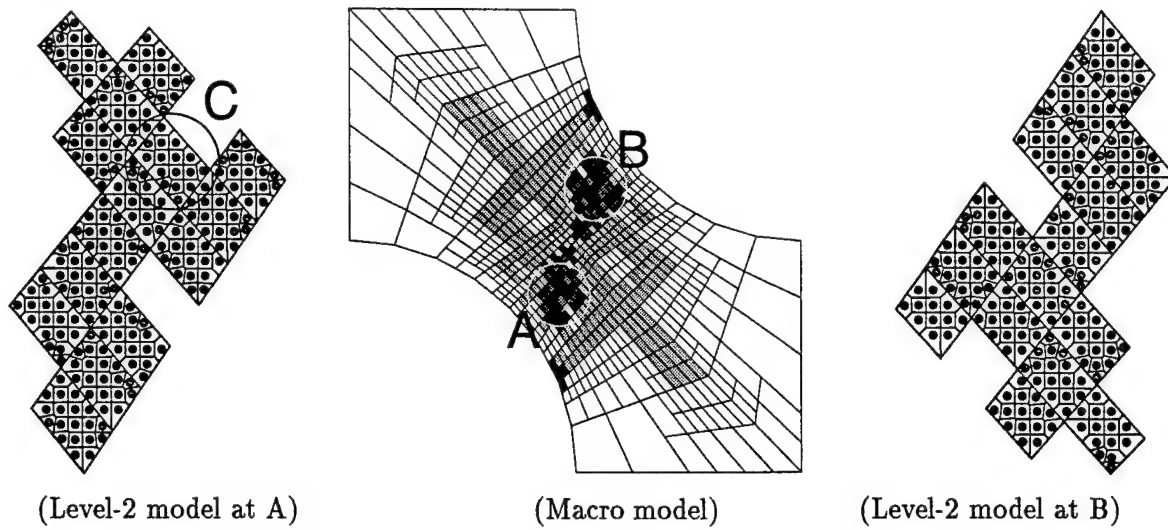


Figure 4.32: Macroscopic three level evolved mesh for the composite plate with two holes at the end of loading. The level-2 regions in the microstructure are shown at the two regions A and B.

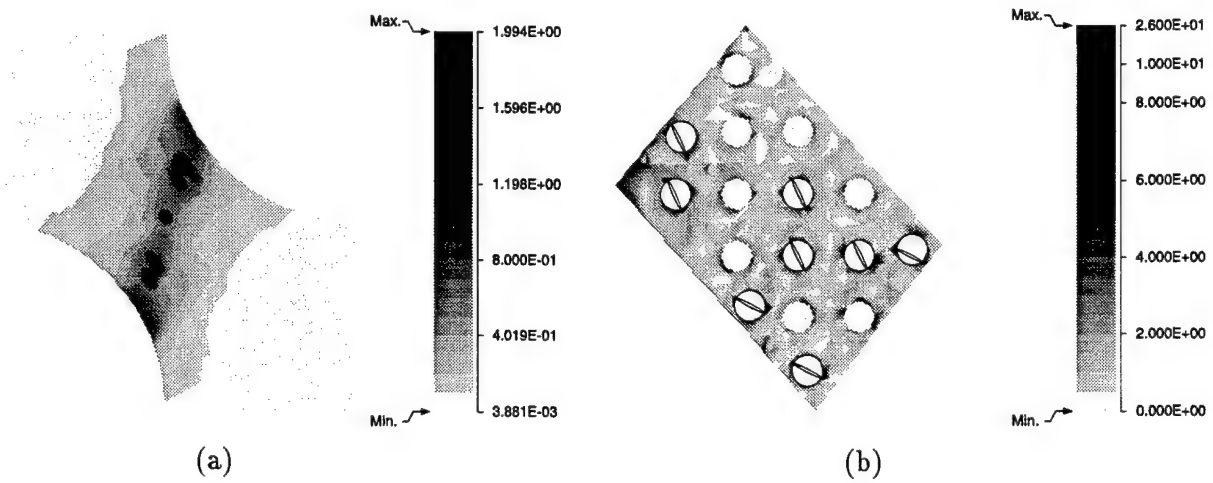


Figure 4.33: Contour plot of (a) the macroscopic plastic strain  $\bar{\epsilon}^p$  and (b) level-2 microscopic plastic strain  $\bar{\epsilon}^p$  at the region C of the microstructure

particle cracking. VCFEM allows continuous changing element topology due to progressive particle cracking with a high level of efficiency and accuracy [23, 28]. This allows modeling large portions of the complex microstructure. A conventional displacement based elastic-plastic FEM code executes the macroscopic analysis. Adaptive methods and mesh refinement strategies are developed to create a hierarchy of computational sub-domains with varying resolution. Such hierarchy allows for differentiation between non-critical and critical regions and help in increasing the efficiency of computations through preferential 'zoom in' regions. Coupling between the scales for regions with periodic microstructure is accomplished through asymptotic homogenization, while other regions of nonuniformity and non-periodicity are modeled by true microstructural VCFEM analysis.

In the hierarchical model, three distinct levels evolve with progressive deformation. In level-0, a piecewise continuous elastic-plastic constitutive law is developed from a numerically created database for macroscopic simulations. The model incorporates exact microstructural morphology in its development and hence is accurate from a micromechanics point of view. This results in high efficiency compared with two-scale analysis by homogenization. Level-1 elements, which manifest with imminent damage, use asymptotic homogenization for predicting macroscopic variables as well as variables in the microstructural RVE. Simultaneously, element refinement by h-adaptation enables zooming in at critical regions of intense deformation. With the rise in local gradients of macroscopic variables and microstructural damage, the assumptions of representative volume element in the microstructure no longer hold. This necessitates a shift in macroscopic simulations to completely microscopic simulations in these regions. This region is termed as the level-2 where an extended portion of the microstructure is directly modeled by VCFEM. The microstructural model is directly interfaced with level-0 or level-1 elements and a coupled analysis is performed.

Several numerical examples are conducted with the multi-level model to examine the effect of various microstructural morphologies on the multi-scale response of composite and porous structural components. Specifically scale effects, effects of microstructural distribution and shapes, and structural geometries, on the mechanical and damage response are investigated. The model performs satisfactorily in identifying critical regions and delineating the necessity of true multi-scale simulations. In conclusions, the multi-level model developed reserves the potential to be a very effective tool in the prediction of structural failure which can be modeled as an aggregate of microscopic damage.

# Bibliography

- [1] Benssousan, A., Lions, J.L. and Papanicoulau G., (1978). Asymptotic analysis for periodic structures, North Holland, Amsterdam.
- [2] Sanchez-Palencia, E., (1980). Non-homogeneous media and vibration theory, Lecture notes in Physics, **127**, Springer-Verlag, Berlin Heidelberg,
- [3] Parton, V.Z. and Kudryavtsev, B.A., (1993). Engineering mechanics of composite structure CRC Press
- [4] Bakhvalov, N. S. and Panasenko, G. P., (1984). Homogenization in Periodic Media. Mathematical Problems of the Mechanics of Composite Materials, Nauka, Moscow
- [5] Fish, J. and Belsky, V., (1995). Multigrid method for periodic heterogeneous media, part II: multiscale modeling and quality control in multidimensional case, *Comp. Meth. in Appl. Mech. and Engng.* **126**, 17-38.
- [6] Fish, J. and Wagiman, A., (1993). Multiscale finite element method for a locally nonperiodic heterogeneous medium, *Comput. Mech.* **12**, 164-180.
- [7] Guedes, J.M. and Kikuchi, N., (1991). Preprocessing and postprocessing for materials based on the homogenization method with adaptive finite element methods, *Comp. Meth. in Appl. Mech, Engng.*, **83**, 143-198.
- [8] Hollister, S.J. and Kikuchi, N., (1992). A comparison of homogenization and standard mechanics analysis for periodic microstructure, *Comput. Mech.* **10**, 73-95.
- [9] Suquet, P., (1985). Local and global aspects in the mathematical theory of plasticity, *Plasticity Today- Modeling methods and Applications*, Sawczuk, A. and Bianchi, G. (eds.), Elsevier, London,
- [10] Fish, J. , Shek,K., Pandheeradi, M. and Shephard, M. S., (1997). Computational Plasticity for composite structures based on mathematical homogenization: Theory and Practice, *Comp. Meth. in Appl. Mech. and Engng.*, **148**, 53-73.
- [11] Guedes, J.M., (1990). Nonlinear computational model for composite material using homogenization, Ph. D. Dissertation, University of Michigan MI.
- [12] Cheng, C. -H., (1992). Modeling of the elasto-plastic behavior for composite materials using homogenization method, Ph. D. Dissertation, University of Michigan MI.

- [13] Lene, F., (1986). Damage constitutive relations for composite materials, *Engin. Frac. Mech.* **25**(5), 713-728.
- [14] Devries, F., Dumontet, H., Duvaut, G. and Lene, F., (1989). Homogenization and damage for composite structures, *Int. J. Num. Meth. in Engng.* **27**, 285-298.
- [15] Belytschko, T. , Fish, J. and Bayliss, A., (1994). The spectral overlay on the finite element solution with high gradients , *Comput. Meth. Appl. Mech. Engng.* **81**, 71-89.
- [16] Robbins D.H. and Reddy, J.N., (1995). Hierarchical modeling of structural sandwiches and multilayered composite panels, Parts I and II, *Intl. Jour. Numer. Meth. Engng.*
- [17] Hughes, T.J.R., (1996). Multiscale phenomena: Green's functions, the Dirichlet-to-Neumann formulation, subgrid scale models, bubbles and the origins of stabilized methods *Comput. Meth. Appl. Mech. Engng.*
- [18] Fish, J. , Nayak, P. and Holmes, M.H., (1994). Microscale reduction error indicators and estimators for a periodic heterogeneous medium, *Comput. Mech.* **14**
- [19] Pagano, N.J. and Rybicki, E.F., (1974). On the significance of effective modulus solutions for fibrous composites, *Jour. Comp. Mat.* **8**, 214-228.
- [20] Zohdi, T.I. , Oden, J.T. and Rodin, G. J., (1996). Hierarchical modeling of heterogeneous bodies, *TICAM Report*, The University of Texas, Austin, Vol. 96-21,
- [21] Oden, J.T. and Zohdi, T.I., (1996). Analysis and adaptive modeling of highly heterogeneous elastic structures, *TICAM Report*, The University of Texas, Austin, Vol. 96-56,
- [22] Moorthy, S. and Ghosh, S., (1996). A Model for analysis of arbitrary composite and porous microstructures with Voronoi cell finite elements, *Int. Jour. Numer. Meth. Engin.* **39**, 2363-2398.
- [23] Moorthy, S. and Ghosh, S., (1998). A Voronoi Cell Finite Element Model for Particle Cracking in Composite Materials, *Comp. Meth. Appl. Mech. Engin.* **151**, 377-400.
- [24] Ghosh, S. , Nowak, Z. and Lee, K., (1997). Quantitative Characterization and Modeling Of Composite Microstructures by Voronoi Cells, *Acta Metall. et Mater.* **45**(6), 2215-2234.
- [25] Ghosh, S. and Liu, Y., (1995). Voronoi cell finite element model based on micropolar theory of thermoelasticity for heterogeneous materials, *Int. Jour. Numer. Meth. Engin.* **38**, 1361-1398.
- [26] Ghosh, S., Lee, K. and Moorthy, S., (1996). Two scale analysis of heterogeneous elastic-plastic materials with asymptotic homogenization and Voronoi cell finite element model, *Comp. Meth. Appl. Mech. Engin.* **132**, 63-116.
- [27] Ghosh, S., Lee, K. and Moorthy, S., (1995). Multiple scale analysis of heterogeneous elastic structures using homogenization theory and Voronoi cell finite element method, *Int. Jour. Solids Struct.* **32**(1), 27-62.
- [28] Ghosh, S. and Moorthy, S., (1998). Particle fracture simulation in non-uniform microstructures of metal-matrix composites, *Acta Mater.* **46**(3), 965-982.



- [29] Hill, R., (1965). A self consistent mechanics of composite materials, *Jour. Mech. Phys. Solids* **13**, 213-222.
- [30] Suquet, P., (1987). Elements of homogenization theory for inelastic solid mechanics, *Homogenization Technique for Composite Media*, Sanchez-Palencia, E. and Zaoui, A. (eds.), Springer-Verlag, Berlin-Heidelberg-New York, 194-275.
- [31] Lee, K. , Moorthy, S. and Ghosh, S., (1999). Multiple scale computational model for damage in composite materials, *Comp. Meth. Appl. Mech. and Engng.* **172**, 175-201.
- [32] Sun, C. T. and Chen, J. L., (1991). A micromechanical model for plastic behavior of fibrous composites, *Comp. Sci. Tech.* **40** 115-129.
- [33] Xie, M. and Adams, D., (1995). A plasticity model for unidirectional composite materials and its applications in modeling composite testing, *Comp. Sci. and Tech.* **54**, 11-21.
- [34] Bao, G., Hutchinson, J. W. and McMeeking, R. M., (1991). Plastic reinforcement of ductile matrices against plastic flow and creep, *Acta Metallur. et Mater.* **39**.
- [35] Gurson, A.L., (1977). Continuum theory of ductile rupture by void nucleation and Growth-I, Yield criteria and flow rules for porous ductile media, *J. Engng. Mater. Technol.* **99**, 2-15.
- [36] Tvergaard, V., (1982). On localization in ductile materials containing spherical voids *Int. Jour. of Frac.* **18**(4) 237-251.
- [37] Terada, K. and Kikuchi, N., (1995). Nonlinear homogenization method for practical applications, *Computational Methods in Micromechanics*, ed. Ghosh, S. and Ostoja-Starzewski, M., ASME AMD **212**, 1-16.
- [38] Dvorak, G.J. and Benveniste, Y., (1992). On transformation strains and uniform fields in multiphase elastic media, *Proc. R. Soc. Lond.*, A **437**, 291-310.
- [39] Hill, R., (1971). *The mathematical theory of plasticity*, Oxford Press.
- [40] Zhu, J. Z. and Zienkiewicz, O. C., (1988). Adaptive techniques in the finite element method, *Comm. Appl. Num. Meth.* **4**, 197-204.
- [41] Melosh, R. J. and Marcal, P. V., (1977). An energy basis for mesh refinement of structural continua, *Int. J. Num. Methods Eng.* **11**(7), 1083-1092.
- [42] Demkowicz, L. , Devloo, Ph. and Oden, J. T., (1985). On an h type mesh refinement strategy based on a minimization of interpolation error, *Comp. Meth. in Appl. Mech. Engng.* **3** , 67-89.

## Chapter 5

# Experimental-Computational Investigation Of Damage Evolution In Discontinuously Reinforced Aluminum Matrix Composite

### 5.1 Introduction

The commercial use of particle-reinforced metal matrix composites in automotive, aerospace and other engineering systems has increased in the last few decades due to their potentially superior mechanical properties, as well as their ability to reduce life-cycle costs through enhanced thermal stability and weight reduction. The property advantages of these materials are, however, often diminished by general degradation of failure properties like ductility and fracture toughness. Various experimental and numerical studies [1, 2, 3, 4, 5, 6, 7, 8, 9, 10] have been conducted to understand the influence of morphological factors such as volume fraction, size, shape and spatial distribution as well as constituent material and interface properties on the deformation and damage behavior. These studies have concluded that failure mechanisms are highly sensitive to local reinforcement distribution, morphology, size, interfacial strength etc.

Traditionally *unit cell* models [11, 12, 13, 14, 15] based on the finite element analysis have been used to predict the onset and growth of evolving damage in composite materials. While these models provide valuable insights into the microstructural damage processes, simple morphologies idealize actual microstructures for many engineering materials that bear little relationship to the actual stereographic features. These deficiencies have been circumvented in [16, 8, 17], where computational models of discontinuously reinforced materials with random spatial dispersion have been considered. Richmond and coworkers [18, 19] have investigated the effect of morphology on damage in composite, porous and polycrystalline materials by modeling actual geometries obtained from 2D micrographs. Using the Voronoi Cell finite element model, Ghosh et. al. [9, 10] have examined the effect of various spatial dispersions and particle shape and size on the damage initiation and evolution process in ductile matrix composites.

Many characterization studies with 2-D microstructures e.g. [20, 21, 22, 23] have also been conducted to understand the relation between microstructural morphology and damage. Experi-

mental research [25, 26, 27, 28, 29] has however pointed to the necessity of examining the full 3D characteristics for understanding the damage process. These studies infer that 2-D assessment can sometimes be misleading, especially in the presence of spatial clustering. Non-destructive evaluation methods, e.g. techniques based on ultrasonics e.g. [30], acoustic emission [4] and X-ray based computer tomography (CT) [31, 32] have emerged as potential methods for studying 3D damage. However many of these systems are thus far not capable of achieving spatial resolutions required to accurately capture microscopic particles and damage in the particle reinforced MMC's. Buffiere et. al [33] are developing a CT technology to yield tomographic images with a higher spatial resolution.

This work deals with a combined experimental-computational approach to study the evolution of microscopic damage to cause complete material failure in commercial SiC particle reinforced aluminum alloys or DRA's. Through a combination of 2D and 3D characterization and analysis models, it is intended to understand what aspects of microstructural morphology that are most critical for damage nucleation and evolution. Since it is difficult to identify the microcrack growth process once a material has failed completely, an interrupted testing technique is designed. Subsequently, sample microstructures in the severely necked region are microscopically examined in 3D using a serial sectioning method discussed in [24, 25, 26]. Computer simulated equivalent microstructures are tessellated into meshes of 2-D and 3-D Voronoi cells. Various characterization functions of geometric parameters are generated and a sensitivity analysis is conducted to explore the influence of morphological parameters on damage. 2D characterization functions are compared with 3D to evaluate the effectiveness of modeling the 2D micrographs. Modeling of the initiation and propagation of damage is conducted with Voronoi Cell Finite Element Method (VCFEM) [9, 10, 34, 35]. Each Voronoi cell element may consist of a matrix phase, an inclusion phase and a crack phase. Damage initiation by particle cracking is assumed to follow a maximum principal stress based Rankine criterion. The VCFEM for particle cracking has shown a significant promise in modeling large aggregates of heterogeneities. While the appropriateness of 3D analyses is recognized for this study, the 3D VCFEM (under development) does not currently have all necessary features. Due to enormous computing requirements of conventional 3D FEM models, various studies have resorted to simplified manifestations of complex geometries and properties e.g. [7, 41, 15]. This study is restricted to 2D in the form of VCFEM analyses of section micrographs. Finally, the effect of size and characteristic lengths of representative material element (RME) on the extent of damage in the model systems is also investigated.

## 5.2 Experiments for Damage Assessment

### 5.2.1 Interrupted tests

The material analyzed in this work is a discretely reinforced commercial aluminum that is fabricated by a powder metallurgy process [36]. It consists of extruded commercial X2080 aluminum alloy with 15% volume fraction SiC particles. The X2080 matrix has a nominal alloy composition with weight percentages of 3.8% Cu, 1.8% Mg and 0.2% Zr, in addition to low impurity contents of Fe and Si. The precipitation hardened X2080 aluminum alloy system is naturally aged by heat treating for 4 hours at 930°F, followed by cold water quench and aging for 2 days at room temperature.

An important object in this failure study is to obtain adequate microstructural data that depict the growth of damage into a major failure path. In general, it is difficult to identify the dominant damage mechanisms and also the microcrack growth process, once a material has fractured

completely. Thus an interrupted testing technique is designed where the load and deformation are halted in the material instability zone, following necking but prior to fracture. The tests assume that the major cracks are essentially prominent in this stage, and are helpful in understanding the linkage mechanism of microcracks or particle debonds to facilitate growth of the dominant damage. To initialize the testing, estimates of the necking and fracture strains are first obtained by observing the behavior of a tension test to failure. The uniaxial tension tests are executed on a MTS 810 material system with a HP 7044 X-Y recorder to monitor the loads and strains, and the critical strains are measured with a MTS 632.11 strain gauge extensometer. Following the initialization, strain controlled interrupted tests are carried out, in which the specimens are loaded to the instability region before the load is stopped.

Figure 5.1a shows a typical tension specimen for the naturally aged material. Data for six specimens of this material, viz. t1, t2, t3, t4, t5 and t6 are tabulated in table 1. The specimens t1, t2, t4 and t6 are obtained from the outer annulus region of the stock material while t3 and t5 are from the central core regions. The initialization of the test to study the entire material behavior and estimate the post-instability region is done with specimens t1 and t2. The material load-displacement curve is plotted in figure 5.1b, from which the necking strain is obtained from the peak load value. For the specimen t1, the test is conducted at a strain rate is  $\dot{\epsilon} = 5 \times 10^{-4} \text{sec}^{-1}$  and the necking strain and fracture strain are found to be  $\epsilon_n = 9.15\%$  and  $\epsilon_f = 9.40\%$  respectively. The short instability region in t1 prompts a reduced strain rate  $\dot{\epsilon} = 3 \times 10^{-4} \text{sec}^{-1}$  for specimen t2, for which  $\epsilon_n = 9.05\%$  and  $\epsilon_f = 9.20\%$ .

In table 1,  $\dot{\epsilon}$ ,  $\epsilon_n$  and  $\epsilon_f$  correspond to the strain rate, the necking strain and the interrupted strain respectively. The interrupted strain coincides with the fracture strain in the event that fracture precedes the load stoppage. This is indicated with F or I in the table. Load interruption is only possible for the specimens t3 and t6 due to the extremely short post-instability range of this material in comparison with the resolution of the loading mechanism. The necking strains for the specimens t1, t2, t4 and t6 are in the range of  $9.00\% \sim 9.30\%$ , while those for specimens t3 and t5 are in the  $9.80\% \sim 10.20\%$  range. This difference is possibly due to gradients created by the heat treatment at different locations in the stock material. The core cools slower and more uniformly regions near the surface. This results in the more uniform microstructure and larger necking and fracture strains for specimens (t3 and t5) located near the core of the stock material.

## 5.2.2 Damage examination and microscopic analysis

To examine the dependence of microstructural damage on the local morphology, serial sectioning of sample coupons extracted from the load-interrupted specimens t3 and t6, is invoked. This method, discussed in [24, 25, 26], involves gradual removal of material layers to obtain a series of scanning electron/optical micrographs, representing sections of a microstructure. It is a very effective method for reconstructing 3D microstructures from a series of 2D sections of particulate reinforced composites, requiring a resolution of few microns. Prior to sectioning, locations are selected in figure 5.1a for cutting out the sample coupons. X-rays and acoustic microscopy with a AEROTECH UNIDEX 11 acoustic microscope with a resolution of about  $50 \mu\text{m}$  are used in this process to detect regions that contain major crack paths. Polished surfaces of these extracted samples are then examined by a Nikon optical microscope for major damage sites. For the specimen t3, shorter cracks passing through 2 ~ 3 particles at most are found. However, for the specimen t6, a larger crack passing through 5 ~ 6 particles is identified, and is consequently chosen for

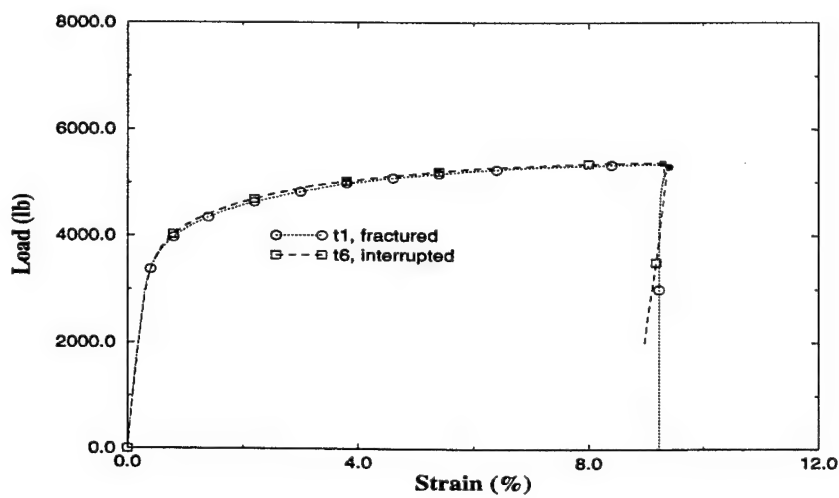
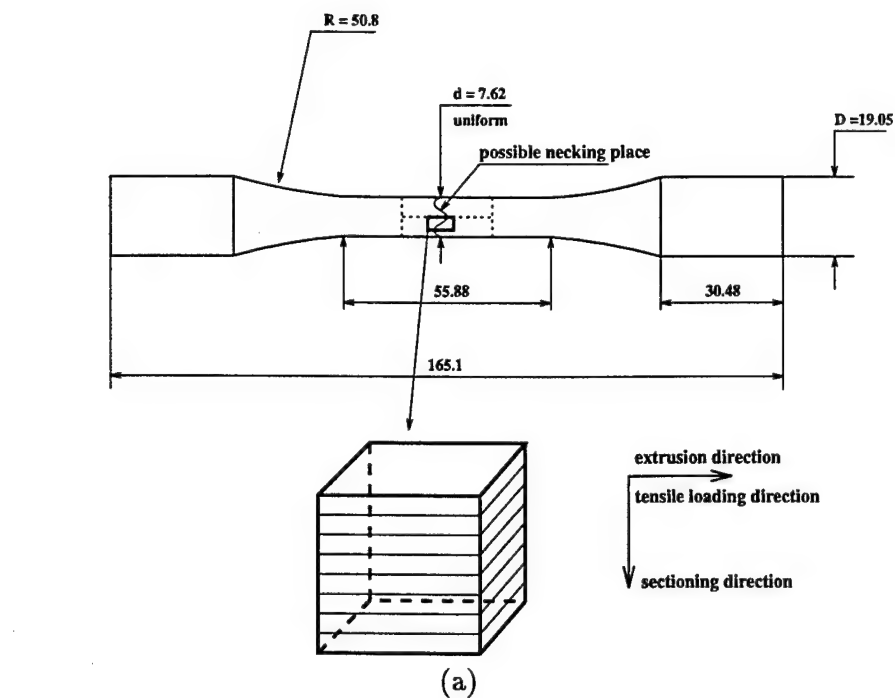


Figure 5.1: (a) Interrupted uniaxial tensile test specimen for naturally aged material and sample coupon for serial sectioning (unit in mm); (b) Load-strain plots for two specimens of naturally aged DRA. Dark points indicate where the loading is interrupted or where the specimen is fractured.

analysis. Coupons of approximate size  $6\text{ mm} \times 6\text{ mm} \times 6\text{ mm}$  are subsequently prepared for the serial sectioning operation to sequentially expose parallel sections of the microstructure. As discussed in [24, 25, 26], parallel layers in a direction perpendicular to the straining direction (see figure 5.1a) are removed using a precision dimple grinder. The depth of material removal per step is selected such that each particle is sectioned at least once, ensuring that all particles of interest are adequately captured in the micrographs. For the DRA considered, the particle size range is approximately  $3\text{--}25\text{ }\mu\text{m}$ , with an average size of  $\sim 9.2\text{ }\mu\text{m}$  and the standard deviation is  $3.891\text{ }\mu\text{m}$ . The section to section step size is chosen to be  $2\text{ }\mu\text{m}$ , corresponding to a total traversed thickness of  $36\text{ }\mu\text{m}$  for 18 sections. Two typical micrographs showing damage are depicted in figures 5.2, for which the horizontal corresponds to the loading direction. The micrographs are then serially stacked using a graphic software [37] to yield 3D microstructures as shown in figure 5.3a. The precise 3D location, shape, size and orientation of each particle can be obtained at a fairly high resolution by this method.

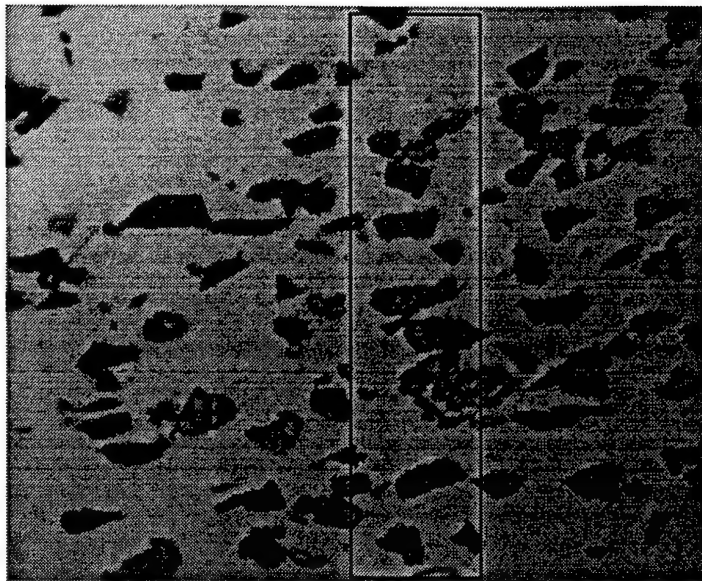
### 5.2.3 Major observations

The micrographs of serial sections 3 and 5 in figure 5.2, perpendicular to the middle plane of the tensile specimen, provide important information on the evolution of the dominant damage path in the material. A dominant damage path is clearly seen in the boxed regions. The damage size progressively diminishes with increasing sections, indicating the end of the cracked particles. The particle area fraction (AF), total number of particles (NP) and total number of cracked particles (NCP) for each section micrograph are presented in table 2. Generally speaking, sections with large AF and NCP are found to contain the larger cracks. The 3D image by assembling 2D micrographs in figure 5.3a also shows the dominant damage path in the boxed region.

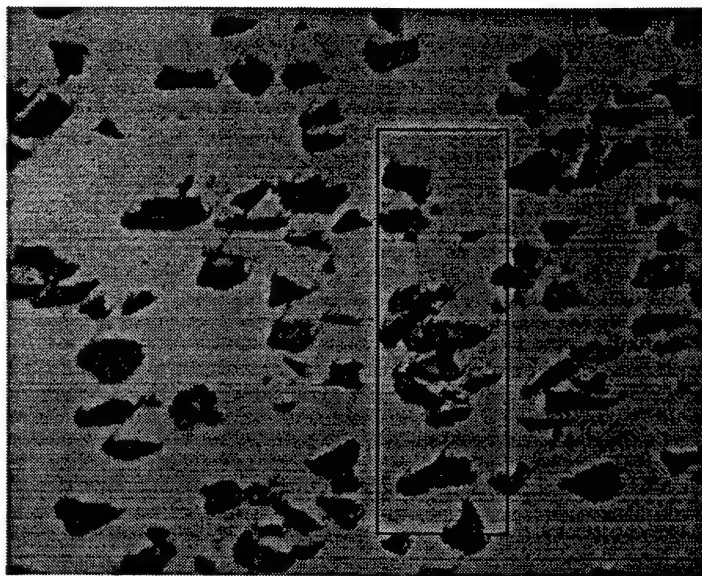
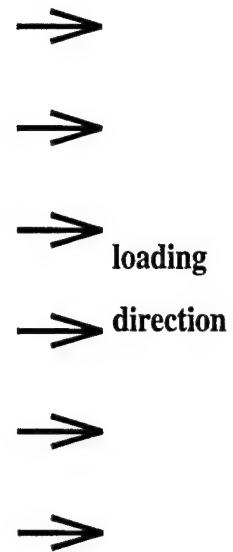
From the microscopic observation results, it is found that for the naturally aged material, the main mode of damage is by particle cracking. Large particles in particle rich regions are more susceptible to cracking than those in particle sparse regions. Microcracks in the particle rich areas link up to form paths of dominant damage. The linkage and evolution of these larger cracks lead to the overall failure of the material. These paths are approximately perpendicular to the tensile loading direction. Thus, spatial distribution of particles plays a more important role in damage than particle size for this material.

## 5.3 Equivalent Microstructure & Mesh Generation

The actual 3D geometry of particles, as seen in figure 5.3a, can be quite complex and an exhaustive database is required to store all geometric details. To avert this, equivalent microstructures that closely approximate the actual morphology but are computationally less demanding, are generated. In this process, each particle and an associated crack are replaced by equivalent ellipses (in 2D) or ellipsoids (in 3D). This method economizes the image analysis and characterization process by way of well known geometric properties. For obtaining equivalent microstructures, digitized image data is first transferred into a binary format to distinguish between the particle, matrix and crack phases. The 0th ( $I_0$ ), 1st ( $I_x, I_y$ ) and 2nd ( $I_{xx}, I_{yy}$ ) order geometric moments are then computed for each particle by adding contributions from each voxel (in 3D) or pixel (in 2D) that lies within the particle boundary. For 2D microstructures the computed moments are equated to the moment formulae



(a)



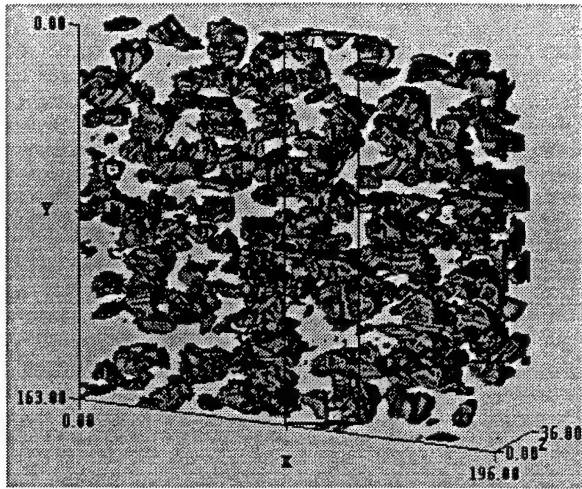
(b)

50  $\mu\text{m}$

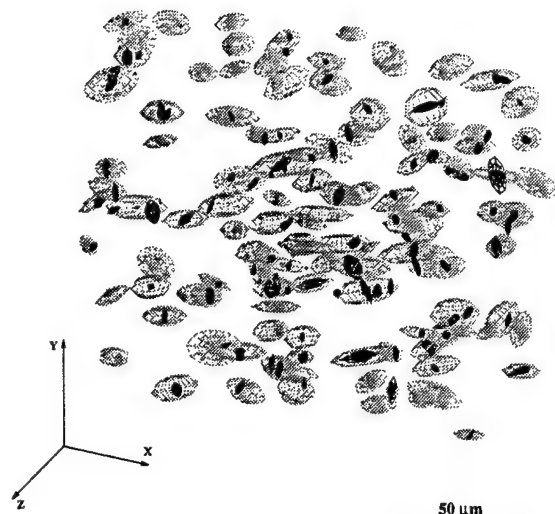


Figure 5.2: Micrographs of different sections of the t6 specimen showing cracked particles; (a) section 3, (b) section 5.

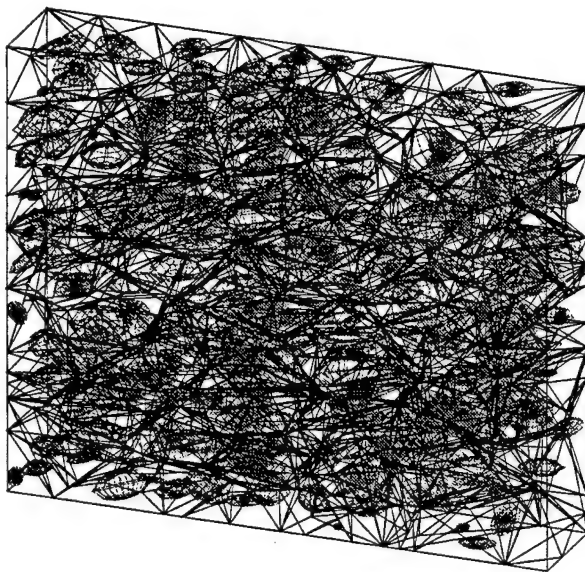




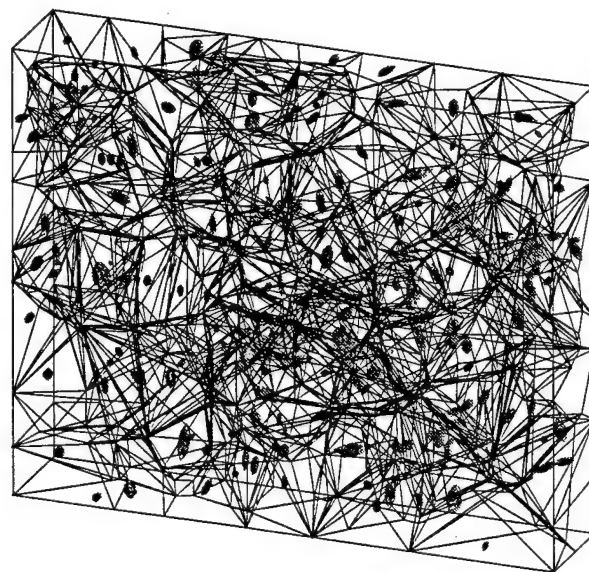
(a)



(b)



(c)



(d)

Figure 5.3: 3D microstructure for SiC particle reinforced DRA after interrupted test (units in  $\mu\text{m}$ ): (a) A computer created image by serially stacking section micrographs, (b) Simulated microstructure of ellipsoidal particles and cracks. Tessellation for 2D and 3D microstructures, (c) 3D tessellation based on particle morphology and (d) 3D tessellation based on microcrack morphology.



for ellipses to evaluate the centroidal coordinates  $(x_c, y_c)$ , half major and minor axis lengths  $(a, b)$ , and orientation  $\theta$  of the major axis from:

$$\begin{aligned} x_c &= \frac{I_y}{I_0}, \quad y_c = \frac{I_x}{I_0}, \quad a = \sqrt{\frac{1}{2}(C_1 + \sqrt{C_1^2 - 4C_2})}, \quad b = \sqrt{\frac{1}{2}(C_1 - \sqrt{C_1^2 - 4C_2})} \\ \theta &= \frac{1}{2} \cos^{-1} \left( \frac{4}{a^2 - b^2} \right) \left( \frac{I_{yy} - I_{xx}}{I_0} - \frac{I_y^2 - I_x^2}{I_0^2} \right) \end{aligned} \quad (5.1)$$

where  $C_1 = 4 * (\frac{I_{xx} + I_{yy}}{I_0} - \frac{I_x^2 + I_y^2}{I_0^2})$  and  $C_2 = \frac{I_0^2}{\pi^2}$ . For 3D microstructures, the centroidal coordinates  $(x_c, y_c, z_c)$  of the equivalent ellipsoid are first evaluated from the 0th and 1st order moments as:  $x_c = \frac{I_y}{I_0}$ ,  $y_c = \frac{I_x}{I_0}$ ,  $z_c = \frac{I_z}{I_0}$ . The principal directions (or orientations of the three axes) for the ellipsoids are obtained from the eigen-values of the 2nd order moments  $I_{ij}$  ( $i = 1..3, j = 1..3$ ). The major (2a), intermediate (2b) and minor (2c) axes of the equivalent ellipsoids are then obtained from the principal moments  $I_1, I_2, I_3$  as:

$$a = \sqrt{\frac{5}{I_0}(I_2 + I_3 - I_1)}, \quad b = \sqrt{\frac{5}{I_0}(I_1 + I_3 - I_2)}, \quad c = \sqrt{\frac{5}{I_0}(I_1 + I_2 - I_3)} \quad (5.2)$$

A simulated 3D microstructure with particles (grey) and cracks (black) is shown in figure 5.3b. The microstructures are then tessellated into a mesh of 2D and 3D Voronoi cells, by surface based algorithms detailed in [25, 26]. In figure 5.3c, the mesh of Voronoi cells is created based on the morphology of particles, while in figure 5.3d the mesh is due to tessellation based on the geometry of particle cracks. Tessellation into a mesh of Voronoi cells plays an important role in developing geometric descriptors for quantitative characterization. They represent regions of immediate influence for each heterogeneity and also define neighbor of each heterogeneity from individual faces or edges of the Voronoi cells. This facilitates easy evaluation of parameters like local area fractions, near neighbor and nearest neighbor distances and orientations.

## 5.4 Microstructure and Damage Characterization

The morphology of particles and associated damage or microcracks can be characterized by various functions of size, shape, orientation and spatial distribution. A number of these classifier functions have been used by the authors and others in [24, 25, 26, 34, 35, 20, 21, 22, 6] to characterize various aspects of microstructural morphology. In this section, some of these functions are considered for the 3D microstructure and 2D micrographs to investigate the relation between morphological characteristics and the path of dominant damage in the material. The specimen t6 with a large microcrack is considered for this study.

In the first exercise, a sensitivity analysis is done with the simulated 3D microstructure in figure 5.3b to reveal the dependence of damage on microstructural variables. Two damage parameters, viz. the number fraction of cracked particles (**nf**) and the volume fraction of cracked particles (**vf**) are chosen to manifest the damage level in the DRA. Six microstructural parameters are considered, viz. (i) particle equivalent size (diameter); (ii) nearest neighbor distance computed as the distance between particles that share a common Voronoi cell edge; (iii) local volume fraction measured as a ratio of the particle size to that of the associated Voronoi cell; (iv) particle shape or ellipsoid aspect ratio; (v) nearest neighbor orientation, measured as the angle between a line joining the

centers of particle and its nearest neighbor, and the loading direction; and (vi) particle orientation with respect to the loading direction. The cracked particle fractions are plotted as functions of these parameters in figure 5.5. A linear interpolation, obtained by a least square fit, yields the corresponding overall gradient or slope.

While both the **nf** and **vf** plots coincide for the particle size plot (i), large differences are noted for nearest neighbor distances (ii) and aspect ratios (iv). Largest slopes of these plots are observed with particle size, nearest neighbor distance and local volume fraction. This infers that the strongest influence on particle cracking comes from the size and local spatial distribution. Particle shape has a relatively smaller effect on damage initiation. Sensitivity of damage to particle orientation and nearest neighbor orientation is found to be minimal for this material.

The characteristics of particles forming the dominant damage path (within the marked box in 5.3a) are compared with those for all cracked particles in the histograms of figure 5.6. The dotted lines correspond to all cracked particles while the shaded areas are for cracked particles in the dominant damage region only. The histograms are with respect to three variables that are found to play important roles in the damage process, viz. the particle size, nearest neighbor distance and orientation with respect to the loading direction. While the range of sizes for all cracked particles is  $4 \sim 13\mu\text{m}$ , that for the particles forming the dominant damage path is  $5.7 \sim 13\mu\text{m}$ . This reveals that larger particles generally contribute to dominant damage path. The plot for nearest neighbor clearly exhibits the influence of particle rich areas (clustering or alignment) on the preferential growth of damage. The nearest neighbor distance for particles in the dominant damage path are in the range  $0.4 \sim 3.7\mu\text{m}$  when compared with the range  $0.4 \sim 12.3\mu\text{m}$  for all cracked particles. The histogram of cracked particles as a function of the orientation with respect to the loading direction reveals that particles with major axis along the loading direction ( $0^\circ$  and  $180^\circ$ ) are generally susceptible to cracking. This is much more pervasive for particles in the dominant damage path, due to the smaller cross-sectional areas normal to loading. In conclusion, particles in the dominant damage path generally have larger size, are in particle rich areas, and are oriented in loading direction.

Finally, it is of interest to identify discriminating characteristics of 2D micrographs that may be helpful in making dominant damage predictions for the actual 3D microstructures. Two representative micrographs, viz. section 1 which *contains a dominant damage* and section 14 *without any dominant damage*, but only scattered particle cracks are compared with the 3D microregion. Four important characterization functions viz. (a) the probability density function of particle equivalent size (diameter), (b) the probability density function of the nearest neighbor distance, (c) the probability density function of the local area/volume fraction and (d) a transformation function  $L(r)$  of a second order intensity function  $K(r)$ , are plotted in figure 5.7 for 2D and 3D micrographs. The second order intensity function  $K(r)$  and its transformed functions ( $L(r) = (\frac{K(r)}{\pi})^{\frac{1}{2}}$  in 2D, and  $L(r) = (\frac{3}{4\pi}K(r))^{\frac{1}{3}}$  in 3D) capture second order statistics of spatial distributions are used as a graphical tool for detecting departures from a homogeneous Poisson process [34, 35, 25, 26]. The plot of  $L(r)$  vs.  $r$  is a  $45^\circ$  straight line for a pure Poisson distribution.

The plots distinctly reveal a few important features of the micrographs. The particle size distribution for the two 2D micrographs are similar and the tails are significantly shorter than 3D. As is expected, 3D particle sizes are larger than 2D particle section sizes due to sectioning along non-principal planes. However the probabilities of both the nearest neighbor distances and local area fractions in figures 5.7b and c yield a distinguishing characteristic. The micrograph with dominant damage has peaks and valleys, as well as tails that are very similar to that for 3D. The

peaks which reflect particle rich regions and the tails which reflect sparse areas are both found to be important discriminants. Deviation from the  $L(r) = r$  function or the  $45^\circ$  line represents a bias towards clustering. The section with the dominant damage has a larger deviation from the random distribution in comparison with the section without major cracking, and is closer to the 3D response. In summary, it may be concluded that when analyzing 2D sections, the likelihood of better representation of dominant damage are for those sections that have higher peaks at lower near neighbor distances with longer tails and have higher deviation from the Poisson distribution. Similar observations have also been made in [5, 1, 38, 29].

## 5.5 Damage Simulation by Voronoi Cell FEM

Two dimensional plane strain/stress simulations of the microstructural damage evolution is conducted by the Voronoi cell finite element model (VCFEM) described in [9, 10, 34, 35]. The current 2D VCFEM only accommodates particle cracking, and hence matrix cracking is ignored in the simulations. The simulations are useful in understanding the damage evolution process by a sequence of particle cracking. Rectangular  $195\mu m \times 155.018\mu m$  micrographs as shown in figure 5.9a,b are analyzed with monotonically increasing strains. Periodicity boundary conditions are imposed by requiring edges to remain straight and parallel to the original direction throughout deformation as:

$$\begin{aligned} u_x &= 0 \text{ (on } x = 0 \text{)}, u_y = 0 \text{ (on } y = 0 \text{)}, u_x = u_{ap} \text{ (on } x = L_x \text{)}, u_y = D_y^* \text{ (on } y = L_y \text{)} \\ T_y &= 0 \text{ (on } x = 0/L_x \text{)}, T_x = 0 \text{ (on } y = 0/L_y \text{)} \end{aligned} \quad (5.3)$$

where  $u_{ap}$  is an applied displacement and  $D_y^*$  is determined from the average force condition  $\int_X T_x dx = 0$  on  $y = L_y$ . The reinforcing phase of SiC particles are assumed to be brittle and is modeled with the linear elastic properties: Young's modulus  $E = 427$  GPa, Poisson's ratio  $\nu = 0.17$ . The aluminum matrix material is assumed to be ductile and is modeled by small deformation isotropic hardening  $J_2$  elasto-plasticity theory with properties: Young's modulus  $E = 72$  GPa, Poisson's ratio  $\nu = 0.33$  and the post yield elastic-plastic behavior is obtained from [39] as shown in figure 5.8. Microstructural damage by particle cracking is assumed to be governed by a maximum principal stress or Rankine criterion. In this criterion, a crack is initiated when the maximum principal stress in tension exceeds a critical fracture stress  $\sigma_{cr}$  at a point. The crack is oriented at right angle to the principal stress direction. The critical stress  $\sigma_{cr}$  is also influenced by the particle size due to the existence of microcracks. To account for the size effect in  $\sigma_{cr}$ , a Weibull distribution based criterion is used, where the probability of particle fracture  $P_f(A, \sigma)$  is related to the particle volume/area  $v$  and the maximum principal stress  $\sigma_I$  as:

$$P_f(v, \sigma_I) = 1 - \exp[-v(\frac{\sigma_I}{\sigma_0})^m] \quad (5.4)$$

where  $\sigma_0$  and  $m$  are two material parameters in the Weibull distribution that are calibrated from experiments.

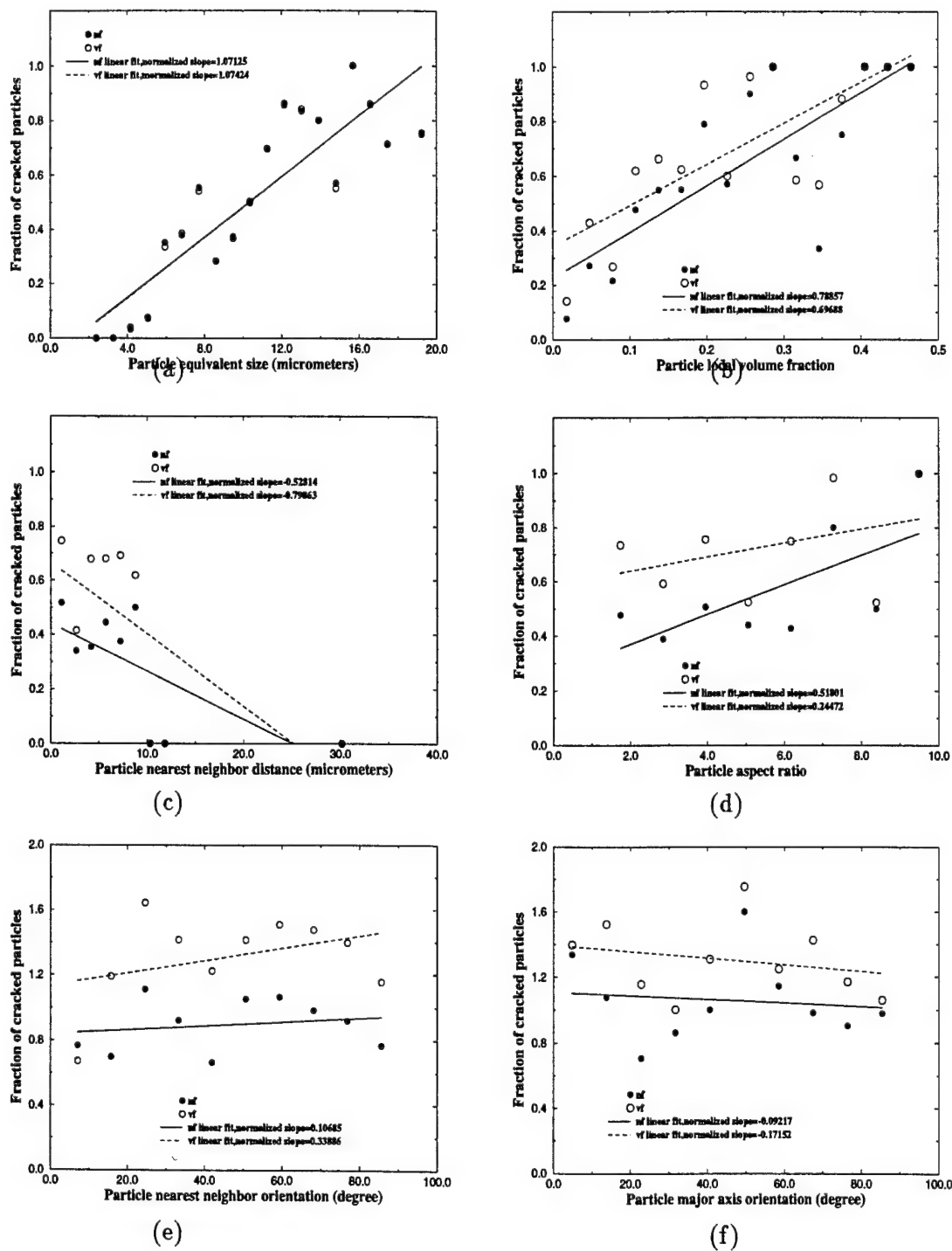


Figure 5.4: Sensitivity of damage to various microstructural variables

### 5.5.1 Calibration of Weibull parameters $\sigma_0$ and $m$

In the two parameter Weibull model, the fraction of fractured particles may be obtained (see [41, 42, 26]) from a known probability distribution of particle volumes  $p(v)$ , as:

$$\rho(v) = \int_{V_{min}}^{V_{max}} p(v) P_f(v, \sigma_I) dv \approx \sum_{i=1}^N p(v_i) (1 - \exp[-\frac{v_i}{v_0} (\frac{\sigma_I}{\sigma_0})^m]) \Delta v_i \quad (5.5)$$

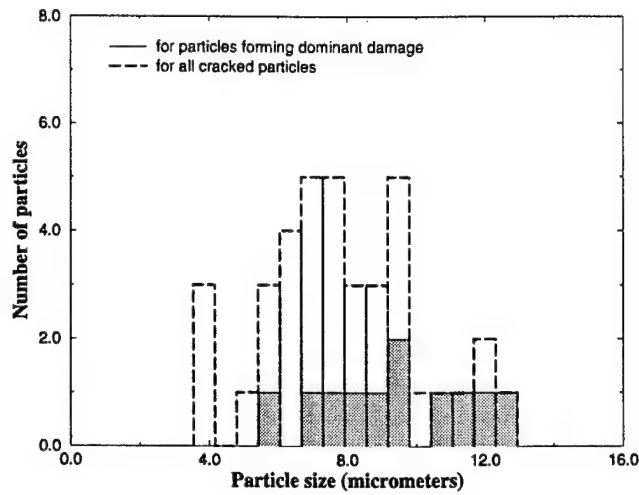
where  $p(v_i)$  is the probability density distribution of particle volume/area  $v_i$ . The entire area is divided into  $N$  intervals such that  $\Delta v_i = v_i - v_{i-1}$ ,  $\sigma_I^i$  is the average particle maximum principal stress for particles with size in the range of  $[v_{i-1}, v_i]$  and  $v_0$  is a reference area taken to be the average area. The fraction of cracked particles  $\rho$  is readily obtained from the experimental micrographs. Again, the section micrographs 2, 8 and 14 are used to calibrate the Weibull parameters. The fractions of cracked particles and the average particle area for these three sections are 31.78%, 24.76%, 28.57% and 53.43, 48.91 and 52.67  $\mu m^2$  respectively. The maximum principal stress  $\sigma_I^i$  for each particle is obtained from VCFEM simulation prior to the onset of particle cracking at a true strain of  $\epsilon = 8.88\%$ . From the experimental observations it is assumed that no major damage has initiated at this strain. The Weibull parameter  $m$  is assumed to take integer values between 1 and 8 following [42, 26] and the corresponding values of  $\sigma_0$  are given in table 3.

The Weibull parameters are also calibrated using a 3D ABAQUS model simulation of a cubic unit cell with a single, 15% volume fraction, spherical particle as described in [26]. The 1x1x1 unit cell model has a particle of radius  $R = 0.66$ . A modified form of equation 5.5 is used to account for the shape variability of the particles as

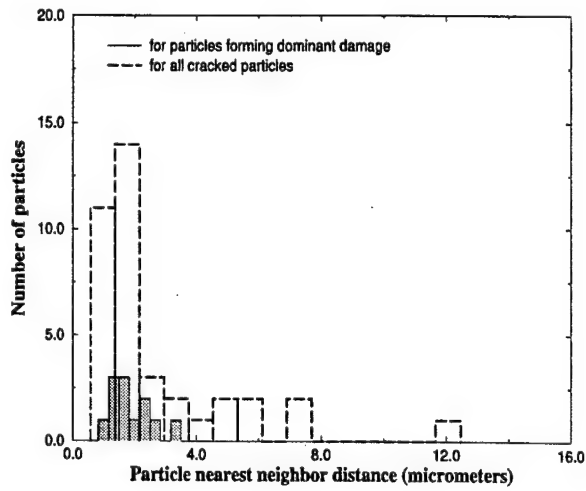
$$\rho(\alpha, v) = \int_{\alpha_{min}}^{\alpha_{max}} \int_{V_{min}}^{V_{max}} p(\alpha) p(v) P_f(v, \sigma_I) dv \quad (5.6)$$

where  $\alpha$  corresponds to the particle aspect ratio. The particle size and shape distribution functions  $p(v)$  and  $p(\alpha)$  are calculated from the computer simulated representation of the actual 3D microstructure shown in figure 5.3. This average particle volume and the fraction of cracked particle are directly computed from figure 5.3 as  $\bar{v} = 642.0 \mu m^3$  and  $\rho = 45.48\%$ . The average particle stress at a macroscopic strain  $\epsilon = 8.88\%$  is obtained from the ABAQUS simulation as  $\sigma_p = 862.60$  MPa. Results of calibration with and without shape effects are documented in table 3. It is found that the best agreement in  $\sigma_0$  for all 2D sections and 3D is obtained for  $m$  between 4 and 5. Consequently the parameter is chosen to be  $m = 4.2$ . The corresponding value of  $\sigma_0$  for section 2 is 3.04 GPa, for section 8 is 3.19 GPa, for section 14 is 2.79 GPa and the average of these sections is  $\sigma_0 = 3.01$  GPa.

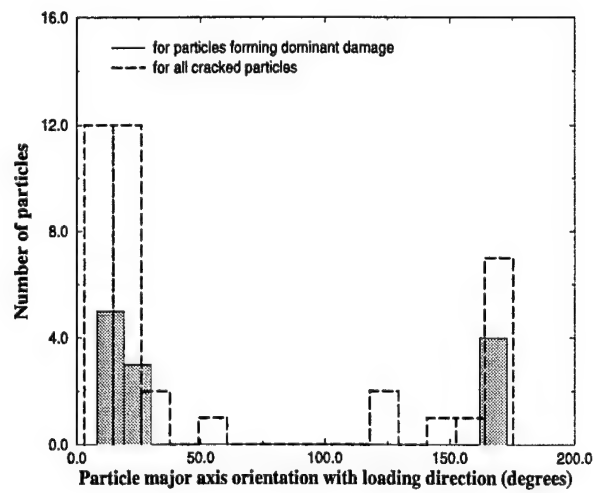
Results of VCFEM analysis of the simulated micrographs of sections 1, 3, 5 and 9 are provided in table 4. The number of cracked particles at a macroscopic strain of 8.88% by VCFEM are compared with experimental results. While the general agreement is quite good, it is seen that the concurrence is particularly favorable when the simulation is conducted with a  $\sigma_0$  that is obtained from a section that is near to the one being analyzed. For example, the results of sections 1 and 3 are very good when  $\sigma_0 = 3.01$  GPa, which is obtained from section 2. This concurrence may be attributed to the similarity in the distribution of heterogeneities in neighboring sections, and suggests that spatial distribution has a strong effect on the Weibull parameters.



(a)

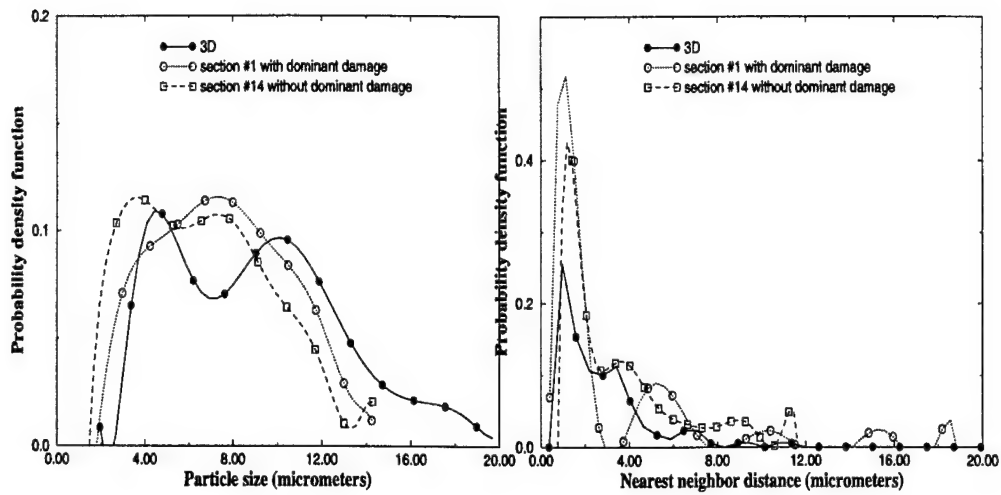


(b)



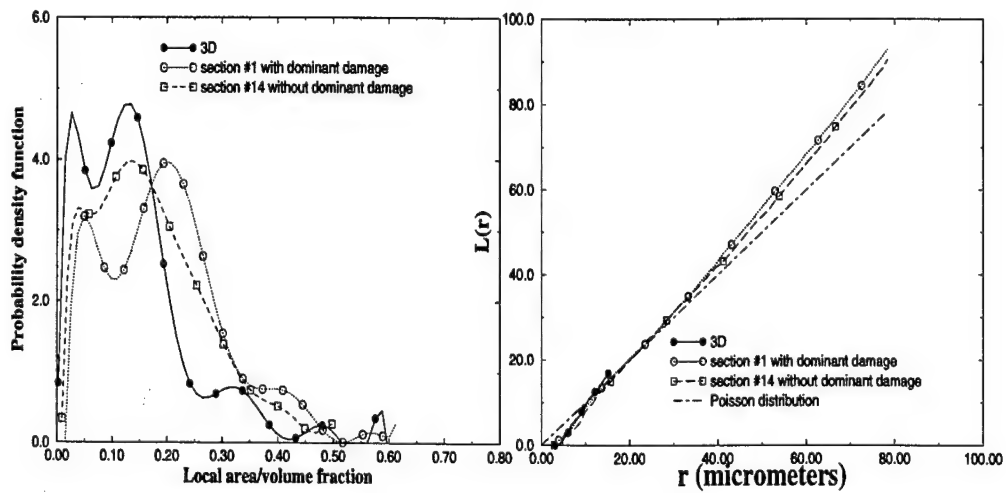
(c)

Figure 5.5: Histograms comparing characteristics of particles with dominant damage with all cracked particles



(a)

(b)



(c)

(d)

Figure 5.6: Characterization functions for 2D sections and 3D microstructure.

## Microscopic Damage Analysis

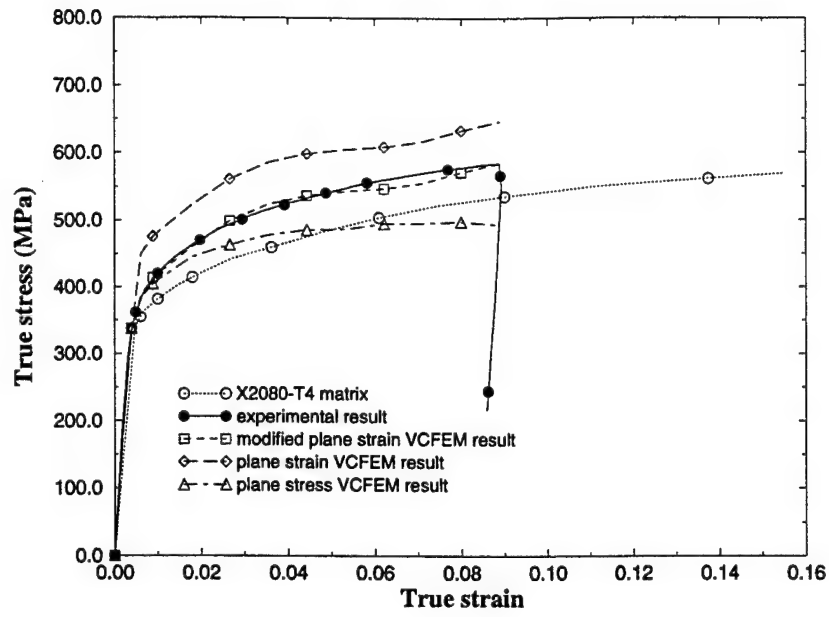
Various results for section 1 which contain a dominant damage path are generated by VCFEM simulation and compared with experimental observations in this section. The macroscopic stress-strain plot for plane strain and plane stress assumptions are compared with experimental results in figure 5.8a. The overall yield strength is better predicted by the plane stress model. However, the post yield behavior with plane strain conditions is much closer to the experimental results. The initial higher yield strength is expected with plane strain due to the plastic constraint caused by the  $\epsilon_z = 0$  condition. A shifted stress-strain plot (modified plane strain VCFEM result in figure 5.8a) where the stresses are reduced by the initial difference in yield stress shows a very good match between experiments and simulation. Thus plane strain assumptions are used in subsequent computations. Figure 5.8b is intended to predict the onset of plastic instability by the model and compare it with actual fracture observed in the experiments. The use of the Considere criterion to predict the onset of plastic instability has been suggested by Llorca [2, 41] in the absence of dilatational strain associated with reinforcement fracture. In this criterion, the average stress  $\bar{\sigma}$  is related to the strain hardening rate  $\frac{d\bar{\sigma}}{d\epsilon}$  as

$$\bar{\sigma} = \frac{d\bar{\sigma}}{d\epsilon} \quad (5.7)$$

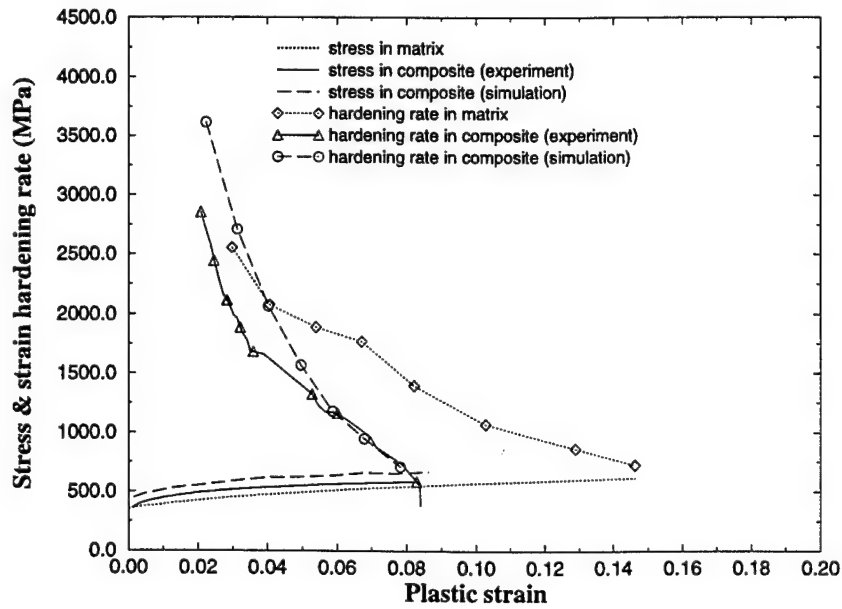
The strain derived from this relation corresponds to the lower bound of the tensile ductility since it controls the composite load bearing capacity. Three sets of curves are plotted in the figure 5.8b corresponding to the matrix material, the VCFEM results in plane strain and the experimental results. It is seen that the Considere criterion (junction of the two curves) predicts the experimental point corresponding to the onset of fracture rather well. Additionally the 2D prediction of the plane strain simulation is also quite good and can be used with reasonable confidence.

Microstructural results of the simulation are compared with experiments in figure 5.9. The computed micrograph with evolved damage for section 1 is compared with the experimental micrograph at 8.88% strain in figure 5.9a and b. The damaged particles are shown with the contained crack. Most damaged particles in the simulation coincide with the experimental results, with the box indicating the dominant damage path. The damage path is approximately perpendicular to the tensile loading direction. Figure 5.9b also shows the contour plot of effective plastic strain in the ductile matrix and indicates the path of damage linkage. The plastic strain is higher and localized between cracked particles and this is expected to cause matrix cracking. The number fraction of cracked particles in different size ranges are plotted in figure 5.9c. Very good agreement is seen between simulation and experimental results. Figure 5.9d is a contour plot of the particle fracture probability at 8.88% strain. The black shade corresponds to the highest probability and fractured particles are illustrated in white with a crack. Similar plots (not shown) at earlier stages of deformation show that several particles with higher probability at the smaller strain have cracked with deformation. The number fraction of cracked particles as a function of straining are plotted for sections 1, 5 and 9 together with the experimental observation in figure 5.10. At lower strains the number fraction of cracked particles for sections 1 and 5 with particle rich regions are higher than that for section 9. This is due to higher stress concentrations particle rich areas that are enough to fracture some particles even at low strains. With increasing strains more particles start to crack in the section 9 and exceeds that for section 5 which has less particles in the clustered regions. The 2D simulations however exhibit less cracked particles than that in the actual 3D microstructure.





(a)



(b)

Figure 5.7: (a) Macroscopic stress-strain response by plane strain and plane stress VCFEM simulation, (b) Stress-strain hardening rate plots for the Considere condition.

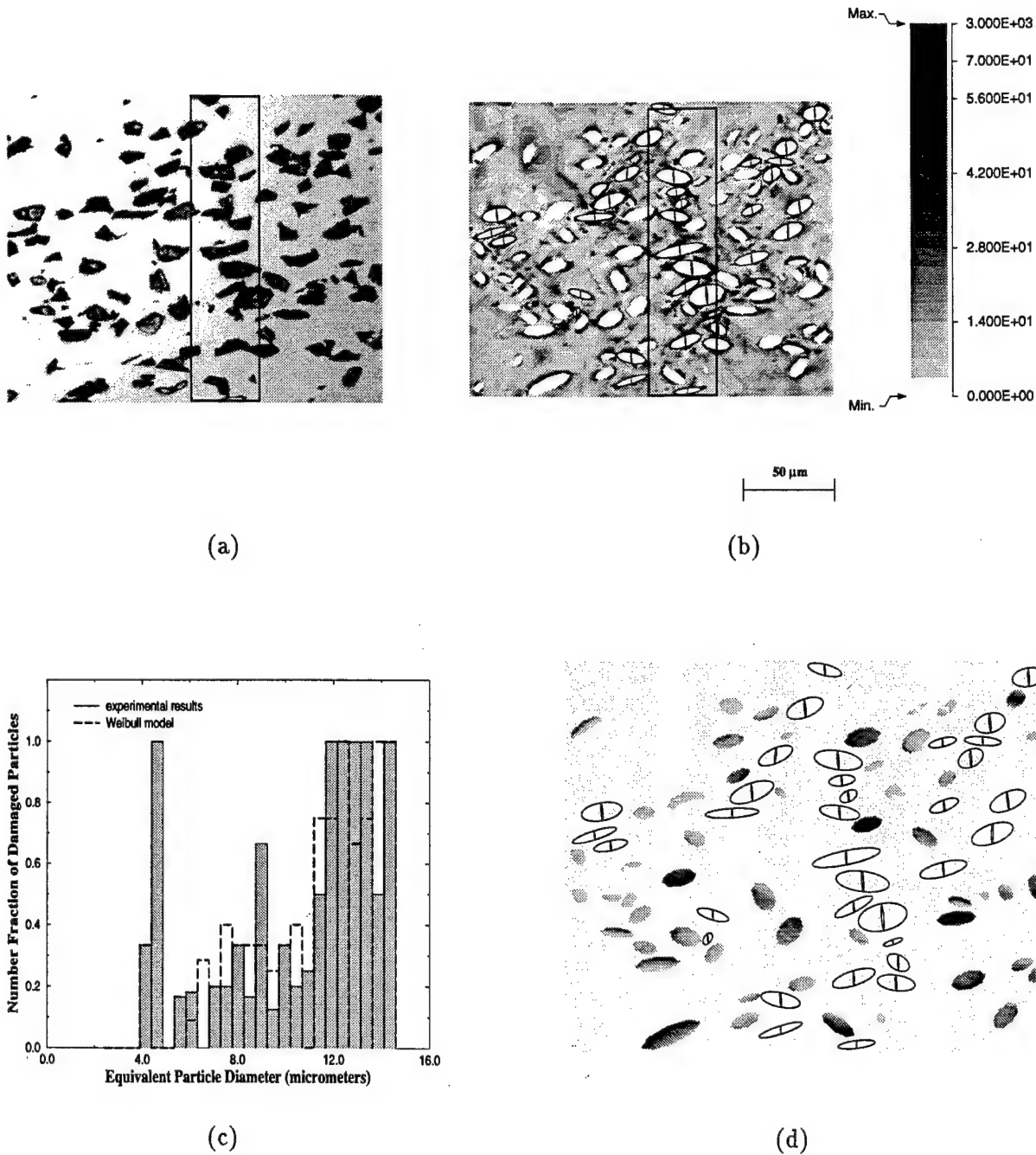


Figure 5.8: (a) Experimental micrographs, (b) VCFEM simulated micrograph showing damage and contour plot of effective plastic strain at 8.88% strain in section 1, (c) histogram of number fraction of cracked particles as a function of particle size by Weibull based probabilistic criterion, and (d) contour plot of particle fracture probability of section 1 at 8.88% strain.

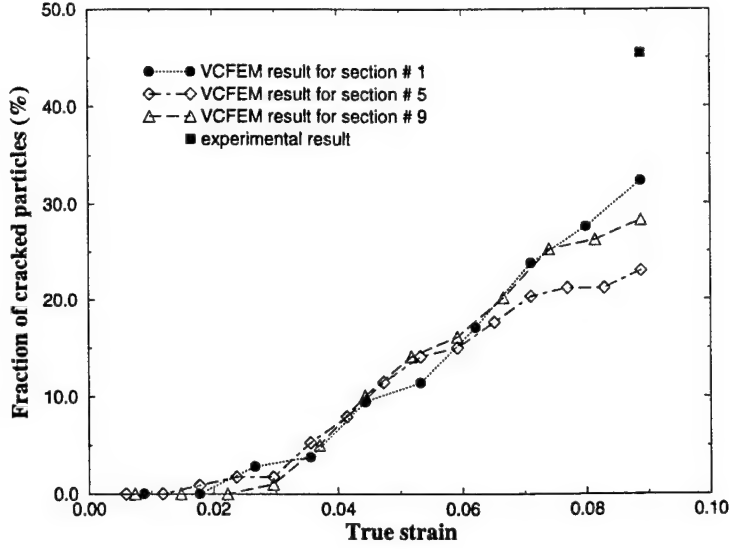


Figure 5.9: Number fraction of cracked particles as a function of straining.

## 5.6 Characteristic Size of Microstructures

The influence region of local morphology on the mechanical response is characterized by a microstructural representative material element (RME) that is critical in delineating length scales. The RME depicts a region which is assumed to be representative of the entire microstructure. Functions that distinguish between variations in stress/strain distributions for local disturbances in microstructural patterns can provide important insight on microstructure-property relations. Marked correlation functions, discussed in [22, 10, 35, 26] for multivariate characterization of patterns, are evaluated to characterize length scales or RME size in the presence of damage. A mark may be identified with an appropriate microstructural variables, e.g. in this case a variable that related to quantification of damage. The marked correlation function for a heterogeneous domain  $W$  of volume  $V$  containing  $N$  heterogeneities is mathematically expressed as [22, 23, 10]:

$$M(r) = \frac{[\frac{dH(r)}{dr}]/(4\pi r^2)}{g(r)}; \quad H(r) = \frac{1}{m^2} \frac{V}{N^2} \sum_{i=1}^N \sum_{k=1}^{k^i} m_i m_k(r) \quad \text{and} \quad g(r) = \frac{1}{4\pi r^2} \frac{dK(r)}{dr} \quad (5.8)$$

where  $K(r)$  is the second order intensity function defined in [34, 35],  $g(r)$  is the pair distribution function and  $H(r)$  is the mark intensity function. The  $H(r)$  function reduces to the  $K(r)$  function if all heterogeneities have the same mark. A mark associated with the  $i^{th}$  heterogeneity is denoted as  $m_i$ ,  $k^i$  is the number of heterogeneities which have their centers within a sphere of radius  $r$  around  $i^{th}$  heterogeneity, for which the mark is  $m_k$ , and  $m$  is the mean of all marks. By definition  $M(r)$  establishes a relation between the location and associated variables for heterogeneities. Two marks are considered in this study. The first corresponds to particle cracks and are designated as  $m_i = 1$  for a cracked particle and  $m_i = 2$  for an intact particle. The second corresponds to the probability of particle fracture, which signifies the propensity to advance the microstructural damage state.

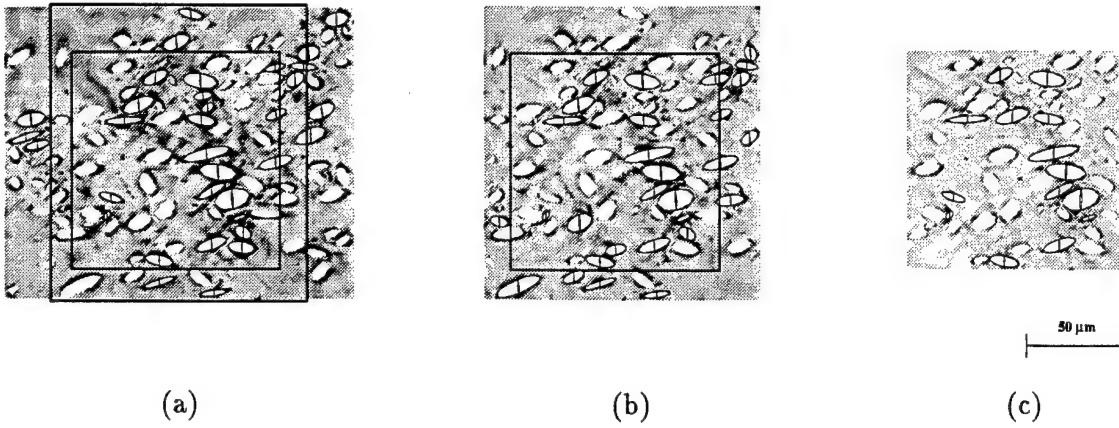


Figure 5.10: Simulations showing effective plastic strain(%) and cracked particles in three different subsets of the entire micrograph of section 1, (a) RME 0 with dimension  $195\mu\text{m} \times 155\mu\text{m}$  (b) RME 1 with dimension  $150\mu\text{m} \times 155\mu\text{m}$  and (c) RME 2 with dimension  $116\mu\text{m} \times 115\mu\text{m}$ .

The  $M(r)$  function statistically stabilizes at near-unit values at a distance  $r_{inter}$  at which the local morphology ceases to have any significant influence on evolving variable. Values of  $M(r) > 1$  show positive correlation, while  $M(r) < 1$  indicates repulsion between marks. This distance  $r_{inter}$  is an indication of the physical range of interaction and is significant in making decisions about length scales and the RME size.

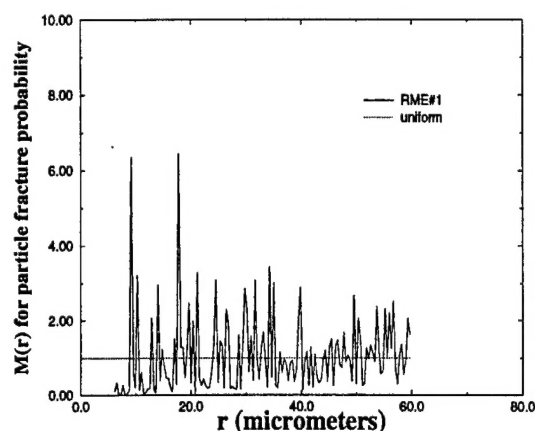
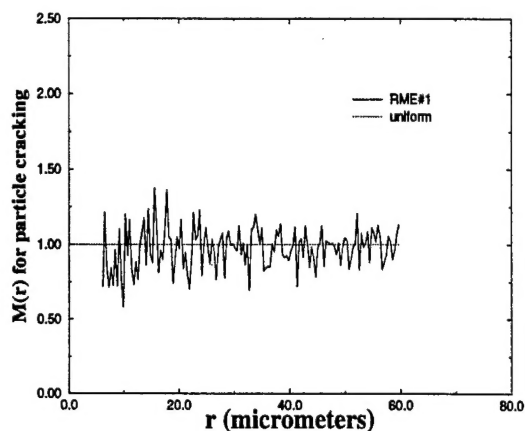
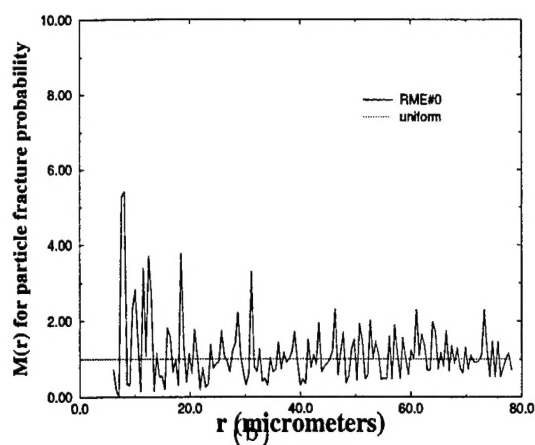
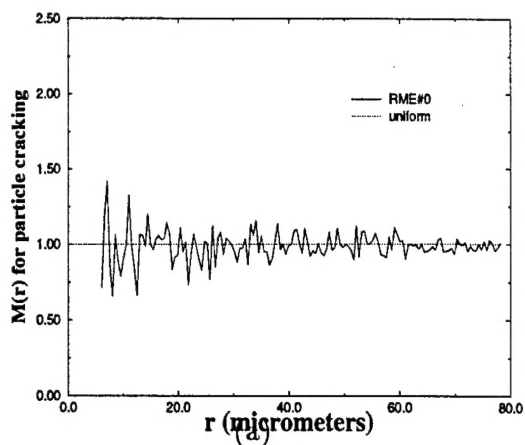
The marked correlation functions corresponding to cracked particles and probability of fracture, are plotted in figures ??a and b from the simulation of the entire micrograph of section 1 (termed as RME 0) with dimensions  $195\mu\text{m} \times 155\mu\text{m}$ . The dotted line corresponds to the unit  $M(r)$  for uniform distribution of spherical heterogeneities with identical marks. Contour plots of the equivalent plastic strain in the simulated micrograph with cracked particles are shown in figure 5.11a. The particle area fraction for this micrograph 18.37% and the total number of particles and cracked particles are 105 and 34 respectively. The plots are made with only upto 40% of the entire micrograph, or  $80\mu\text{m}$  to avoid boundary effects in  $M(r)$ . The  $M(r)$  functions in both figures approximately stabilize at near-unit values at a distance  $r_{inter}$  of about  $60\mu\text{m}$ . At this distance, the local morphology is expected to have a significantly reduced influence on the evolving variables. The slower attenuation of  $M(r)$  for particle fracture at shorter range indicates the strong effect of the local morphology on damage evolution. Next, a smaller region (RME 1) is selected for damage simulation corresponding to the stabilized region in the  $M(r)$  plots. Since the stable region is  $60\mu\text{m}$ , the dimension of the micrograph is chosen to be  $150\mu\text{m} \times 155\mu\text{m}$ , incorporating the scaling factor, i.e.  $\frac{60}{.4} = 150$ . This is shown with the box in figure 5.11a. Again the contour plots of plastic strain with cracked particles by VCFEM simulation are shown in figure 5.11b. The dominant crack behavior is quite similar to that for RME 0, even though there is some difference near the boundary. Also the plastic strain contours and limiting values are similar. The particle area fraction for RME 1 is 18.13% with the total number of particles and cracked particles at 84 and 28 respectively. The  $M(r)$  plots in figure ??c and d show that the functions may still be assumed to stabilize at around  $60\mu\text{m}$ . A smaller subset (RME 2), with dimensions  $116\mu\text{m} \times 115\mu\text{m}$  is next simulated and the plastic strain is depicted in figure 5.11c. Significantly different plastic

strains and cracking pattern is observed for this microstructure. The particle area fraction for this micrograph is 18.68% with a total of 51 particles of which 18 are cracked. The plots of  $M(r)$  function do not stabilize in the domain of the simulation window. Through this analysis the size effect of microstructure, needed for adequate representation and analysis in the presence of evolving damage is demonstrated.

## 5.7 Conclusions

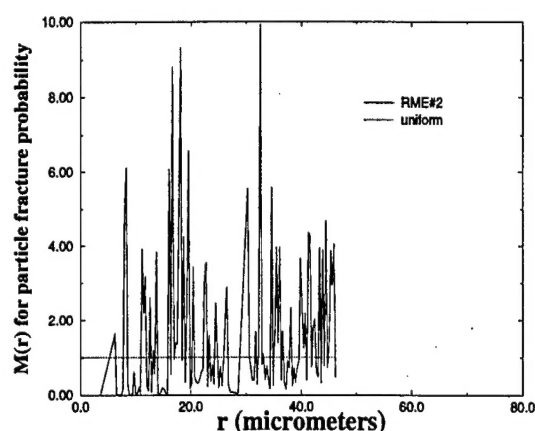
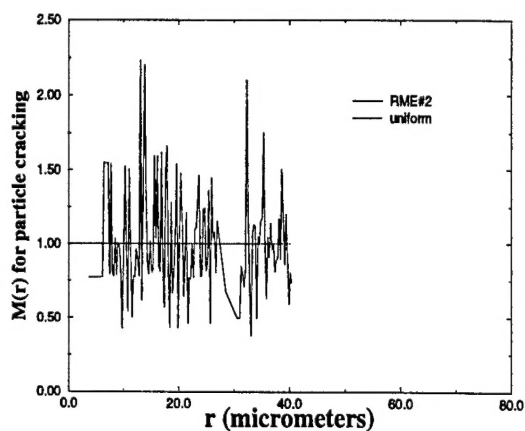
In this work, a combination of experimental and computational methods are utilized to characterize and understand the evolution of microscopic damage that cause failure in naturally aged commercial SiC particle reinforced DRA's. The main mode of damage for the naturally aged material is found to be particle cracking. Larger particles in particle rich regions are more susceptible to cracking than those in particle sparse regions. Spatial distribution of particles plays a more important role in damage than particle size for this material. A sensitivity analysis with respect to microstructural parameters infers that the strongest influence on particle cracking comes from the size and local spatial distribution. Particle shape, orientation and nearest neighbor orientation have relatively smaller effect on damage initiation. Histograms of particles forming the dominant damage path in comparison with all cracked particles reveal that larger particles oriented in loading direction and in relatively rich areas are more susceptible to contribute to a dominant crack in the microstructure. In an attempt to identify discriminating characteristics of 2D micrographs that may be of helpful in making dominant damage predictions for the actual 3D microstructures, probability density functions of particle size nearest neighbor distance, and second order intensity function  $K(r)$  of spatial distribution are plotted. Better representation of damage is possible with those sections that have higher peaks at lower near neighbor distances and longer tails, as well as have propensity towards clustering.

Next the two dimensional Voronoi cell finite element model is used to simulate microstructural damage evolution in computer generated equivalent micrographs. Both macroscopic and microscopic variables obtained by the VCFEM simulation are compared with experimental observations. The macroscopic stress-strain plot for the plane strain analysis is found to yield quite good match with experiments if the difference in the initial yield strength due to plastic constraint is subtracted. Prediction of the onset of plastic instability by the Considere criterion is also found to be in reasonably good agreement with the experimental results. For the microstructural results with number of cracked particles in different size ranges, the Weibull model is found to give better concurrence with experiments. A plot of the number fraction of cracked particles as a function of straining shows that at lower strains sections with particle rich regions damage rapidly, but the rate slows down with additional deformation. Finally, the marked correlation functions are evaluated to characterize length scales and representative material element size in the presence of damage. Particle cracks and the probability of particle fracture are chosen to be the marks. The study reveals that a significantly large portion of the microstructure should be analyzed for reasonable accuracy in the presence of damage. The correlation functions do not stabilize below a certain length scales and this keeps growing with increased damage. In summary, various important characteristics of growing damage are investigated in this work to understand the role of microstructure in the material failure process.



(c)

(d)



(e)

(f)

Figure 5.11: Marked correlation function as a function of radial distance; (a) cracked particles as marks and (b) probability of cracking as mark for RME 0; (c) cracked particles as marks and (d) probability of cracking as mark for RME 1; (e) cracked particles as marks and (f) probability of cracking as mark for RME 2.

# Bibliography

- [1] P.M. Singh and J.J. Lewandowski, *Metall. Trans. A*, **26A**, 2911 (1995).
- [2] J. Llorca and C. Gonzalez, *J.Mech.Phys.Solids*, **46**, 1 (1998).
- [3] A.B. Pandey, B.S. Majumdar and D.B. Miracle, *Processing and Fabrication of Advanced Materials, Proc. of TMS Conf.*, ed. by T.S. Srivatsan and J.J. Moore, 185 (1995).
- [4] P.M. Mummery, B. Derby and C.B. Scruby, *Acta Metall. Mater.*, **41**, 1431 (1993).
- [5] Y. Brechet, J.D. Embury, S. Tao and L. Luo, *Acta Metall. Mater.*, **39**, 1781 (1993).
- [6] W.H. Hunt, *Ph.D Thesis*, Carnegie Mellon University, (1992).
- [7] J. Llorca and M. Elices, *Intrinsic and Extrinsic Fracture Mechanisms in Inorganic Composite Systems*, ed. by J.J. Lewandowski and W.H. Hunt, a publication of the Minerals, Metals & Materials Society, 15 (1995).
- [8] T. Christman, A. Needleman and S. Suresh, *Acta Metall. et Mater.*, **37**, 3029 (1989).
- [9] S. Moorthy and S. Ghosh, *Comp. Meth. Appl. Mech. Eng.*, **151**, 377 (1998).
- [10] S. Ghosh and S. Moorthy, *Acta Metall. et Mater.*, **46**, 965 (1998).
- [11] A. Needleman, *J. Appl. Mech.*, **54**, 525 (1987).
- [12] V. Tvergaard, *Jour. Mech. Phys. Solids*, **41**, 1309 (1991).
- [13] G. Bao, *Acta Metall. et Mater.*, **40**, 2547 (1992).
- [14] C.L. Hom, P.A. Mataga and R. M. McMeeking, *Int. Jour. Numer. Meth. Engrg.*, **27**, 233 (1989).
- [15] M. Finot, Y.-L. Shen, A. Needleman and S. Suresh, *Metall. Mat. Trans. A*, **25A**, 2403 (1994).
- [16] J.R. Brockenbrough, S.Suresh and W.A.Weinecke, *Acta Metall. et Mater.*, **39**, 735 (1991).
- [17] P.E. McHugh, R.J. Asaro and C.F. Shih, *Acta Metall. et Mater.*, **41**, 1461 (1993).
- [18] J.R. Brockenbrough, W.H. Hunt Jr. and O. Richmond, *Scripta Metall.*, **27**, 385 (1992).
- [19] R. Becker and O. Richmond, *Model. Simul. Mater. Sci. Eng.*, **2**, 439 (1994).

- [20] W.A. Spitzig, J.F. Kelly and O. Richmond, *Metallography*, **18**, 235 (1985).
- [21] P.J. Wray, O. Richmond and H.L. Morrison, *Metallography*, **16**, 39 (1983).
- [22] R. Pyrz and B. Bochenek, *Sci. Engrg. Comp. Mat.*, **3**, 95 (1994).
- [23] R. Pyrz, *Mater. Sci. Eng.*, **A177**, 253 (1994).
- [24] M. Li, S. Ghosh, T.N. Rouns, H. Weiland, O. Richmond and W. Hunt, *Mater. Characterization*, **41(2-3)**, 81 (1998).
- [25] M. Li, S. Ghosh, O. Richmond, H. Weiland and T.N. Rouns, Part I, *Mater. Sci. Engin. A*, (in press).
- [26] M. Li, S. Ghosh, O. Richmond, H. Weiland and T.N. Rouns, Part II, *Mater. Sci. Engin. A*, (in press).
- [27] W.H. Hunt, *Intrinsic and extrinsic fracture mechanisms in inorganic composite systems*, ed. by J.J. Lewandowski and W.H. Hunt, A Publication of the Minerals, Metals & Materials Society, **31** (1995).
- [28] J.J. Lewandowski, C. Liu, W.H. Hunt, Jr., *Powder Metallurgy Composites*, ed. by P. Kumar, K.M. Vedula and A.M. Ritter, TMS-AIME, Warrendale, PA, 117 (1987).
- [29] D.J. Lloyd, *Acta Metall. Mater.*, **39**, 59 (1991).
- [30] S.I. Rokhlin, W. Huang and Y.C. Chu, *Ultrasonics*, **33**, 351 (1995).
- [31] P. Potet, C. Bathias and B. Degriigny, *Mater. Eval.*, **46**, 1050 (1988).
- [32] B. London, R.N. Yancey and J.A. Smith, *Mater. Eval.*, **48**, 604 (1990).
- [33] J.-Y. Buffiere, E. Maire, C. Verdu, P. Cloetens, M. Pateyron, G. Peix and J. Baruchel, *Mater. Sci. Eng.*, **A234-236**, 633 (1997).
- [34] S. Ghosh, Z. Nowak and K. Lee, *Acta. Mater.*, **45**, 2215 (1997).
- [35] S. Ghosh, Z. Nowak and K. Lee, *Comp. Sci. & Tech.*, **57**, 1187 (1997).
- [36] W.H. Hunt, Jr., T.M. Osman and J.J. Lewandowski, *J.O.M.*, **45(1)**, 30 (1993).
- [37] *SPYGLASS Slicer, Quick Tour and Reference*, Version 1.0, Spyglass Inc., Champaign, IL 61826 (1994).
- [38] P.M. Singh, J.J. Lewandowski, in: *Intrinsic and Extrinsic Fracture Mechanisms in Inorganic Composite Systems*, ed. by J.J. Lewandowski and W.H. Hunt, a publication of the minerals, metals & materials Society, 1995, pp.57.
- [39] W.H. Hunt, C.R. Cook and R.R. Sawtell, *SAE paper*, 910834 (1991).
- [40] C.W. Nan and D.R. Clarke, *Acta Mater.*, **44**, 3801 (1996).
- [41] C. Gonzalez and J. Llorca, *Scripta Materialia*, **35**, 91 (1996).
- [42] J. Llorca, *Acta metall. mater.*, **43**, 181 (1995).



## Chapter 6

# List of Participating Scientific Personnel

1. **Dr. Somnath Ghosh**, Principal Investigator,  
Associate professor of Applied Mechanics, The Ohio State University.
2. **Dr. Suresh Moorthy**, Ph.D. 1997; Post-Doctoral Fellow 1997-present,  
Graduate Research Associate in Applied Mechanics, 1995-1997.
3. **Dr. Kyunghoon Lee**, Ph.D. 1998,  
Graduate Research Associate in Applied Mechanics, 1995-1997.
4. **Mingshan Li**, Ph.D. 1998,  
Graduate Research Associate in Applied Mechanics, 1995-1997.
5. **Madhusudhana Narasa**, M.S. 1997,  
Graduate Research Associate in Applied Mechanics, 1996-1997.